Large Eddy Simulation of Partially Premixed Flames using Doubly Conditional Source-term Estimation

by

Mohammad Mortada Ahmed

A thesis
presented to the University of Waterloo
in fulfillment of the
thesis requirement for the degree of
Doctor of Philosophy
in
Mechanical and Mechatronics Engineering

Waterloo, Ontario, Canada, 2019

Examining Committee Membership

The following served on the Examining Committee for this thesis. The decision of the Examining Committee is by majority vote.

External Examiner: Epaminondas Mastorakos
Professor, Department of Mechanical Engineering,
University of Cambridge

Supervisor(s): Cecile B. Devaud
Professor, Mechanical and Mechatronics Engineering,
University of Waterloo

Internal Member: Sean Peterson
Associate Professor, Mechanical and Mechatronics Engineering,
University of Waterloo

Internal Member: Jean-Pierre Hickey
Assistant Professor, Mechanical and Mechatronics Engineering,
University of Waterloo

Internal-External Member: Andrea Katherine Scott
Assistant Professor, Systems Design Engineering,
University of Waterloo

Author's Declaration

I hereby declare that I am the sole author of this thesis. This is a true copy of the thesis, including any required final revisions, as accepted by my examiners.

I understand that my thesis may be made electronically available to the public.

Abstract

Doubly Conditional Source-term Estimation (DCSE) is a partially premixed formulated closure to model turbulent combustion. The conditioning variables are selected to be mixture fraction and progress variable to represent the non-premixed and premixed flame characteristics, respectively. The statistical distribution of mixture fraction and progress variable is described by a β-Probability Density Function (PDF) and Modified Laminar Flame (MLF-PDF), respectively.

In the current study, DCSE is extended to the LES framework to provide further details about the mixing field. In LES, challenging transient phenomena that include lift-off, local extinction and reignition can be assessed. Filtered transport equations of mass, momentum, enthalpy and species mass fractions are solved. In addition, transport equations for the filtered mixture fraction and progress variable, and their Sub-grid Scale (SGS) variance are solved to provide the statistical description of both conditioning variables.

Detailed Chemistry is included in the investigation by using GRI-MECH 2.11 and 3.0. To reduce the computational cost, reaction rates are tabulated prior to the LES-DCSE calculations as a function of mixture fraction, CO_2 and H_2O mass fractions.

A least square numerical technique, LSQR, and a more detailed closure for the progress variable Scalar Dissipation Rate (SDR) are initially assessed using RANS-DCSE, which show better performance for LSQR as it reduces the matrix inversion time included in the DCSE implementation by 60%. The SDR model is shown to have an impact on the predictions. LES-DCSE is applied on a series of methane turbulent lifted flames. The predictions show very good agreement with the experimental data, and the qualitative analysis is consistent with triple flame characteristics.

A series of methane-piloted partially premixed flames is investigated in LES by using DCSE. LES-DCSE is able to capture the local extinction and reignition with which these flames are characterized. A very good agreement with experimental data is found in the predictions that include radial profiles of Favre-filtered velocity, temperature, mixture fraction and major and minor species mass fractions. These results demonstrate the capability of LES-DCSE of modelling partially premixed flames. Future work includes DCSE implementation in complex industrial burners, examining DCSE in spray combustion and improving the chemistry tabulation technique to be able to investigate complex fuels such as oxy-fuels and syngas.

Acknowledgements

First I would like to express my deep gratitude and sincere thanks to my supervisor Prof. Cécile Devaud for her expert guidance and wise counsel throughout my years of study and work in Waterloo. Her patience and support pushed me forward to continue and not to give up in the hardest times. Whatever I can say about her support will not be enough to thank her for.

I would like to thank my respectful committee members: Prof. Epaminondas Mastorakos, Prof. Sean Peterson, Prof. Jean-Pierre Hickey and Prof. Andrea Scott for granting me the honor of being in my present examination. The financial support of the Natural Science and Engineering Research Council of Canada (NSERC) is gratefully acknowledged. Also Compute Canada is acknowledged for providing the computational resources that are used in the present work. I would like to thank all my colleagues at the Energy Research Centre (ERC) for their valuable support, especially Daniele Dovizio, Jeff Labahn, Kevin Lee, Duy Lee, Daniel Wilson, Mehdi Ashrafizadeh, Ahmed Hussien, Samaneh Zareian and Alexandra McGowen. I also like to thank my friends from the University of Waterloo, especially Amer Keblawi and Ali Assem for their sincere friendship. I would like to thank Prof. Kendal Bushe and his team for their help and the fruitful sharing of experience, especially Graham Hendra, Hong Tsui and Stefanie De Graaf.

I finish with Egypt, where the most basic source of my identity resides. Truly I can say I would not have reached this point in my life without the support of my family. I would like to deeply thank my precious mother and my late father for building me up block by block and supporting me since my childhood till PhD degree. I gratefully acknowledge the positive role that my brothers, Bassem and Mostafa, played in the formation of my academic character and their continuous moral support. A special thanks are granted to my beloved wife for her love, affection and patience.

Dedication

This work is dedicated to ones I love: God, my family and my close friends.

Table of Contents

List of Figures

List of Tables

Nomenclature

Greek symbols

$\vec{\alpha}$	Conditional-averaged/filtered water mass fraction vector
$\vec{\alpha}_0$	*a priori* knowledge of the solution $\vec{\alpha}$
β	Temperature exponent
χ	Scalar Dissipation Rate (1/s)
Δ	Filter size (m)
δ	Delta function
$\Delta h^o{}_{f,k}$	Mass enthalpy of formation of species k (J)
δ_{ij}	Kronecker's delta
δ_L	Laminar thermal thickness (m)
ε	Dissipation rate of the turbulent kinetic energy ($\mathrm{m}^2/\mathrm{s}^3$)
ε_{sgs}	Dissipation rate of the sub-grid scale turbulent kinetic energy ($\mathrm{m}^2/\mathrm{s}^3$)
η	Mixture fraction sample space
λ	Regularization parameter/ Thermal conductivity (W/m.K)

μ	Absolute viscosity (Pa.s)
μ_t	Turbulent viscosity (Pa.s)
ν_t	Sub-grid scale kinematic viscosity (m^2/s)
ρ	Density (kg/m^3)
σ_k	Standard k-ε model constant
σ_ε	Standard k-ε model constant
τ	Heat release parameter
τ_{ij}	Viscous stress tensor (Pa)
$\widetilde{\phi}$	Favre-averaged/filtered ϕ
$\phi^{''}$	Fluctuation of the Favre-averaged/filtered ϕ
$\dot{\omega}_k$	Chemical source-term of species k (1/s)
$\dot{\omega}_F$	Fuel mass reaction rate (1/s)
$\overline{\dot{\omega}}_p$	The premixed mode contribution term in the progress variable source-term (1/s)
$\overline{\dot{\omega}}_{np}$	Non-premixed mode contribution term in the progress variable source-term (1/s)
$\overline{\dot{\omega}}_{cd}$	Cross-dissipation contribution term in the progress variable source-term (1/s)
$\overline{\dot{\omega}}_c$	Chemical contribution term in the progress variable source-term (1/s)

Roman symbols

A	Integrated joint Probability Density Function (PDF)/Filtered Density Function (FDF) matrix/ The pre-exponential constant
$\vec{b}$	Unconditional averaged/filtered water mass fraction.

C_B	Eddy Break-Up model constant
c	Reaction progress variable
c^*	Progress variable sample space
$\widetilde{C}_{CH_4}$	Time-averaged methane concentration
C_μ	Standard k-ε model constant
$C_{\varepsilon 1}$	Standard k-ε model constant
$C_{\varepsilon 2}$	Standard k-ε model constant
C_s	Smagorinsky coefficient
C_{p_k}	Specific heat capacity of species k at constant pressure (J/kg.K)
d	The main fuel jet inlet diameter
D_t	The turbulent diffusivity
Da_Δ	Sub-grid scale Damköhler
$f_{k,i}$	Body force along i acting on species k (N)
$f_{j/i}$	Mass fraction of element j in species i
F	LES filter
h_t	Total enthalpy (J)
h	Lift-off height (mm)
I	Identity matrix
Ka	Karlovitz number
k	Turbulent kinetic energy (m^2/s^2)
k_{sgs}	Sub-grid scale component of turbulent kinetic energy (m^2/s^2)
Le	Lewis number

M	Number of column in matrix A
N	Number of rows in matrix A/ number of species
N_A	Avogadro's number
P	Probability Density Function/ Filtered Density Function
p	Pressure (Pa)
P_k	Production term in turbulent kinetic energy transport equation
Pr_t	Turbulent Prandtl number
$\dot{Q}_r$	Heat source-term due to radiation (W)
q_i	Heat flux in i direction (W/m^2)
Re	Reynolds number
S	Oxidizer-fuel stoichiometric mass ratio
S_L	Unstrained laminar flame velocity (m/s)
Sc_t	Turbulent Schmidt number
$\widetilde{S_{ij}}$	Filtered strain rate tensor
t	Time (s)
Tr	Trace of a matrix
T_b	Adiabatic flame temperature (K)
T_u	Unburnt gas temperature (K)
T_A	Activation temperature (K)
u_i	Velocity component in i direction (m/s)
${u'}_\Delta$	Sub-grid scale velocity (m/s)
$\overline{U}$	Filtered velocity component (m/s)

$u^{'}$	Residual sub-grid scale velocity component (m/s)
$V_{k,i}$	Diffusion velocity of species k in i direction (m/s)
$\overline{W}$	Time-averaged reacting jet width (mm)
$\overline{W}_f$	Flammability region width (mm)
x_i	Spatial component in i direction (m)
Y_k	Mass fraction of species k
Y_F	Fuel mass fraction
Y_O	Oxidizer mass fraction
Y_i	Mass fraction of element i in the local mixture
$Y_{i,o}$	Mass fraction of element i in the oxidizer
$Y_{i,f}$	Mass fraction of element i in the fuel
$Y_e(j)$	Mass fraction of element j
Z	Mixture fraction

Chapter 1

Introduction

1.1 Combustion in the energy sector

The gradual increase in energy demand all over the world, due to the expansion of industry and the growth in the world population, is estimated to be 1.8% per year in 2005, and expected to rise further [1]. Due to the increase in energy demands, many sources of energy have become the focus of investigation and research, most of which are renewable sources of energy. Many countries have managed to increase their energy supply sourced by renewable energy; for example, Canada provided 17.3% of its energy supply from renewable sources in 2017 [2]. Despite the progress in using renewable sources of energy, 81% of global energy production relies on combustion of fossil fuels to unleash the stored chemical energy, usually within a combustion chamber [3]. The combustion-operated applications are various and include power generation, heating, transportation and several industrial processes. Most of these applications are operated using turbulent combustion, as it is characterized by high heat release and enhanced mixing. Further, some applications favour combustion over other energy sources (such as transportation and jet engines) due to the high energy density stored in the fossil fuels.

Consequently, the turbulent combustion of fossil fuels will remain a major player for the transportation and power generation in the short/mid-term future. However, it is also a major source of undesirable gaseous emissions. These gaseous emissions include greenhouse gases (GHG), nitrogen and sulphur oxides ($\mathrm{NO_x}, \mathrm{SO_x}$), and soot particles. The GHG emitted by the stationary combustion sources and transportation formed 74% of the total GHG emissions in Canada in 2017 [4]. Further, the average global level of carbon dioxide (CO_2) in the atmosphere increased by 1.7% from 2018 to 2019 [3]. This increase accelerates global warming, which is expected to cause environmental and natural catastrophes in the future. Other atmospheric pollutants, such as nitrogen oxides ($\mathrm{NO_x}$) and soot particles, may also be formed due to high temperature and incomplete burning of fuel, respectively. Transportation and mobile equipment are the largest contributors (52%) to the total $\mathrm{NO_x}$ emission release in Canada in 2017 [2].

These statistics have forced governments to impose strict emission regulations on overall combustion processes. The emission control requires increasing the efficiency of the combustion process, and thus design improved combustion devices that can produce less emissions and follow the regulations. Many experimental studies are devoted to improving the combustion process and reducing $\mathrm{NO_x}$ and unburnt hydrocarbons. In addition, Computational Fluid Dynamics (CFD) simulations based on rigorous modelling are also needed to optimize the combustion process and the combustion chamber design.

The numerical simulation of turbulent combustion can be implemented using three approaches: Direct Numerical Simulation (DNS), Large Eddy Simulation (LES), and Reynolds-Averaged Navier-Stokes (RANS) calculation. Although DNS is based on resolving all turbulence scales and provides the most accurate predictions among the three approaches, it is not computationally feasible due to the enormous required computational resources, especially for high Reynolds number flows, and the limitation to simple geometries. In contrast, RANS approaches model all the turbulence length/time scales which makes it the fastest computationally, but the least accurate; it also lacks detailed description of the mixing field. As a compromise between DNS and RANS, LES is considered the most promising tool among the three listed techniques to describe turbulence-chemistry interaction and model temporal phenomena. Only small turbulent scales (smaller than a specific filter width) are modelled, while all the larger scales are resolved. Moreover, LES can be used with more complicated geometries compared to DNS. With reasonable computational resources, it can provide more details about the flow/mixing fields compared to RANS calculations. These reasons have led to the selection of LES for the current research framework.

A combination of reliable turbulence model, detailed chemistry and a combustion model is expected to provide good numerical predictions of flames that will help in emission control and efficiency improvement. The newly-developed numerical tools should focus on the types of flames that are found in real-life combustion applications to provide accurate predictions for the flame parameters and characteristics. In the next section, the main flame categories are described.

1.2 Motivation

The combustion process may be broadly divided into two categories: i) premixed combustion, and ii) non-premixed combustion. In premixed combustion, the fuel and the oxidizer have a complete mixing before being released into the combustion space. In contrast, in non-premixed combustion, the mixing of fuel and oxidizer takes place inside the combustion chamber after separate injection. In many industrial applications, the combustion process can be described as partially premixed which is an intermediate stage between the premixed and non-premixed characteristics. These applications include gas turbines, domestic and industrial boilers, furnaces and some automotive engines [5].

The partially premixed combustion regime is expected to have a significant impact on the prediction of the flame characteristics including the heat release rate and the product levels [6], as compared to investigating the same flame using only premixed or non-premixed modelling formulation. Therefore, the accurate modelling of turbulent partially premixed flames is essential to achieve and design optimal combustion devices in many applications. Providing a rigorous numerical model is very important to capture the transient processes that are observed in real combustion devices. These processes include the lift-off of the turbulent lifted flames, as well as the local extinction and reignition in the flames that operate close to the stability operation range. Therefore, turbulent jet lifted flames and flames with high local extinction have become the target of modelling in the present work. Lifted jet flames have captured the interest of combustion research for the last fifty years. They have been investigated analytically, experimentally, and numerically [7]. This significant interest is due to their prevalence in many industrial combustion applications. These applications include burners in commercial boilers, jet engines, and gas flares. In addition, lifted flames are involved in combustion in turbines, diesel engines, and direct fuel injection gasoline engines which involve stratified mixtures. Such flames involve some physical phenomena which are complicated to investigate and model such as ignition, flame extinction, and stabilization [7]. Recently, a combustion model that is based on partially premixed flame formulation, known as Doubly Conditional Source-term Estimation (DCSE), has been developed and used in RANS [8, 9]. This model has shown a good performance in RANS, in addition to the fact that it has no restriction to combustion regimes and can be linked to detailed chemistry. Also, it has a reasonable computational cost in comparison with the other combustion models that use detailed chemistry, which makes it a promising selection to extend to LES and provide a detailed assessment for its performance with lifted flames and flames with significant levels of extinction.

1.3 Objectives

The current work aims to extend a partially premixed formulation (DCSE), that was first proposed for use with RANS [8], to be capable of simulating partially premixed flames in LES. In addition, the transient processes that are not able to be captured in RANS will be investigated and assessed in LES where more reactive flow details are provided. The objectives are summarized as

1. **Improved DCSE implementation for LES**: Initial assessment of a computational tool for solving least squares problems to be used in DCSE calculations, namely Least Squares QR-factorization (LSQR), in comparison with LU-decomposition initially implemented in RANS. The investigation is focused on CPU time and accuracy. In addition, a detailed closure for the scalar dissipation rate (SDR) term of the reaction progress variable [10, 9] is implemented and compared to the linear relaxation closure used in the previous RANS simulations [8]. Both assessments are carried out in RANS. The findings of these investigations were presented at the spring technical meeting of combustion institute/canadian section (CICS) 2016 [11].

2. **Investigation of LES-DCSE applied to turbulent lifted flames**: LES of a series of methane-air turbulent jet lifted flames using DCSE with detailed chemistry are implemented. The LES predictions are compared with experimental data [12, 13]. A qualitative analysis is provided in comparison to the experimental observations and the triple flame characteristics. In addition, the effect of some terms in the progress variable and its variance transport equations is investigated and discussed.

3. **Assessment of LES-DCSE for flames with increasing levels of extinction**: LES of a series of partially premixed methane-air piloted flames that exhibit increasing levels of local extinction using DCSE and detailed chemistry are carried out. The investigation includes comparing the predictions of velocity, mixture fraction, temperature and species mass fraction Favre-filtered radial profiles with experimental data at specific axial locations. Some conditional-filtered radial profiles are included in the quantitative analysis. A qualtitative analysis is provided to investigate local extinction in the three flames.

1.4 Overview of the study

In Chapter 2, background information is presented that includes a description of the governing equations that are involved in the current study. The different turbulence modelling approaches and the turbulent combustion modelling strategies are described. A review of the different theories used to explain the stabilization of the lifted flames, is provided. Previous investigations of the methane-piloted partially premixed flames of Sandia are summarized.

Chapter 3 provides a detailed description for the DCSE combustion model, that includes its basic concepts and assumptions, the mathematical formulation and the computational techniques used. In addition, the behaviour of the model is investigated at the DNS limit.

Chapter 4 outlines the RANS simulations carried out for a series of lifted flames to assess the effect of using LSQR and a more detailed SDR model on the computational time and accuracy prior to using them in LES which form the base of the current study.

In Chapter 5, DCSE is extended to LES to investigate a series of lifted flames with different Reynolds numbers. The study includes quantitative and qualitative analyses.

Chapter 6 describes LES investigation of a series of methane-air piloted flames that have different levels of extinction. A sensitivity analyses of different important parameters in the formulation of DCSE are carried out. Comparisons of the numerical predictions with experimental data, are included.

Finally, Chapter 7 summarizes the general conclusions of the present dissertation and the suggestions for future work.

1.5 Author's current contributions

It is acknowledged that parts of the content presented in chapter 3-5 are published in the following articles

- M. Mortada and C. Devaud. Large Eddy Simulation of lifted turbulent flame in cold air using Doubly Conditional Source-term Estimation. Combustion and Flame, 208:420 - 435, 2019.
- M. Mortada and C. B. Devaud. Large Eddy Simulations of Sandia flames D, E and F using Doubly Conditional Source-term Estimation. Proceedings of Combustion Institute/Canadian Section Spring Technical Meeting, University of British Columbia, May 13 - 16, 2019.
- M. Mortada and C. B. Devaud. Large Eddy Simulation of lifted turbulent flame in cold air using Doubly Conditional Source-term Estimation. Proceedings of Combustion Institute/Canadian Section Spring Technical Meeting, University of Ryerson, May 15, 2018.

- M. Mortada and C. B. Devaud. Large Eddy Simulation of turbulent lifted flame. Proceedings of Combustion Institute/Canadian Section Spring Technical Meeting, University of McGill, May 15 - 18, 2017.

- M. Yao, M. Mortada, C. Devaud and J. Hickey. Locally-Adaptive tabulation of Low-dimensional manifolds using Bezier patch reconstruction. Proceedings of Combustion Institute/Canadian Section Spring Technical Meeting, University of McGill, May 15 - 18, 2017.

- M. Mortada and C. B. Devaud. Numerical investigation of Doubly Conditional Source-term Estimation applied to turbulent partially premixed combustion. Proceedings of Combustion Institute/Canadian Section Spring Technical Meeting, University of Waterloo, May 10 - 12, 2016.

- M. Mortada and C. B. Devaud. Assessment of LES-DCSE to capture local extinction in the Sandia piloted turbuelnt jet flames D-F. Proceedings of the Combustion Institute, under review, 2020.

Chapter 2

Literature Review

This chapter provides background information including the governing equations, a description for the turbulence approaches used in the current work, and the different strategies used to model turbulent combustion. This is followed by a review on turbulent lifted flames and their stabilization theories, as well as a review of previous investigations used to model Sandia flames (D-F).

2.1 Instantaneous governing equations

Transport equations of mass, momentum, enthalpy (energy) and species mass fractions must be considered for the simulation of a turbulent reacting flow. The transport equation of mass is expressed as

$$\frac{\partial \rho}{\partial t} + \frac{\partial}{\partial x_i}(\rho u_i) = 0, \tag{2.1}$$

where ρ is the density, t time, x_i spatial components and u_i the velocity components for $i = 1$ to 3. Navier-Stokes equation (momentum balance) is considered in the form

$$\frac{\partial(\rho u_j)}{\partial t} + \frac{\partial(\rho u_i u_j)}{\partial x_i} = -\frac{\partial p}{\partial x_j} + \frac{\partial \tau_{ij}}{\partial x_i} + \rho \sum_{k=1}^{N} Y_k f_{k,j}, \tag{2.2}$$

where p is the pressure, τ_{ij} the viscous stress tensor, Y_k the mass fraction of species k and $f_{k,j}$ the body force along j acting on species k. For newtonian fluids, the viscous stress tensor is expressed as

$$\tau_{ij} = -\frac{2}{3}\mu \frac{\partial u_k}{\partial x_k}\delta_{ij} + \mu\left(\frac{\partial u_i}{\partial x_j} + \frac{\partial u_j}{\partial x_i}\right), \tag{2.3}$$

where μ is the absolute viscosity and δ_{ij} the kronecker's delta.
The energy equation, presented as total enthalpy (h_t) balance, can be written as

$$\frac{\partial}{\partial t}(\rho h_t) + \frac{\partial}{\partial x_i}(\rho u_i h_t) = \frac{Dp}{Dt} + \tau_{ij}\frac{\partial u_i}{\partial x_j} - \frac{\partial q_i}{\partial x_i} + \dot{Q}_r + \rho \sum_{k=1}^{N} Y_k f_{k,i} V_{k,i}, \tag{2.4}$$

where $\tau_{ij}\frac{\partial u_i}{\partial x_i}$ is the heating source term due to friction, q_i the energy flux, the term $\rho\sum_{k=1}^{N} Y_k f_{k,i} V_{k,i}$ the power produced by volume forces f_k on species k, and $\dot{Q}_r$ the heat source term due to radiation [14].
The total enthalpy is defined for a mixture of N species as

$$h_t = \sum_{k=1}^{N} h_{tk} Y_k = \sum_{k=1}^{N} (\int_{T_o}^{T} C_{p_k} dT) + \sum_{k=1}^{N} \Delta h^o{}_{f,k} Y_k, \tag{2.5}$$

where $C_{p_k}$is the specific heat capacity of species k at constant pressure and $\Delta h^o{}_{f,k}$ the mass enthalpy of formation of species k at the reference temperature T_o.
The conservation of species k follows

$$\frac{\partial}{\partial t}(\rho Y_k) + \frac{\partial}{\partial x_i}(\rho u_i Y_k) = -\frac{\partial}{\partial x_i}(\rho V_{k,i} Y_k) + \dot{\omega}_k \qquad k = 1, N, \tag{2.6}$$

where $V_{k,i}$ is the i-component of the diffusion velocity V_k of species k, and $\dot{\omega}_k$ the reaction rate of species k [14].
In principle, Eqs (2.1 - 2.6) are discretized in space and time for numerical investigation.

2.2 Favre-averaged transport equations in RANS

In RANS, the transport equations are averaged to obtain the mean values of the prognostic variables (e.g. velocity, temperature). Reynolds-averaging produces unclosed terms that need closure. In reactive flows, density-weighted or Favre-averaged quantities are used to account for the large changes in density and avoids additional unclosed terms generated by Reynolds averaging.
For any quantity ϕ of interest, the Favre-averaging is calculated as

$$\widetilde{\phi} = \frac{\overline{\rho\phi}}{\overline{\rho}}, \tag{2.7}$$

and the fluctuations of this Favre-averaged quantity are defined as

$$\phi'' = \phi - \widetilde{\phi}. \tag{2.8}$$

The Reynolds-averaged transport equations include the conservation of mass

$$\frac{\partial\overline{\rho}}{\partial t} + \frac{\partial}{\partial x_i}(\overline{\rho}\widetilde{u}_i) = 0, \tag{2.9}$$

conservation of momentum (neglecting body forces)

$$\frac{\partial(\overline{\rho}\widetilde{u}_j)}{\partial t} + \frac{\partial(\overline{\rho}\widetilde{u}_i\widetilde{u}_j)}{\partial x_i} = -\frac{\partial\overline{p}}{\partial x_j} + \frac{\partial}{\partial x_i}(\overline{\tau_{ij}} - \overline{\rho}\widetilde{u_i''u_j''}), \tag{2.10}$$

Conservation of species mass fraction

$$\frac{\partial}{\partial t}(\overline{\rho}\widetilde{Y}_k) + \frac{\partial}{\partial x_i}(\overline{\rho}\widetilde{u}_i\widetilde{Y}_k) = -\frac{\partial}{\partial x_i}(\overline{V_{i,k}Y_k} + \overline{\rho}\widetilde{u_i''Y_k''}) + \overline{\dot{\omega}}_k \qquad k = 1, N, \tag{2.11}$$

and Conservation of energy

$$\frac{\partial}{\partial t}(\overline{\rho}\widetilde{h}) + \frac{\partial}{\partial x_i}(\overline{\rho}\widetilde{u}_i\widetilde{h}) = \frac{D\overline{p}}{Dt} + \frac{\partial}{\partial x_i}(\overline{\lambda\frac{\partial T}{\partial x_i}} - \overline{\rho}\widetilde{u_i''h''}) + \overline{\tau_{ij}\frac{\partial u_i}{\partial x_j}} + \overline{\dot{Q}}_r, \tag{2.12}$$

where

$$\frac{D\overline{p}}{Dt} = \frac{\partial\overline{p}}{\partial t} + \widetilde{u}_i\frac{\partial\overline{p}}{\partial x_i} + \overline{u_i''\frac{\partial p}{\partial x_i}}. \tag{2.13}$$

Some assumptions are used to model unclosed terms in the governing transport equations. The production terms in Eqs. (2.11) and (2.12) are modelled using the gradient assumption as

$$\overline{\rho}\widetilde{u_i''Y_k''} = -\frac{\mu_t}{Sc_{tk}}\frac{\partial\widetilde{Y}_k}{\partial x_i} \quad and \quad \overline{\rho}\widetilde{u_i''h''} = -\frac{\mu_t}{Pr_{tk}}\frac{\partial\widetilde{h}}{\partial x_i} \tag{2.14}$$

where μ_t is the turbulent viscosity that is calculated by turbulence model, Sc_t the turbulent Schmidt number, and Pr_t the turbulent Prandtl number for any species k.

In case of high Reynolds numbers, which is the common case for turbulent flows, the laminar diffusive fluxes $(\overline{V_{i,k}Y_k})$ for any species k (Eq. 2.11) or enthalpy $(\overline{\lambda\frac{\partial T}{\partial x_i}})$ (Eq. 2.12) are neglected compared to turbulent transport. The source term $\overline{\dot{\omega}}_k$ is closed by the combustion model which is covered in detail in Chapter 3. Reynolds stresses $(\widetilde{u_i''u_j''})$ are closed by a turbulence model.

There are several direct RANS turbulence models that involve one or two transport equations, in addition to solving balance equations for Reynolds stresses. In the current section, only the model that is used in Chapter 4 simulations is covered, for brevity.

2.2.1 Standard k-ε two equation model

This model is considered the most popular and time efficient in RANS models. It calculates the turbulent viscosity as

$$\mu_t = \overline{\rho} C_\mu \frac{k^2}{\varepsilon}, \tag{2.15}$$

where k and ε are described by the two transport equations

$$\frac{\partial}{\partial t}(\overline{\rho} k) + \frac{\partial}{\partial x_i}(\overline{\rho}\widetilde{u}_i k) = \frac{\partial}{\partial x_i}\left[(\mu + \frac{\mu_t}{\sigma_\epsilon})\frac{\partial k}{\partial x_i}\right] + P_k - \overline{\rho}\varepsilon, \tag{2.16}$$

$$\frac{\partial}{\partial t}(\overline{\rho} \varepsilon) + \frac{\partial}{\partial x_i}(\overline{\rho}\widetilde{u}_i \varepsilon) = \frac{\partial}{\partial x_i}\left[(\mu + \frac{\mu_t}{\sigma_\varepsilon})\frac{\partial \varepsilon}{\partial x_i}\right] + C_{\varepsilon 1}\frac{\varepsilon}{k}P_k - C_{\varepsilon 2}\overline{\rho}\frac{\varepsilon^2}{k}, \tag{2.17}$$

The model constants C_μ, σ_k, σ_ε, $C_{\varepsilon 1}$ and $C_{\varepsilon 2}$ are usually 0.09, 1.0, 1.3, 1.44 and 1.92, respectively. The source term P_k is calculated as

$$P_k = -\overline{\rho}\widetilde{u_i'' u_j''}\frac{\partial \widetilde{u}_i}{\partial x_j}, \tag{2.18}$$

where Reynolds stress term is obtained by Boussinesq approximation as

$$\overline{\rho}\widetilde{u_i'' u_j''} = -\mu_t \left(\frac{\partial \widetilde{u}_i}{\partial x_j} + \frac{\partial \widetilde{u}_j}{\partial x_i} - \frac{2}{3}\delta_{ij}\frac{\partial \widetilde{u}_k}{\partial x_k}\right) + \frac{2}{3}\overline{\rho}k, \tag{2.19}$$

where the TKE is obtained by

$$k = \frac{1}{2}\sum_{k=1}^{3}\widetilde{u_k'' u_k''}. \tag{2.20}$$

2.3 Filtered transport equations in LES

The dissipation scales are modelled in LES, which are described as Sub-Grid Scales (SGS), while all the other scales are resolved. Therefore, LES provides better and more elaborate description of mixing field compared to RANS simulations. The LES computational cost is much lower compared to DNS simulations [15], but larger than the computational cost in RANS. In LES, the large and dissipation scales are separated using a spatial filtering process. The limit above which scales are resolved is called a cut-off scale. The filtering function decomposes the velocity as follows

$$U(x,t) = \overline{U}(x,t) + u^{'}(x,t), \tag{2.21}$$

where $\overline{U}$ is the filtered velocity component and $u^{'}$ the residual (SGS) velocity component. The governing equations of LES are determined by applying a filter on the flow variables in the spectral or physical space. The filtered quantity $\overline{f}$ is obtained by

$$\overline{f}(\vec{x},t) = \int f(\vec{x'},t)F(\vec{x}-\vec{x'})d\vec{x'} \tag{2.22}$$

where F represents the LES filter. Several types of filters can be used, including a cut-off filter in spectral space, a box filter (top-hat filter) in physical space, and a Gaussian filter in physical space.
The top hat filter is defined as

$$F(\vec{x}-\vec{x'}) = \begin{cases} \frac{1}{\Delta^3} & |\vec{x}-\vec{x'}| \leq \frac{\Delta}{2} \\ 0 & otherwise \end{cases}, \tag{2.23}$$

where Δ is the filter size. This filter performs an averaging over a cubic box of size Δ. For variable density, a Favre-filtering can be obtained as

$$\tilde{f}(\vec{x},t) = \frac{1}{\bar{\rho}}\int \rho f(\vec{x'},t)F(\vec{x}-\vec{x'})d\vec{x'} \tag{2.24}$$

LES (filtered) balance equations are obtained by filtering the instantaneous balance equations, which look very similar to RANS equations. They include (with the gradient assumption used in Eqs. (2.27) and (2.28))

- Conservation of mass

$$\frac{\partial\overline{\rho}}{\partial t} + \frac{\partial}{\partial x_i}(\overline{\rho}\widetilde{u_i}) = 0, \tag{2.25}$$

- Conservation of momentum

$$\frac{\partial\overline{\rho}\widetilde{u_i}}{\partial t} + \frac{\partial}{\partial x_i}(\overline{\rho}\widetilde{u_i}\widetilde{u_j}) + \frac{\partial\overline{p}}{\partial x_j} = \frac{\partial}{\partial x_i}\Big(\overline{\tau}_{ij} - \overline{\rho}(\widetilde{u_iu_j} - \tilde{u}_i\tilde{u}_j)\Big), \tag{2.26}$$

- Conservation of energy

$$\frac{\partial\overline{\rho}\widetilde{h_t}}{\partial t} + \frac{\partial}{\partial x_i}(\overline{\rho}\widetilde{u_i}\widetilde{h_t}) = \frac{\partial}{\partial x_i}\Big(\bar{\rho}(\alpha+\alpha_t)\frac{\partial\widetilde{h}}{\partial x_i}\Big) + \frac{D\overline{p}}{Dt}, \tag{2.27}$$

- Conservation of species mass fraction

$$\frac{\partial\overline{\rho}\widetilde{Y_k}}{\partial t} + \frac{\partial}{\partial x_i}(\overline{\rho}\widetilde{u_i}\widetilde{Y_k}) = \frac{\partial}{\partial x_i}\Big((D+D_t)\frac{\partial\widetilde{Y_k}}{\partial x_i}\Big) + \overline{\dot{\omega}_k}, \tag{2.28}$$

where α and α_t are the molecular and turbulent thermal diffusivities, $\frac{D\overline{p}}{Dt}$ the total derivative of the filtered pressure, D and D_t the molecular and turbulent diffusivities, and $\overline{\tau}_{ij}$ is the viscous stress tensor which is obtained by

$$\overline{\tau}_{ij} \equiv -\overline{\rho}\mu\widetilde{u''_i u''_j} \equiv -\mu_t\left(\frac{\partial \tilde{u}_i}{\partial x_j} + \frac{\partial \tilde{u}_j}{\partial x_i} - \frac{2}{3}\delta_{ij}\frac{\partial \tilde{u}_k}{\partial x_k}\right). \tag{2.29}$$

The unclosed quantities in the resulting filtered Eqs. ((2.25) - (2.28)) include the unresolved Reynolds stresses $(\widetilde{u_i u_j} - \tilde{u}_i\tilde{u}_j)$ and the filtered chemical reaction rate $\overline{\dot{\omega}_k}$, while the filtered energy source term is not included as radiation is neglected in the present investigations. Finding models for the unknown terms in the LES governing equations may follow concepts developed in RANS, for example by using global quantities such as the SGS-TKE, k_{sgs}, and its dissipation rate, ε_{sgs}.

Smagorinsky SGS model is popular due to its simple formulation [16]. It is also based on the eddy-viscosity hypothesis. The unclosed residual stress tensor σ, which is defined as $\sigma_{ij} = \overline{\rho}(\widetilde{u_i u_j} - \tilde{u}_i\tilde{u}_j)$, is closed using the following expression

$$\sigma_{ij} - \frac{\delta_{ij}}{3}\sigma_{kk} = -\nu_t\left(\frac{\partial \overline{u}_j}{\partial x_i} + \frac{\partial \overline{u}_i}{\partial x_j}\right) = -2\nu_t\overline{S_{ij}}, \tag{2.30}$$

where $\overline{S_{ij}}$ is the filtered strain rate tensor, ν_t the SGS viscosity, which is modelled using the following simplified argument, assuming that the integral scale is of the same order of the grid size

$$\nu_t = (C_s\Delta)^2|\overline{S}| = (C_s\Delta)^2\left(2\overline{S_{ij}S_{ij}}\right)^{0.5}, \tag{2.31}$$

where C_s is Smagorinsky coefficient. This constant can be set to a fixed value or determined dynamically [17]. Applications of the Smagorinsky model to various problems have revealed that the constant is not universal and varies depending on resolution and flow characteristics. In the case of homogeneous isotropic turbulence, the model constant is estimated as $C_s \approx 0.2$.

For laminar shear flows in which the residual shear stresses are zero, the appropriate value of the Smagorinsky coefficient is zero. Therefore, a non-zero value of C_s would lead, incorrectly, to residual shear stresses on the order of Δ. This problem is not found in RANS, where the RANS equation reverts to the Navier-Stokes equation with zero Reynolds stresses in case of laminar flow conditions.

Moreover, the Smagorinsky model is known as being too dissipative, especially near solid no-slip boundaries.

Some modifications are suggested to obtain better performance from this model, including

- Dynamically calculating the model coefficient [17].
- Introducing transport equations for relevant quantities. In particular, solving an equation for the SGS-TKE allows a much better estimation of the velocity scale for the SGS fluctuations [18].

2.4 Turbulent combustion models

The wide range of reaction time scales, with order of magnitude from 10^{-10} to 1 second [19, 14], represents a challenge for chemistry inclusion in reactive flows. In addition, the averaging or filtering process creates a challenging unclosed term in the Favre-averaged/filtered species transport equation(s) which is the chemical source-term [19]. According to Arrhenius law [14], the fuel mass reaction rate $\dot{\omega}_F$ can be obtained by

$$\dot{\omega}_F = -A\rho^2 T^\beta Y_F Y_O e^{\frac{-T_A}{T}}, \tag{2.32}$$

where A is the pre-exponential constant, β the temperature exponent, Y_F fuel mass fraction, Y_O oxidizer mass fraction and T_A the activation temperature. Due to the non-linearity of Eq.2.32, the averaged/filtered reaction rates cannot by calculated from the averaged/filtered scalars as

$$\overline{\dot{\omega}(\rho, T, Y_k)} \neq \dot{\omega}(\overline{\rho}, \overline{T}, \overline{Y_k}). \tag{2.33}$$

Detailed chemical schemes will increase the complexity of the estimation of the averaged/filtered reaction rates. However, the use of simple chemistry with simple estimation of the source-term, such as using Taylor series of the temperature fluctuation, will lead to new terms to be modelled. Moreover, a truncation error will be encountered as there is no way of providing infinite closures for infinite unclosed terms.

A better alternative, which is reliable compared to the simple Taylor series, is to derive a numerical strategy based on physical assumptions to estimate the averaged/filtered chemical source-term. Some strategies will be described in Section (2.4.1-2.4.6). A categorization that is performed by Bilger et al. [20] divides the combustion modelling strategies into a number of approaches that includes the mixing controlled approach, that assumes that chemistry is faster than any other physical processes in the flow with examples of

Eddy-Dissipation Concept (EDC) and Eddy-Break Up (EBU) model. Other approaches include the laminar flamelet approach which assumes that the chemical reaction can be described in terms of small narrow flamelets that are assumed to be smaller that the microscales of the flow. On the other side, the transported Probability/Filtered Density Function (PDF/FDF), Conditional Moment Closure (CMC), Multiple Mapping Conditioning (MMC) and CSE/DCSE are not dependent on such physical assumptions.

2.4.1 Infinitely fast chemistry assumption

The chemistry time scale is assumed to be very fast compared to the mixing time scale, which is a reasonable assumption in non-premixed flames where chemical time scale is found to be much smaller than the time scale of the other physical processes, such as convection and diffusion [14]. Two common models based on infintely fast chemistry are EDC and EBU models, where the first is developed for non-premixed combustion by Magnussen [21] and the second is for premixed by Spadling [22]. In EBU-type models, the mean reaction rate is a function of the rate of mixing between the reactants and hot products which is carried out by turbulence effect. The mean reaction rate of any product species k is expressed as

$$\overline{\dot{\omega}_k} = C_B \rho \frac{\varepsilon}{k} \widetilde{Y_k''^2}^{\frac{1}{2}}, \tag{2.34}$$

where C_B is a model constant that needs to be estimated for each case under investigation as it can be different from case to another, and $\widetilde{Y_k''^2}$ the variance of the product species k mass fraction. Although the EBU model is considered the fastest approach to combustion modelling due to its high simplicity, it usually produces over-prediction on the reactive scalars, in addition to the fact that detailed chemistry cannot be included in the model. The EDC model provides a closure for the averaged/filtered source term as

$$\overline{\dot{\omega}}_{fu} = C_D \overline{\rho} \frac{\varepsilon}{k} min\left(\widetilde{Y}_{fu}, \frac{\widetilde{Y}_{ox}}{S}, \beta \frac{\widetilde{Y}_{fu}}{1+S}\right), \tag{2.35}$$

where C_D and β are model parameters that need adjustment from case to another, S the oxidizer-fuel stoichiometric mass ratio, $\widetilde{Y}_{fu}$ and $\widetilde{Y}_{ox}$ the Favre-averaged/filtered mass fraction of fuel and oxidizer, respectively. This model is considered as simple as EBU model, however it can handle finite rate kinetics by modifying the mixing time scales with chemical time scale information. This modification allows for coupling EDC with detailed chemistry [23]. However, the fact that the model constants need investigation for each individual case, does not make it a robust combustion modelling strategy for industrial applications.

2.4.2 Laminar flamelet model

This approach has been proposed by Peters [24] and Kuznetsov [25], independently. This model is based on assuming that the turbulent diffusion flame consists of an ensemble of stretched laminar flamelets (extremely small, thin flame elements) [26].

Due to the fact that diffusion flames are controlled by the degree of mixing of the fuel and the oxidizer, a conserved scalar Z is introduced to track the mixedness of the reactants, which is called mixture fraction. This scalar takes ranges between the two extreme cases (0 at pure oxidizer and 1 at pure fuel). The mixture fraction can be described by Bilger's definition

$$Z = \frac{Y_i - Y_{i,O}}{Y_{i,F} - Y_{i,O}}, \tag{2.36}$$

where Y_i the mass fraction of element i in the local mixture, and $Y_{i,O}$ and $Y_{i,F}$ are the mass fraction of the element i in the oxidizer and the fuel streams, respectively. The mixture fraction can be obtained by solving a transport equation for its mean/filtered value, which is capable of describing the variation of other scalars involved in the reactive flow in case of assuming fast chemistry, no heat loss and equal diffusivity. The Favre-averaged/filtered transport equation of mixture fraction can be expressed as

$$\frac{\partial(\overline{\rho}\widetilde{Z})}{\partial t} + \frac{\partial}{\partial x_i}(\overline{\rho}\widetilde{u}_i\widetilde{Z}) = \frac{\partial}{\partial x_i}\left(\overline{\rho D\frac{\partial Z}{\partial x_i}} - \overline{\rho}\widetilde{u_i''Z''}\right), \tag{2.37}$$

where turbulent flux is closed using the gradient assumption as

$$\widetilde{u_i''Z''} = -D_t\frac{\partial \widetilde{Z}}{\partial x_i}, \tag{2.38}$$

where D_t is the turbulent diffusivity. The first order moment of the mixture fraction is not sufficient to describe/estimate the reactive scalars' averaged/filtered values. Therefore, its variance $\widetilde{Z''^2}$ is transported by

$$\begin{aligned}\frac{\partial(\overline{\rho}\widetilde{Z''^2})}{\partial t} + \frac{\partial}{\partial x_i}(\overline{\rho}\widetilde{u}_i\widetilde{Z''^2}) = \frac{\partial}{\partial x_i}\left(\overline{\rho D\frac{\partial Z''^2}{\partial x_i}} - \overline{\rho u_i''Z''^2}\right) - \overline{2Z''\frac{\partial}{\partial x_i}\left(\rho D\frac{\partial Z}{\partial x_i}\right)}\\ -2\overline{\rho u_i''Z''}\frac{\partial \widetilde{Z}}{\partial x_i} - \overline{2\rho D\frac{\partial Z''}{\partial x_i}\frac{\partial Z''}{\partial x_i}}.\end{aligned} \tag{2.39}$$

The turbulent transport $(-\frac{\partial}{\partial x_i}\overline{\rho u_i{}'' Z''^2})$ and the production term $(-2\overline{\rho u_i{}'' Z''}\frac{\partial \widetilde{Z}}{\partial x_i})$ are modelled using the gradient assumption similar to Eq. 2.38. The molecular diffusion $\left(\frac{\partial}{\partial x_i}\left(\overline{\rho D \frac{\partial Z''^2}{\partial x_i}}\right) - \overline{2Z''\frac{\partial}{\partial x_i}\left(\rho D \frac{\partial Z}{\partial x_i}\right)}\right)$ is negligible compared to the turbulent transport at high Reynolds flows.

The mean/SGS-SDR of the mixture fraction $(2\overline{\rho D \frac{\partial Z''}{\partial x_i}\frac{\partial Z''}{\partial x_i}})$ dissipates the fluctuations of the mixture fraction analogous to the TKE dissipation rate and the fluctuations in velocity. This analogy led to the linear relaxation model of the mixture fraction SDR, $\widetilde{\chi}_Z$, which is expressed as

$$\widetilde{\chi}_Z = C_{\chi Z}\frac{\widetilde{\varepsilon}}{\widetilde{k}}\widetilde{Z''^2}, \tag{2.40}$$

where C_{χ_Z} is a constant that is usually taken to be 2 [6]. As the ensembles of laminar flamelets are pre-tabulated as a function of the mixture fraction prior to the CFD calculations and the first and second moments of the mixture fractions are used to calculate the PDF/FDF, the Favre-averaged mass fraction of species k is evaluated by integrating the presumed PDF/FDF multiplied by the ensemble of laminar flamelets at different strain rates, which represents the flame structure, over the mixture fraction sample space, following the expression

$$\widetilde{Y}_k = \int_0^1 Y_k(Z)\widetilde{P}(Z;\vec{x},t)dZ, \tag{2.41}$$

where $Y_k(Z)$ is the tabulated mass fraction of species k as a function of Z.

The assumption of fast chemistry is avoided in case of finite-rate chemistry and an additional tabulation variable is required to address the flame away from the equilibrium conditions. The SDR of the mixture fraction is usually used for this purpose due to its influence in flame structure.

In non-premixed flames, different combustion regimes can be identified based on influential quantities as shown in Fig. 2.1 where the ratio between the SDR for which quenching takes place and the SDR conditioned at stoichiometric conditions $(\frac{\chi_q}{\widetilde{\chi}_{st}})$, and the ratio between stoichiometric mixture fraction root mean square (RMS) and flame thickness $(\frac{(\widetilde{Z''^2})^{\frac{1}{2}}}{(\Delta Z)_F})$ represent key quantities to define the non-premixed combustion regime. Further, Fig. 2.1 also illustrates the dependence of the flame structure on spatial location in real flames using a turbulent lifted flame sketch, which shows that some practical flames can encounter more than one combustion regime in its structure. It is worth noting that the non-premixed

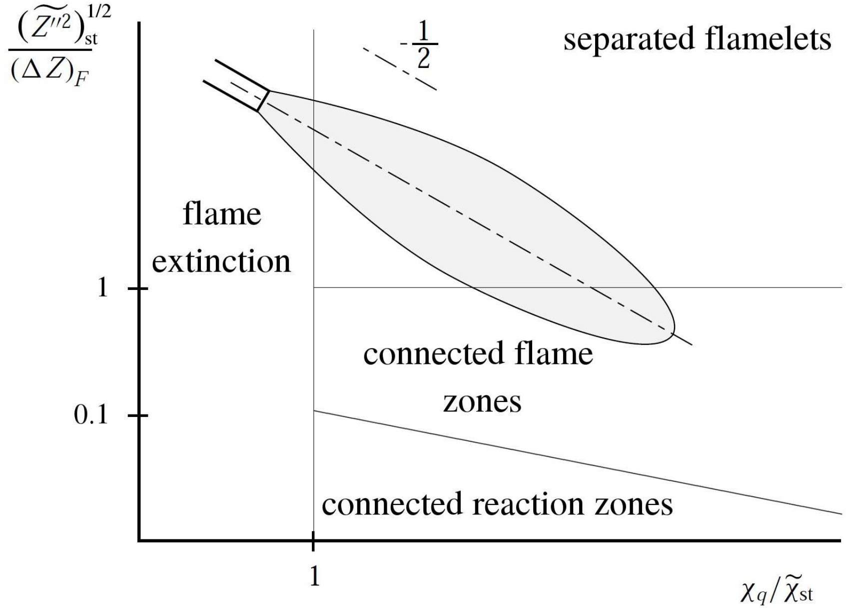

Figure 2.1: Non-premixed turbulent combustion regimes [6]

flamelet model works the best in the flamelets regime where the flamelet assumption (the flamelets are assumed to be smaller than the Kolmogorov scales) is satisfied.

The flamelet model can be used to investigate premixed flames but with a different key scalar than the mixture fraction. Instead, a progress variable is selected or G-equation approach is used to describe the degree of combustion completion [14]. A normalized reaction progress variable c is usually selected so that its value can vary from 0 at no combustion to 1 at complete combustion. Similar to the mixture fraction, the progress variable is transported in the form

$$\frac{\partial(\overline{\rho}\widetilde{c})}{\partial t} + \frac{\partial}{\partial x_i}(\overline{\rho}\widetilde{u}_i\widetilde{c}) = \frac{\partial}{\partial x_i}\left(\overline{\rho D \frac{\partial c}{\partial x_i}} - \rho\widetilde{u_i''c''}\right) + \overline{\dot{\omega}}_c. \tag{2.42}$$

Unlike the mixture fraction, the progress variable is not a conserved scalar as it has a source-term that needs to be closed. It can be closed with different closures that include Bray-Moss-Libby (BML) model[27] and the flame surface density (FSD) model [14]. Overall, the flamelet model involves better chemistry description than EDC or EBU models with reasonable computational expense. However, the drawback of this model is that it is limited to the flamelet regime where turbulent eddies are not expected to affect the flame structure. In other words, the assumption of laminar flamelets is valid if Kolmogorov eddies are larger than the thin reaction zones.

2.4.3 Conditional Moment Closure (CMC)

The idea that the fluctuations about mean/filtered quantities are significantly reduced once they are conditioned on a specific selected scalar, forms the basis of CMC model that is first proposed by Bilger [28] and Klimenko [29], independently. CMC model has the advantage that it is not restricted to specific turbulent combustion regime and can be coupled with finite-rate kinetics. In non-premixed combustion, the reactive scalars are often conditioned on mixture fraction, while a progress variable is selected as a conditioning variable in premixed combustion. The mean/filtered value of any scalar f is obtained by the following integral

$$\widetilde{f} = \int_0^1 \overline{f|\eta}\widetilde{P}(\eta)d\eta, \tag{2.43}$$

where $\overline{f|\eta}$ is the conditional averaged/filtered f that is conditioned on a given value of mixture fraction, η. The conditional scalars, required to obtain the unconditional quantities, are obtained by solving their transport equations over a CMC grid corresponding to the CFD grid, but often much coarser. Also, the mixture fraction is discretized in a sample space to define a number of bins corresponding to the values on which the reactive scalars will be conditioned. The conditional scalar transport equation will result in some terms that require closure such as the conditional velocity, conditional turbulent flux and conditional chemical reaction rate. It is common in CMC that the fluctuations about the conditional averages are neglected, which led to the following estimation of the chemical source term

$$\overline{\dot{\omega}_k|\eta} \approx \dot{\omega}(\overline{T|\eta}, \overline{\rho|\eta}, \overline{Y_k|\eta}). \tag{2.44}$$

This hypothesis is called first order closure in CMC. The second order closure, which means providing fluctuations with closures, is used when the fluctuations cannot be neglected such as in autoignition or extinction cases [30]. Using two conditioning variables can be suitable alternative [31], but it will result in higher complexity of the model. Many investigations of non-premixed flames that are performed by CMC obtained very good predictions at different combustion regimes and transient phenomena [32, 19, 33]. However, the method encounters issues in the modelling of premixed flames mostly due to the added complexity of the conditional SDR closure and additional complexity of having a non-conserved conditioning variable [34]. Recently, numerical simulations of a premixed pilot stabilized flames have shown promising results for CMC [35]. Good predictions have been obtained for LES-CMC modelling of turbulent premixed bluff body flames close to blow-off [36].

2.4.4 PDF transport equation model

The PDF transport equation model is considered a general method that is not restricted to a specific combustion regime. It is also based on obtaining the averaged/filtered quantities by integration over the PDF distribution. In contrast to the flamelet or CMC models, the form of PDF or joint PDF is not presumed; a transport equation is solved for the joint PDF of velocity, viscous dissipation and reactive scalars [37].

PDF methods are applied to premixed and non-premixed flames. However, a closure issue is encountered in the PDF transport equation with the resultant mixing term, as the PDF equation does not have any information about mixing time. This mixing term can be modelled by including scalar gradients which increases the dimensionality of the model. Consequently, the high dimensionality of the PDF transport method made the regular finite difference or finite volume methods not feasible to be used in the solution [38]. To overcome this obstacle, Monte-Carlo Lagrangian method is developed by Pope [39] in order to reduce the computational expenses. In this method, a large number of stochastic particles are seeded to represent the flow, and their evolution in the flow field is used to determine the evolution of the joint PDF/FDF. Another approach is developed, independently, by Valiño [40] and Sabel'nikov and Soulard [41]. This alternative model uses stochastic fields instead of particles, and has no spatial sampling errors.

Generally, the PDF methods provide the best description of turbulent reacting flows [23] as they do not assume fast chemistry and they provide a closed form for the chemical source term. The generality of the model makes it preferable for partially premixed combustion. However, it is considered the most computationally expensive compared to the other models. In addition, the modelling of the mixing term forms an issue as the closure is usually complex and the accuracy of the predictions is affected by the quality of the closure.

2.4.5 Multiple Mapping Conditioning (MMC)

This technique is proposed by Klimenko and Pope [42] which is derived as a blend of the PDF transport equation and the CMC combustion models. The idea of this combination is that the joint PDF/FDF of the conditioning scalars is obtained implicitly which has to be consistent with the conditional dissipation rates of the species. Then, the statistics of the species and the dissipation rate fields are obtained from the joint PDF/FDF and the mapping. Blending two reliable models made MMC model one of the most promising methods, although the computational cost still needs reduction. It has been used successfully to simulate non-premixed [43, 44], premixed [45] and partially premixed flames [46]. However, it still not practical for simulating reactive flows in complex geometries because of the high computational cost [19].

2.4.6 Conditional Source-term Estimation (CSE)

This approach is first proposed by Steiner and Bushe [47]. It is based on the main concepts used to derive CMC, except that the conditional averages/filtered quantities, that are presented in Eq. 2.43, are not obtained by solving transport equations for the conditional quantities. Instead, integral inversions are used to obtain the conditional averages/filtered. More details about the formulation and the implementation of CSE/DCSE are provided in Chapter 3. CSE/DCSE has been applied successfully on premixed flames [48], non-premixed flames [49] and partially premixed flames [8]. The inclusion of chemistry has evolved from using simple chemistry [47] to flamelet tabulation [50] reaching detailed tabulated chemistry [51]. In principle, CSE/DCSE has no limitation regarding its performance at different turbulent combustion regimes with reasonable computational cost, which makes it a promising approach for further investigations in more complex cases such as spray combustion and pollutant formation, such as soot and (NO_x).

2.5 Turbulent Lifted Jet flame Stabilization

The phenomenon of flame lift-off is observed when the flame stabilizes at a distance away from the nozzle exit, as shown in Fig. 2.2. An important characteristic of the lifted flame is the lift-off height. It is defined as the distance between the burner rim and the lowest point of the flame base. The lowest point of the flame base is well-distanced from its axis, and is found to be unsteady with high frequency of fluctuations. Due to these high fluctuations, experimental measurements are difficult to perform [52]. An example of the lifted turbulent jet flame is presented in Fig. 2.3. It is noticed that the lift-off height increases linearly as the jet velocity increases in contrast to what is found in laminar lifted flames [52]. In both cases, flame extinction takes place when a certain critical velocity is exceeded.

The motivation of using lifted flames is to conserve the durability of the fuel nozzle due to

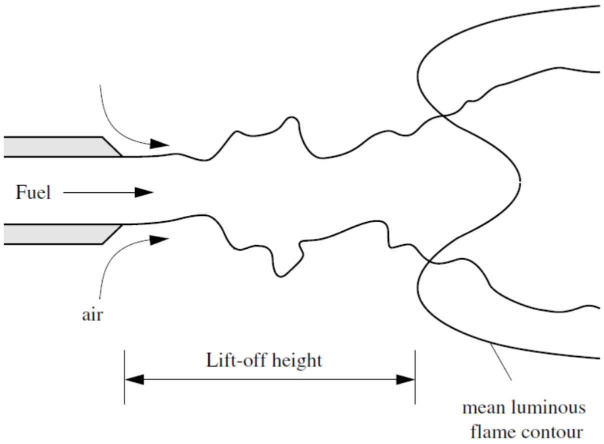

Figure 2.2: Schematic representation of a lifted jet diffusion flame, reproduced from [6]

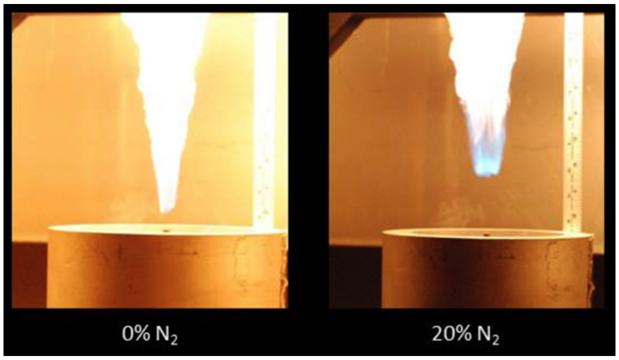

Figure 2.3: Pure ethylene flame luminosity in comparison to high level (20% by mole fraction) dilution of nitrogen, reproduced from [53]

lower damage to its material, and to allow for higher energy production due to higher operational velocity. Due to the complex transient phenomena involved, current combustion models struggle to give accurate and consistent predictions of lift-off height and extinction. There is a crucial need for the development of computational tasks capable of reproducing these phenomena.

Many theories have been investigated to describe and explain the lifted flame stabilization mechanisms. These theories include the premixed flame theory [54], the critical scalar dissipation concept [55], and the large eddy concept [56]. Detailed reviews can be found in references [7, 57]. Auto-ignition can also be considered as a lifted flame stabilization mechanism when a hot co-flow is present. This mechanism has been investigated experimentally by Cabra et al. [58, 59] and numerically by Yoo et al. [60].

2.5.1 The premixed flame theory

This approach is first proposed by Wohl et al. [54] who demonstrates that the flame base stabilizes itself at the location where the burning velocity is equal to the mean flow velocity. Vanquickenborne and van Tiggelen confim this flame stabilization theory experimentally using measurements applied to turbulent methane jets [61]. Futher, Vanquickenborne and van Tiggelen find that fuel and air are fully premixed at the base of the lifted flame which promotes the premixed flame theory. Additionally, in other measurements, a considerable amount of air is entrained upstream of the flame base [62]. More recent experimental findings question the assumption of the premixed flame propagation, because it means that the premixed flame front cannot propagate against the local flow velocity for long periods of time [63].

2.5.2 The critical scalar dissipation concept

This concept is also called flamelet quenching (extinction), first proposed by Peters and Williams [55]. It is postulated that there is not enough residence time upstream of the flame base to achieve a uniform mixture in time and space. In contrast to the premixed flame theory, the flame is lifted if the probability of burning flamelets calculated from the integral over the PDF of the scalar dissipation rate is below a certain critical value. This means that the reaction zone is displaced downstream to the location of the critically low value of scalar dissipation rate. One of the flaws of this approach is that it ignores the mixing that takes place partially upstream to the flame base according to Pitts [63].

2.5.3 The large eddy concept

This concept adopts the idea that the large turbulent scales are responsible for stabilizing the flame at a distance away from the rim [56]. Such a mechanism assumes that the large vortices entrain the hot products into the edges of the jet to ignite the combustible mixture. Accordingly, the flame lift-off is due to the rapid mixing between the products and the unburnt mixture where there is no adequate time to start ignition. However, this model is not consistent with the experimental investigations carried out by Pitts [63].

2.5.4 Partially premixed flame theory

Recent studies indicate that the lifted flame propagation is in the partially premixed mode. This results in the partially premixed flame propagation mechanism. An experimental investigation of lifted methane flames concludes that the governing stabilization mechanism in modelling lifted flames is the partially premixed turbulent velocity approach, while scalar dissipation rate measurements show that the mechanism of the diffusion flame extinction is not supported [64]. The results obtained by Stårner et al. [65] at the base of a methane jet flame have shown mixed characteristics of premixed and diffusion flames. This is supported by the experimental observations of Su et al. [66] which indicate the consistency between the observed scalar and velocity fields and the large scales contributions as well. To model such a flame numerically, the model should have an accurate description of both pure premixed and pure non-premixed flames. This kind of combination is first investigated though the flamelet model. Bradley et al. [67] are the first to apply this strategy numerically with a model based on the premixed turbulent flame propagation but considering the flammability limits, as well. Then a modification is considered to evaluate the mean heat release depending on mixture fraction and progress variable values. The agreement is acceptable between the predicted lift-off heights and the experimental data but the problem is that the model is tending to be fully premixed most of the time. Some modifications are provided regarding the turbulence model and the temperature closure order which resulted in better predictions [68]. Another model based on two scalars, mixture fraction and G, is proposed by Müller et al. [69]. The G-equation is used to describe the flame propagation with the laminar burning velocity as a function of mixture fraction. The same model is modified by Chen et al. [70] and both of them obtained good agreement with the corresponding experimental data. The issue is how to close the turbulent burning velocity term. Several *a-posteriori* DNS-CMC studies which examine the benefits of doubly conditioning are available for turbulent combustion with large temperature fluctuations [71], ignition-extinction [72, 73, 74] and Homogeneous Charge Compression Engines (HCCI) [75]. Recently, doubly CMC has been applied to spray combustion with flame lift-off [31] with good predictions, however the computational time and the model complexity still form an issue. The CSE model has been modified for the first time by Dovizio et al. [8] to describe partially premixed flame propagation through two conditioning parameters: the mixture fraction and the reaction progress variable. A series of lifted turbulent jet flames using RANS simulations are investigated. In the same scope, Dovizio et al. [8]

examine the effect of using different types of joint PDFs. Some terms were neglected in the progress variable transport equation. The RANS prediction of lift-off height were in good agreement within the experimental uncertainty with a larger noticeable discrepancy for the second flame (Re=12000). Nevertheless, some flame statistics available in the experimental studies could not be used due to the averaging nature of RANS. It is also believed that LES will bring a more realistic description of the turbulent flow and mixing fields of these complex flames.

2.6 Sandia methane-air piloted flames (D-F)

Modern combustion devices have to account for high fuel consumption rates at relatively high turbulence levels. This leads to operating outside or close to the limits of the stable combustion regimes. As a result, some instabilities such as local extinction and subsequent re-ignition may take place. These phenomena are described as finite rate chemistry effects which are referred to the turbulence-chemistry interaction that happens at the smallest turbulence scales. The high non-linearity of the chemical reaction rates makes it very challenging to recreate such phenomena numerically. To investigate such complex phenomena, the right description of turbulence, reliable selection of chemistry and combustion model, are necessary. The set of Sandia flames (D-F) shows an increasing level of local extinction with increasing Reynolds number value [76, 77]. It also provides a wide set of experimental data that allows for full examination of the reacting flow scalars in the conditional and unconditional state.

This series of flames has been investigated in the combustion literature using different approaches. The Lagrangian and the hybrid Lagrangian/Eulerian approaches, which rely on using stochastic particles, show in general good results, although their average time consumption is relatively high compared to the conventional Eulerian approach based-models. Flame D was first investigated by Lagrangian flamelet model by Pitsch and Steiner [78] in LES, followed by a comparison between steady and unsteady formulation applied on the same flame [79] using postprocessing. A joint scalar PDF method is applied on Flame (D-F) using reduced chemistry [80]. Another joint transported PDF method based on mixture fraction, scalar dissipation rate and burning indicator is carried out on Flame F [81]. In addition, hybrid techniques are used to simulate Sandia flames such as using finite volume [82] and finite-difference with Monte Carlo scheme [83, 84]. Many Multiple Mapping Conditioning (MMC) investigations are carried out successfully. Most of which are investigated in LES [85, 86, 87], while RANS investigations [88, 89, 90] show good results for the first moments, but not as good for the second moments compared to the experimental data. Some Lagrangian investigations are focused on studying specific parameters such as the time consumption of different parallel processing of chemistry retrieval [91], the effect of three different parallel strategies for redistributing the chemistry workload [92], the reduced finite rate chemistry [93] and the effect of the molecular diffusion [94]. The conditional moment closure (CMC) technique is applied in Lagrangian framework by Han and Huh [95] with first and second order closures on flames D and E. The results show an improvement in the conditional scalars obtained by the second order closure compared to the first order one, although the predicted second order moments do not look promising. The Eulerian investigations are not expected to have higher accuracy than the Lagrangian, but are less time consuming. Starting with the investigation of Ihme and Pitsch [96], they used an extension of the flamelet/progress variable (FPV) model that employs a presumed FDF to simulate Flame D and E in LES which obtained good results. A multi-environmental PDF transport model is used in Eulerian framework by Zhao [97] with Flame D and F in LES and managed to capture the local extinction in the flames. More Eulerian investigations include the steady flamelet appraoch that is used in LES and with detailed chemistry by Bretels et al. [98] to investigate Flame D and obtain reasonable predictions. The same flame is also investigated by Nunno and Mueller [99] in an LES study that is focused on chemistry effect and shows better predictions for the time scales for the pseudo-unsteady one dimensional manifold over the quasi-steady assumption. Further, Pant et al. [100] investigated the effect of different presumed PDF table integration approaches on different flamelet model predictions. Even in RANS, a comparison between the flamelet and EDC models is applied on Flame D which shows better results for steady laminar flamelet in OH predictions with less good predictions in CO [101]. CMC is used several times to simulate Sandia flames. It has been used by Roomena et al. [102] with first order closure to investigate Flame D with overall good agreement except at the fuel rich regions. That was referred to either discrepancy in chemistry or the conditional fluctuations that cannot be neglected. The latter possibility is discarded by a pretabulated doubly conditioning method carried out by Kronenburg and Kostka [73] that shows no major difference if the effect of conditional fluctuations is included. In agreement with the conclusion obtained in the Lagrangian based study [95], the second order closure employed by Kim and Huh [103] shows better predictions compared to the first order closure. Moreover, the detailed description of the mixing field provided in LES shows better results compared to RANS [104]. Further, good predictions and detailed qualitative analysis are introduced by Garmory and Mastorakos [105] using LES-CMC to predict Sandia D and F. It also shows high levels of local extinction that are captured by temperature and OH mass fraction predictions of Flame F. The second approach based on conditional moments with presumed PDF is CSE. It is initially tested for Flame D in LES with simplified chemistry which provided satisfactory predictions [47]. Then, another LES investigation with improved CSE model and tabulated detailed chemistry is carried out, and obtained good agreement with the experimental data for the same flame [51]. These results led to a comparative study between CSE and CMC applied on Flame D and E in RANS [106]. Comparable predictions are obtained for the first and second moments of velocity and mixture fraction of Flame D. Even for the major species, the conditional and unconditional profiles are comparable and in good agreement with experiments, while larger discrepancies in the minor species profiles can be seen for both models. In Flame E predictions, CSE shows better results. In addition, CSE is less computationally expensive than CMC. Both models were not able to produce good results for Flame F. A recent study based on Bushe's findings [107] that introduced a new model called Uniform Conditional State (UCS) is used with a multi-dimensional flamelet manifold to investigate Flame (C-F) through postprocessing [108]. The PDF structure is based on the experimental data to diminish the error due to PDF modelling. The predictions are in good agreement with the experimental data for temperature profiles for all flames, while the species mass fraction predictions of Flame E and F does not show the same success.

2.6.1 Summary

This chapter introduces information that is meant to form a solid background for the investigations of the current research. Different approaches of turbulence modelling are discussed keeping in mind that LES is mainly used in the current study, while RANS is selected for initial assessment only for a least squares numerical technique and an elaborate progress variable SDR model. Different turbulent combustion modelling strategies are shown including the infinitely fast chemistry models which have the advantage of low computational cost, but not practical in terms of model constants that need adjustment for every individual case. The flamelet model has been commonly applied to many combustion problems, but lacks the flexibility of being applicable outside the flamelet regime. CMC, transport PDF equation and MMC are not restricted to any combustion regime assuming appropriate closures are found for the additional terms produced for each method. CSE/DCSE has shown great performance in simulating different categories of flames without physical limitation and with reasonable computational cost. Therefore, the current investigations adopt LES-DCSE as a computational tool to investigate the complex reactive flow transitions observed in partially premixed flames. Lifted flames are investigated due to their importance in industry and their complexity. The partially premixed flame propagation theory has shown superiority amongst the other stabilization theories in terms of experimental observations. This promotes DCSE to investigate such flames. The local extinction and reignition found in Sandia flames (D-F) have been investigated with several models including Lagrangian and Eulerian approaches. The double conditioning formulation of DCSE makes it attractive to be assessed in simulating such flames.

Chapter 3

Doubly Conditional Source-term Estimation

The present chapter describes the main concepts upon which DCSE is established, the formulation of DCSE and the link with chemistry to close the mean/filtered chemical source term in the species transport equations. A description for the joint PDF/FDF is provided. The regularization technique and least squares method are explained. In addition, details on the chemistry reduction and tabulation are provided. Finally, an assessment for the behaviour of DCSE at the DNS limit is carried out prior to the LES investigation.

3.1 Formulation

The concept of CSE [47] relies on the same fundamental assumption as what is used in CMC [30]: the turbulent fluctuations found in the species mass fractions and temperature (or enthalpy) are correlated with the fluctuations of one or two key scalars such as mixture fraction in non-premixed combustion and a progress variable in premixed flames. Thus, if the species mass fractions and temperature (or enthalpy) are conditionally averaged on specific values of these key scalars, mixture fraction and/or progress variable, the fluctuations about the resulting conditional averages are significantly reduced compared to the turbulent fluctuations about the unconditional averages, to the level of being negligible. This also implies that additional sample spaces and averaging are introduced. The major advantage of this procedure is that the mean (in RANS) or filtered (in LES) chemical source term needed in the mean/filtered species transport equation may be determined by first order approximation using directly the conditional averages. This is commonly referred to as first order closure.

In the remainder of the current study, η and c^* represent the sample space variables of mixture fraction and progress variable, respectively. The progress variable, by itself, will be defined later in Section 3.3. For the moment, it is assumed that the progress variable varies between 0 and 1. In the context of double conditioning, the conditional averages are written as $\overline{f|\eta, c^*}$ where f may be any scalar quantity of interest such as species mass fraction or temperature. The vertical bar means conditional averaging of f on the two conditions located on the right hand side of the bar, i.e. in the present case, mixture fraction and progress variable. The conditional averages may be functions of space $\vec{x}$ and time t. In CSE/DCSE, the mean/filtered species transport equations are solved. Thus, the mean/filtered chemical source term, $\overline{\dot{\omega}_k}(\vec{x}, t)$ in any species k transport equation, as a function of the position vector $\vec{x}$ and time t, must be determined and can be found by the following expression,

$$\overline{\dot{\omega}_k}(\vec{x}, t) = \overline{\rho} \int_0^1 \int_0^1 \frac{\overline{\dot{\omega}_k|\eta, c^*}}{\overline{\rho|\eta, c^*}}(\vec{x}, t) \times \widetilde{P}(\eta, c^*, \vec{x}, t)\, d\eta\, dc^*, \tag{3.1}$$

where $\overline{\dot{\omega}_k|\eta, c^*}$ is the mean/filtered chemical reaction rate for species k conditionally averaged/filtered on η and c^* and $\widetilde{P}$ the joint PDF/FDF. Equation 3.1 is valid in the context of RANS and LES. On the right hand side of Eq.3.1, $\overline{\dot{\omega}_k|\eta, c^*}$ is calculated using the conditionally averaged/filtered species mass fractions and temperature, and the joint PDF/FDF is determined by a presumed form. Thus, Eq. 3.1 is in closed form as long as the conditionally averaged/filtered species mass fraction and temperature, and the presumed PDF/FDF form are known.

3.1.1 The presumed PDF/FDF

The selection of the PDF/FDF, that represents the characteristics of the key quantity, will have a significant impact on the predictions. In the current study, the joint PDF/FDF is obtained by

$$\widetilde{P}(\eta, c^*) = \widetilde{P}(\eta)\widetilde{P}(c^*|\eta), \tag{3.2}$$

where $\widetilde{P}(c^*|\eta)$ is the reaction progress variable PDF/FDF determined at the equivalence ratio corresponding to the mixture fraction value Z. The presumed β-PDF is commonly selected in non-premixed flames [109, 49] in particular, as β functions are able to change shape from one (ordinary beta) or two peaks (modified beta) to Gaussian shapes [14]. In contrast, for turbulent premixed flames, the use of PDF, that is based on the solution of unstrained one dimensional laminar flame, is shown to perform better than the β-PDF [110, 111]. The PDF is calculated as follows

$$\widetilde{P}(c^*, x, t) = A\delta(c^*) + Bf(c^*) + C\delta(1-c^*), \tag{3.3}$$

where $f(c^*)$ is related to the solution of an unstrained laminar premixed flame using

$$f(c^*) = \frac{1}{\nabla c^*}, \tag{3.4}$$

and its shape should be defined at a specific equivalence ratio value ϕ. The coefficients A, B, and C are obtained using the mean/filtered progress variable, $\widetilde{c}$, and variance $\widetilde{c''^2}$ as follows

$$C = \frac{\widetilde{c} - \widetilde{c^2}}{I_1 - I_2}, \tag{3.5}$$

$$B = \frac{\widetilde{c^2} I_1 - \widetilde{c} I_2}{I_1 - I_2}, \tag{3.6}$$

$$A = 1 - BI_0 - C, \tag{3.7}$$

where $I_0 = \int_0^1 f(c^*)dc^*$,$I_1 = \int_0^1 c^* f(c^*)dc^*$ and $I_2 = \int_0^1 c^{*2} f(c^*)dc^*$.

This formulation faces the problem that the PDF/FDF may rise to infinity as the value of the reaction progress variable c approaches 0 or 1. In addition, the laminar flame PDF works well only for high variance values. To overcome this problem, a modified version of the PDF/FDF of Bray et al. [112] is proposed by Jin et al. [111]. Prior to any CSE calculations, the presumed PDF/FDF is usually stored in look-up tables using the following integrals

$$(Pdc)_i = \int_{c_i - \frac{\Delta c}{2}}^{c_i + \frac{\Delta c}{2}} Pdc, \tag{3.8}$$

$$(Pdc)_0 = \int_0^{\frac{\Delta c}{2}} Pdc, \tag{3.9}$$

$$(Pdc)_n = \int_{1-\frac{\Delta c}{2}}^{1} Pdc, \tag{3.10}$$

where i represents the index of the discretized points (n points) in the reaction variable space. Equation (3.8) covers the interval between $1 < i < n-1$, and Eqs. (3.9) and (3.10) represent the first and last intervals that should be treated in a different way which is calculated using δ function. The formulation still allows switching back to $f(c^*)$ when needed. Jin et al. [111] describe four different possible cases of the truncated $f(c^*)$. These cases are

1. The laminar flamelet PDF with two delta functions at $c^* = 0, 1$.
2. The laminar flamelet PDF with only one delta function at $c^* = 0$ and the same laminar inner distribution till $c^* = c_2 < 1$.
3. The laminar flamelet PDF starting from $c^* = c_1 > 0$ and ending with a delta function at $c^* = 1$.
4. The inner distribution function from $c_1 > 0$ to $c_2 < 1$.

Each case of the four cases in Fig. 3.1 is selected to be used in a specific range of the mean/filtered progress variable and its variance. Also, β-function is used to model the PDF shape at the very lean of very rich mixtures of the progress variable PDF/FDF. This is because the unstrained laminar premixed flame failed to reach convergence at such mixtures. These two regions are found to be at a mixture fraction value smaller than 0.0143 and larger than 0.2, which is far from the flammability limits ($0.022 < Z < 0.11$) for methane-air combustion at atmospheric conditions [113]. Similar bounds are defined for Sandia flames composition which are 0.18 and 0.7 for the flammability limits of ($0.2 < Z < 0.6$). As a result, the conditional reaction rates are negligible outside the flammability limits. Therefore, the unconditional reaction rates will not be affected by the shape of the PDF/FDF in either regions of very lean or very rich mixture fraction.

The presumed joint PDF/FDF requires the mean/filtered and variance values of the mixture fraction and progress variable. These values are obtained from the solution of transport equations, as will be described later.

Given the expected low level of remaining fluctuations after double conditioning [71, 107], first order closure is applied to determine $\overline{\dot{\omega}_k|\eta, c^*}$, leading to the following approximation,

$$\overline{\dot{\omega}_k|\eta, c^*} \quad \simeq \quad \dot{\omega}_k(\overline{Y_i|\eta, c^*}, \overline{T|\eta, c^*}), \tag{3.11}$$

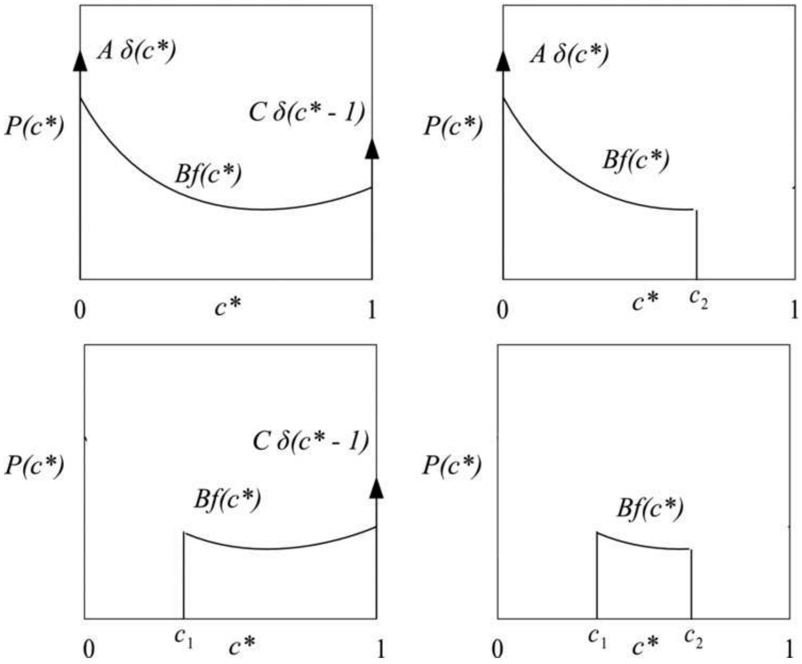

Figure 3.1: The four possible cases for the modified laminar flamelet PDFs, reproduced from [111]

where $\overline{Y_i|\eta, c^*}$ is the conditionally averaged/filtered mass fraction of species i, and $\overline{T|\eta, c^*}$ the conditionally averaged/filtered temperature. No additional transport equation is introduced for the conditionally averaged/filtered species mass fractions and temperature. In DCSE, the conditionally averaged/filtered species mass fractions and temperature are found by inverting the following integral

$$\widetilde{f}(\vec{x}, t) = \int_0^1 \int_0^1 \overline{f|\eta, c^*}(\vec{x}, t)\ \widetilde{P}(\eta, c^*, \vec{x}, t)\ d\eta\ dc^*, \tag{3.12}$$

where f represents any species mass fraction or temperature. In principle, the inversion of Eq. 3.12 would be performed for each chemical species in the selected mechanism. However, the inversion step is computationally intensive and at present, it is not feasible to perform the inversion of Eq. 3.12 for all species. Therefore, a different strategy is selected, that relies on chemistry tabulation. The use of detailed chemistry tabulation does not imply any flamelet assumption in turbulent combustion modeling and, for example, has been implemented in LES-CMC [104] and LES-transported PDF calculations [114]. Different chemistry tabulation techniques exist [115] and in the present investigation, the selected method is Trajectory Generated Low Dimensional Manifold (TGLDM) [116, 117]. The detailed reaction mechanism is dimensionally-reduced and, in the current study, tabulated to provide conditional reaction rates as functions of three parameters, η, $(Y_{\mathrm{CO_2}})$ and $(Y_{\mathrm{H_2O}})$. Further detail is provided in Section 3.3. Thus, only one conditional species mass fraction is required, $Y_{\mathrm{H_2O}}$, to retrieve all chemical source terms.

3.2 Inversion process

In order to perform the integral inversion, as shown in Eq. 3.12, it is necessary to define "ensembles" in which conditional averaged/filtered reactive scalars are assumed to be uniform. In particular, the conditional quantities are found to vary less in space in the radial direction compared to their unconditional counterparts [65, 30] in turbulent jet configurations. Thus, it is reasonable to assume the ensembles to be axial divisions of the cylindrical computational domain, which means that Eq. 3.12 is solved for each ensemble. Equation. 3.12 is re-written for each ensemble as

$$\widetilde{f}(x_j,t) = \int_0^1 \int_0^1 \overline{f|\eta, c^*}(t)\ \widetilde{P}(\eta, c^*, x_j, t)\ d\eta\ dc^*, \tag{3.13}$$

where j refers to the j-th point in the ensemble. In contrast to Eq. 3.12 that is written for any point in space, Eq. 3.13 is formulated for each ensemble in which the conditional averages are not functions of space. Each ensemble contains N number of points corresponding to the grid points. Equation 3.13 can be discretized and cast in matrix-vector form such that

$$A \cdot \vec{\alpha} = \vec{b}, \tag{3.14}$$

where A is the integrated joint PDF/FDF matrix of dimensions (N x M) where M is the number of bins in the combined mixture fraction/progress variable space, $\overrightarrow{\alpha}$ is the conditional averaged/filtered scalar vector of size M for a given ensemble, and $\overrightarrow{b}$ is the unconditional averaged scalar vector of size N. Equation 3.14 is a Fredholm integral of the first kind resulting in an ill-posed system as it does not satisfy the definition of well-posed system provided by Hadamard [118]. This means that solution of Eq. 3.14 is very sensitive for any perturbation in the inputs (i.e. a small perturbation in $\vec{b}$ or $\widetilde{P}$ will lead to large changes in $\vec{\alpha}$). Therefore, a regularization technique is required to obtain a stable and unique solution from such system.

Examples for such techniques include Truncated Singular Value Decomposition (TSVD) [119] and Tikhonov regularization methods [120]. The advantage of Tikhonov regularization over TSVD is that it is characterized by a continuously-variable degree of regularization. Through an investigation of a non-premixed turbulent methane-air flame which involves a Bayesian analysis to the inversion process, the zeroth order Tikhonov was compared to the first order Tikhonov [121]. The first order method shows superiority over the zeroth order for not requiring any additional storage and the independence on previous time steps. However, the smoothing matrix needs to be defined for each simulation which makes it more complicated, especially with two conditioning variables. The zeroth order Tikhonov regularization method is found to give a good approximation of the exact solution which makes it a good choice for the present work. It involves solving the following minimization problem

$$\vec{\alpha} = \arg\min\Big\{\Big\| \mathbf{A}\vec{\alpha} - \vec{b} \Big\|_2 + \lambda^2 \Big\| \vec{\alpha} - \vec{\alpha}_0 \Big\|_2\Big\}, \tag{3.15}$$

where λ is the regularization parameter, $\vec{\alpha}_0$ *a priori* knowledge of the solution, and $\|..\|_2$ represents the L-2 norm operator. The *a priori* knowledge can be selected to be a one-dimensional unstrained laminar premixed flame solution [111, 122], or using the previous time step solution [50]. As the final solution is found not to depend on the *a priori* knowledge, the latter is adopted in the current simulations for simplicity. An initial value of zero is set when the simulation starts.

The regularization parameter may be obtained from the L-curve [123]. This requires evaluating the norm of the solution, and the norm of the residual at each time step then finding the region of minimum error which is found at the corner of the L-shaped curve. This process is hard to be automated. Thus, the approach proposed by Grout et al. [50] is applied. This approach is simple and involves calculating the regularization parameter using

$$\lambda^2 = \frac{Tr(A^T A)}{Tr(I)}, \tag{3.16}$$

where Tr is the trace of the matrix and I is the identity matrix. No change in the order of magnitude is found when the regularization parameters obtained by Eq. (3.16) are compared with those determined for the L-curve [50]. The problem is that, it does not guarantee the positivity of the calculated conditional mass fractions which is non-physical. However, the non-physical values are observed in the very fuel-rich regions where the chemical activity can be neglected and the errors obtained in this region will not affect the turbulent combustion modelling process [124].

To overcome this undesired behavior, Bushe and Steiner [124] replace all negative values by zeros in the solution vector $\vec{\alpha}$ and then apply a rescaling process. The rescaled values of the solution vector noted by $\overrightarrow{\alpha}_{\text{final}}$ are determined using

$$\overrightarrow{\alpha}_{\text{final}} = \overrightarrow{\alpha}\,\frac{\sum_j \widetilde{Y}_k(x_j,t)\int\int \overline{Y_k|\eta,c^*}\,\widetilde{P}\,(\eta,c^*;x_j,t)\,d\eta dc^*}{\sum_j\left(\int\int \overline{Y_k|\eta,c^*}\,\widetilde{P}(\eta,c^*;x_j,t)d\eta dc^*\right)^2}, \tag{3.17}$$

The scaling factor, $S = \frac{\overrightarrow{\alpha}_{\text{final}}}{\overrightarrow{\alpha}}$, is monitored at each time step. It is found to be in the following range, $0.88 \leq S \leq 1.00025$, which shows the small impact of rescaling.

The conventional CSE simulations involve the use of a numerical technique to carry out the matrix inversion process, as shown in Eq. 3.14. The LU-decomposition is the commonly used technique side by side with Tikhonov regularization method in singly CSE simulations [125, 48, 49], and DCSE [8]. LU-decomposition is based on the principle of matrix pivoting and decomposing the system of equations into two systems which are easy to solve by forward and backward substitution. It also implies that the matrix must be square to factorize. Thus, the sides of the Eq. 3.14 will be multiplied by the transpose of matrix A as follows

$$A^T A\overrightarrow{\alpha} = A^T\overrightarrow{b}. \tag{3.18}$$

Then the equation can be re-written as

$$A^*\overrightarrow{\alpha} = \overrightarrow{b^*}, \tag{3.19}$$

following the regularization method, the right hand side will be

$$\overrightarrow{b^*} = \overrightarrow{b^*} + \lambda\overrightarrow{\alpha_0}. \tag{3.20}$$

Then matrix A^* is decomposed as $PA^* = LU$, where P is a permutation matrix, L unit lower triangular matrix, U upper triangular matrix. This leads to presenting the original system (3.19) in the form of a pair of triangular systems as

$$L\overrightarrow{y} = P\overrightarrow{b^*}, U\overrightarrow{\alpha} = \overrightarrow{y}, \tag{3.21}$$

which are solved by forward and backward substitution, respectively.

Although LU-decomposition is considered a direct technique of solving system of simultaneous linear equations which will avoid any truncating or rounding errors encountered in indirect techniques, the conditioning number of A^*, which is the square of that obtained for matrix A, will increase the sensitivity to any perturbation. Moreover, the matrix-vector and matrix-matrix multiplication processes are considered time consuming, especially in the case of doubly conditional calculations.

Recently, another numerical technique for solving least squares problems, is used in CSE [126]. According to Tsui and Bushe [126], there are at least two sources of errors in the inversion process; the first is the modelling errors that can be encountered in the PDF/FDF matrix, and the second is due to using zeroth order Tikhonov regularization using the laminar flamelet solution. The errors generated from the iterative method are relatively small compared to the formerly mentioned errors.

The LSQR algorithm is first proposed by Paige and Saunders [127]. The method proved its efficiency and stability in solving large, sparse, and ill-conditioned linear systems [128]. In addition, it is recommended for over-determined or under-determined systems [129]. LSQR is based on the bidiagonalization process developed by Golub and Kahan [130]. A parallel version of LSQR method is developed by Lee et al. [131] for the purpose of solving the systems of equations found in the seismic tomography field. The iterative nature of the technique enables the use of multiple processors in parallel, which is significantly useful in case of large matrices of order (10,000) or higher. Tsui and Bushe [126] performed two separate tests after modifying the technique to be able to account for the initial solution $\overrightarrow{\alpha_0}$ which improved convergence rate by 10%, which contributes in saving more time.

As the inversion is carried out, the $\overline{Y_{\mathrm{H_2O}}|\eta, c^*}$ values are obtained and used to evaluate the conditional reaction rates from the chemistry tables. Eventually, the DCSE loop closes by calculating the filtered unconditional reaction rates using Eq. 3.1. The solution procedure can be summarized in the form of flow chart, as shown in Fig. 3.2. Conservation of mass is enforced through the solution of the transport equations in the LES code and in the generation of the chemistry tables.

3.3 Chemistry reduction and tabulation

Chemical reaction mechanisms play a crucial role in calculating the mean/filtered chemical source term in the investigation of most of turbulent combustion models. For methane-air combustion, GRI-MECH 2.11 and GRI-MECH 3.0 are considered the two commonly used detailed mechanisms [132, 133]. The first one includes 49 species and 277 elementary reactions, while the second includes 53 species and 325 elementary reactions. Using detailed chemistry is expected to provide high accuracy in predictions, but will cost a relatively massive increase in computational time. This may be referred to solving the chemical source term for each reactive cell at each time step. Moreover, the generated governing ordinary

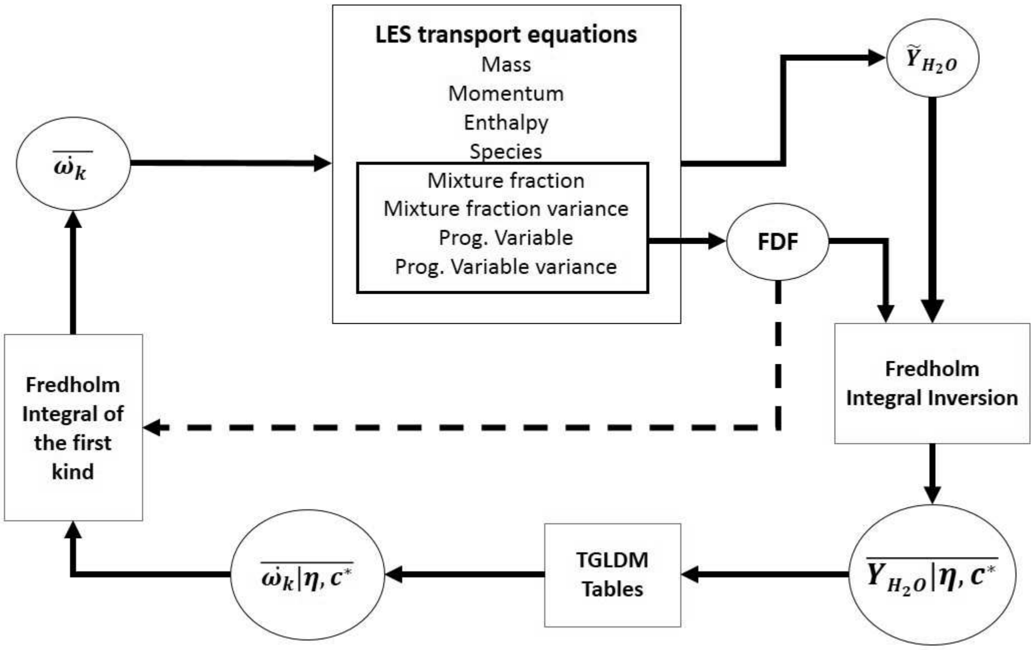

Figure 3.2: Flow chart of solution procedure that involves DCSE calculations

differential equation (ODE) system is stiff, because of the different time scales included in the chemical reactions. This requires a very small time step to guarantee the numerical stability [134]. For this reason, the chemistry is tabulated to reduce the dimensions of the mechanism and to keep the inclusion of the detailed chemistry, but represented as a function of lower number of parameters. The method adopted for the current work is the Trajectory Generated Low Dimensional Manifold (TGLDM), proposed by Pope and Maas [135]. Different manifolds are defined depending on the number of reduced dimensions. The manifold is comprised of reaction trajectories that are generated from the boundaries of the manifold. Each trajectory evolves, until it reaches the chemical equilibrium condition. The evolution of trajectories is based on solving the following differential equation using numerical integration,

$$\frac{\partial}{\partial t}Y_k = \dot{\omega}_k, \tag{3.22}$$

The initial conditions for Eq. 3.22 can be calculated by applying a mass balance on the involved elements and the concept of the ”extreme-value-of-major-species”, which is

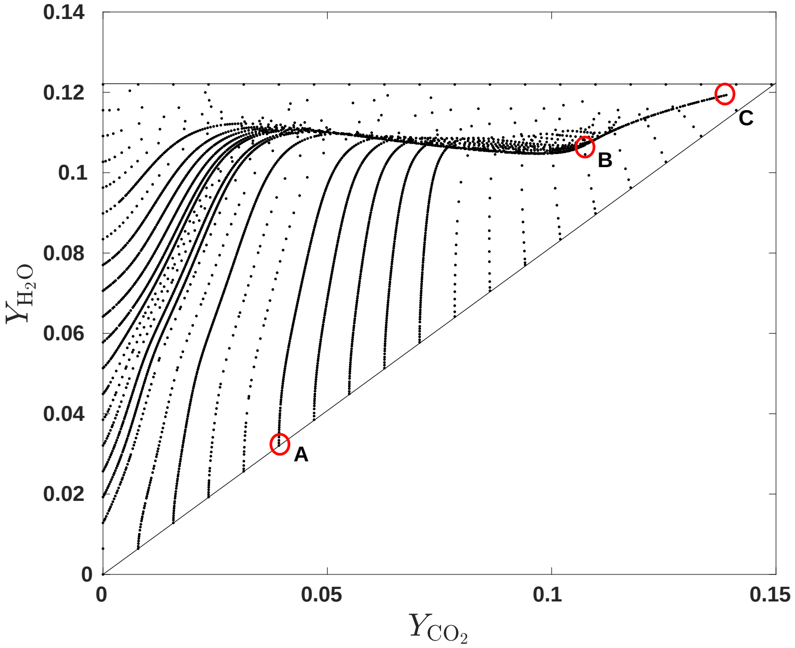

Figure 3.3: The stoichiometric reaction manifold showing the solution points of Eq. 3.22 for each reaction trajectory ($\eta = 0.055$), where point A represent an initial trajectory point, B the leading point of the equilibrium trajectory and C the equilibrium point of the current manifold.

used by Pope and Maas [135]. The maximum values of each species mass fraction can be estimated by

$$Y_e(j) = \sum_{i=1}^{n_e+2} Y(i) f_{j/i}, j = 1...n_e, \tag{3.23}$$

where $f_{j/i}$ is the mass fraction of element j in species i and $Y_e(j)$ is the mass fraction of element j. Then, linear programming techniques [136] can be used to identify the realizable region and specify the initial points of the trajectories.

An example for a generated manifold is presented in Fig. 3.3, where point A represents one of the initial composition points that are evaluated on the boundaries of the realizable region. The reacting mixture at point A undergoes a temporal evolution, until it reaches the equilibrium trajectory, represented by the curve BC, where the mass fraction of water,

Y_{H_2O}, is directly linked to the mass fraction of carbon dioxide, Y_{CO_2}, before reaching equilibrium at C. The resulting chemistry tables include three dimensions η, Y_{CO_2} and Y_{H_2O}. The mass fractions of CO_2 and H_2O are selected to be the variables by which the resulted manifolds are stored in the form of structured tables. This selection is made because the formation time of carbon dioxide and water is relatively long compared to the other species [135, 51]. As c^* is selected to be a normalized mass fraction of CO_2, the number of dimensions can be further reduced to three dimensions η, Y_{CO_2} and Y_{H_2O} instead of including c^* as the fourth dimension. After the calculation of trajectories is completed, the redundant points can be removed to avoid any unnecessary increase in table size. Delauney triangulation technique [137] is employed to easily locate points within the manifold, as seen in Fig. 3.4.

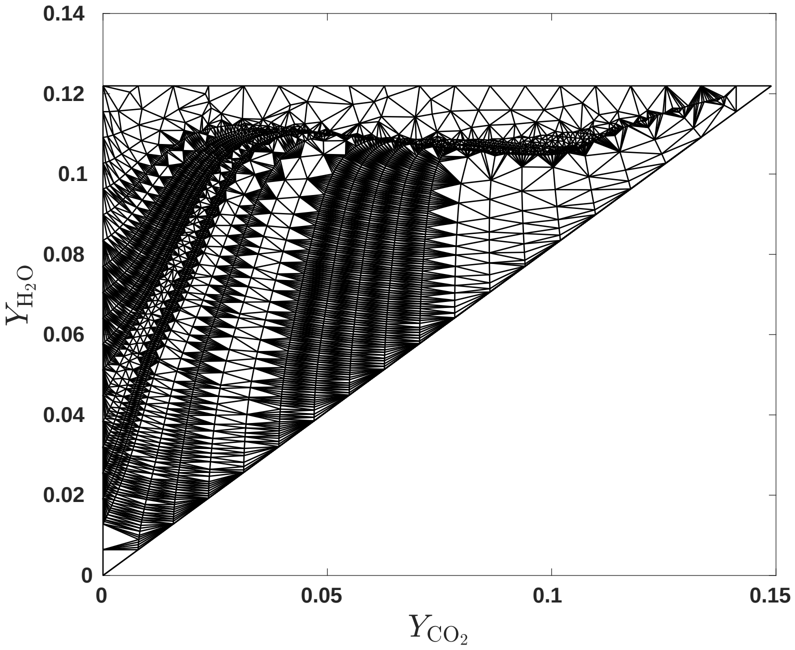

Figure 3.4: Graphical presentation for Delauney triangulation of the stoichiometric reaction manifold of the methane-air mixture ($\eta = 0.055$)

3.4 Behavior in the DNS limit prior to LES

CSE/DCSE has not been developed for any particular simulation framework, RANS or LES. There is no constant or model parameter in CSE related to RANS or LES. There is no additional equation solved for CSE/DCSE, and therefore, for example, no additional mixing term that needs to be closed at the SGS level in LES.

As presented in Sections 3.1 and 3.2, the main components of CSE/DCSE are the integral inversion process and the presumed (joint) FDF. When the LES filter is further decreased to the point of resolving all turbulent length and time scales, the LES-DCSE calculations are expected to reproduce the DNS solution. To the authors' best knowledge, only a few studies have examined this aspect in the context of turbulent premixed combustion, for the flamelet approach [110] and PDF methods [138]. In the current framework of partially-premixed combustion and DCSE, some discussion is now provided on how DCSE would behave in an LES approaching the DNS limit. Starting with the inversion process, in the DNS limit, the joint FDF tends to a delta function at one point in space. As a result, the matrix A of integrated joint FDF in Eq. 3.14 is only made of zeros and ones. Consequently, the inversion process becomes trivial and the filtered unconditional species mass fractions are equal to the tabulated conditional species concentrations at given values of $\widetilde{Z}$ and $\widetilde{c}$. This means that the DNS limit is reproduced as long as the joint FDF behaviour is adequately modelled by the presumed FDFs and the tabulated chemistry is accurate.

There seems to be a consensus on the use of the β function and its accuracy to approximate the FDF of mixture fraction, in particular for two-stream mixing configurations at atmospheric pressure [139] like what is found in the selected lifted flames. The laminar flamelet FDF selected in the present paper has been shown to reproduce the laminar burning velocity of a one dimensional (1D) laminar premixed flame (Fig. 2 of [140]). Thus, the same behavior is expected for the present simulations.

For additional testing, $\widetilde{Z''^2}$ and $\widetilde{c''^2}$ are set to a very small value of 10^{-6}, the joint FDF becomes a delta function and the resulting matrix A in the regularization process (Eq. 6) is sparse made of zeros and ones. These very small values of variance were imposed artificially only for testing.

The last aspect is the tabulated chemistry that will be the dominant effect controlling the behavior of the flame in the DNS limit. In the current work, the selected tabulation method is TGDLM using 0D autoignition trajectories generated from GRI Mech 2.11. Other chemistry tabulation methods are possible, but were not tested in the present work. This choice is motivated by the fact that the selected lifted turbulent flames start from a non-premixed configuration and at the flame base, large mixture fraction (or equivalence ratio) gradients are expected to be present. Thus, the assumption of the flame being composed of laminar

premixed flamelets may not be valid in the present flames. Further, the TGLDM tabulated chemistry has been tested for a 1D unstrained laminar premixed flame and laminar diffusion flamelets, both using methane-air chemistry [117]. These previous results show that the TGLDM chemistry could reproduce the major species concentrations accurately, but larger discrepancies could be seen for H_2 and OH mass fractions. This is explained by the lack of diffusion term in the governing equations of the current 0D trajectories. For the diffusion flamelets, the agreement for the species mass fractions between TGLDM and flamelet profile is found to be good for low scalar dissipation rates and larger differences are observed for higher scalar dissipation rates. This occurs due to no direct effect of strain included in the tabulation. Consequently, if there is a discrepancy in reproducing the DNS limit of the selected lifted flame, it will most likely come from the tabulated chemistry.
Finally, a 1D unstrained laminar methane-air premixed flame is simulated at stoichiometric conditions using the same DCSE routines and TGLDM tables as those implemented in the current work. The grid spacing is equal to 0.04 mm with a finer progress variable sample space grid (50 points). The predicted laminar flame is found to be 0.33 m/s which is in excellent agreement with the experimental value of 0.35 m/s [141]. Thus, it is fair to conclude that the present LES-DCSE formulation is capable of reproducing the main elements of the DNS limit.

3.5 Summary

DCSE is the model used in the current study to simulate the partially premixed characteristics in combustion. It is based on two assumptions; the first is that the fluctuations of two key scalars can be correlated to the fluctuations of the reactive scalars in the reactive flow, and the second is that the fluctuations about the conditional averaged/filtered quantities can be neglected compared to the fluctuations about the unconditional ones. The model is based on using Fredholm integral of the first kind to get the chemical reaction rates by integrating the conditional reaction rates multiplied by a presumed joint PDF/FDF over the sample space of mixture fraction and progress variable. The joint PDF/FDF is obtained as the multiplication of the mixture fraction and progress variable PDF/FDFs, where β-function is used for mixture fraction and the modified laminar flame PDF is used for the progress variable PDF/FDF. The computational domain is divided into a number of ensembles on which DCSE procedure is applied. The procedure involves a regularization process for an essential matrix-vector inversion that results in least squares problem. Zeroth order Tikhinov method is selected for regularization, and LSQR or LU decomposition can be used to solve the least squares problem. GRI-MECH 2.11 is dimensionally reduced and tabulated using TGLDM technique which produced three dimensional chemistry tables. A one-dimensional unstrained laminar premixed flame simulations are run using DCSE and the stoichiometric TGLDM table to assess its ability to produce good results at DNS limit. The results show that DCSE is able to reproduce the laminar flame speed with discrepancy of 5%.

Chapter 4

Assessment of least squares method and the progress variable SDR closure using RANS simulations

Prior to the LES calculations, RANS simulations of a series of methane-air turbulent lifted flames, implemented by DCSE, are used to provide insight for the impact of using the LSQR technique and more detailed progress variable SDR closure in comparison with the counterparts that are used in previous RANS-DCSE simulations performed for the same flames [8]. First, the Favre-averaged transport equations involved in the RANS calculations are presented. Next, a detailed description for the detailed SDR closure is provided. Then, the experimental setup and the corresponding computational domain are given. Finally, the results are discussed.

4.1 Favre-averaged transport equations

Transport equations of mass, momentum, enthalpy and species are solved. Seven species, CH_4, O_2, CO_2, H_2O, CO, OH and H_2, are determined by their respective transport equations [14]. These seven species are selected as being the main contributors of enthalpy changes. Further, a transport equation of mean mixture fraction is solved as

$$\frac{\partial(\overline{\rho}\widetilde{Z})}{\partial t} + \frac{\partial}{\partial x_i}(\overline{\rho}\widetilde{u}_i\widetilde{Z}) = \frac{\partial}{\partial x_i}\left(\overline{\rho D\frac{\partial Z}{\partial x_i}} - \overline{\rho}\widetilde{u_i''Z''}\right), \tag{4.1}$$

while the Favre-averaged equation for the variance of the mixture fraction is

$$\frac{\partial(\overline{\rho}\widetilde{Z''^2})}{\partial t}+\frac{\partial}{\partial x_i}(\overline{\rho}\widetilde{u}_i\widetilde{Z''^2})=-\underbrace{\frac{\partial}{\partial x_i}\left(\overline{\rho u_i'' Z''^2}\right)}_{\text{turbulent transport}}+\underbrace{\frac{\partial}{\partial x_i}\left(\overline{\rho D\frac{\partial Z''^2}{\partial x_i}}\right)}_{\text{molecular diffusion}} \\ -\underbrace{2\overline{\rho}\widetilde{u_i''Z''}}_{\textit{production}}-\underbrace{\overline{\rho}\widetilde{\chi}_z}_{\text{dissipation}}, \tag{4.2}$$

where the gradient assumption is used to close the turbulent flux, $\widetilde{u_i''Z''}$, as

$$\widetilde{u_i''Z''}=-D_t\frac{\partial\widetilde{Z}}{\partial x_i}. \tag{4.3}$$

In the present work, differential diffusion is neglected as it has a minimal impact as obtained from the simulation results in [142]. The reaction progress variable represents the degree of consumption of the fuel. It has a value that ranges from zero in fresh gas (with no products) to unity for the completely burnt gases (with no reactants presented at that location).
In the present work, the progress variable is defined as

$$c(\eta)=\frac{Y_{CO_2}}{Y_{CO_2}^{eq}(\eta)}, \tag{4.4}$$

where $Y_{CO_2}^{eq}(\eta)$ is the equilibrium value of the mass fraction of CO_2, ideally obtained when complete combustion takes place, which is a function of equivalence ratio. The governing transport equation of the mean progress variable is

$$\frac{\partial(\overline{\rho}\widetilde{c})}{\partial t}+\frac{\partial}{\partial x_i}(\overline{\rho}\widetilde{u}_i\widetilde{c})=\frac{\partial}{\partial x_i}\left(\overline{\rho D\frac{\partial c}{\partial x_i}}-\overline{\rho}\widetilde{u_i''c''}\right)+\overline{\dot{\omega}_{tot}}, \tag{4.5}$$

where D is the reaction progress variable diffusivity. The turbulent scalar flux is closed using a gradient assumption as used with the mixture fraction equation,

$$\widetilde{u_i''c''}=-\frac{\mu_t}{Sc_t}\frac{\partial\widetilde{c}}{\partial x_i}. \tag{4.6}$$

The mean total progress variable source term is decomposed into

$$\overline{\dot{\omega}_{tot}}=\overline{\dot{\omega}_p}+\overline{\dot{\omega}_{np}}+\overline{\dot{\omega}_{cd}}+\overline{\dot{\omega}_c}, \tag{4.7}$$

where $\overline{\dot{\omega}_p}$ and $\overline{\dot{\omega}_{np}}$ are the premixed and non-premixed mode contribution terms, respectively, $\overline{\dot{\omega}_{cd}}$ the cross dissipation term, and $\overline{\dot{\omega}_c}$ the chemical source term of the progress variable. The first three terms in the right hand side of Eq. 4.7 are presented due to the dependence of the reaction progress variable on the mixture fraction. The first term, $\overline{\dot{\omega}_p}$, is zero because of the linear relation between c and Y_{CO_2} (Eq. 4.4). The second term, $\overline{\dot{\omega}_{np}}$, involves a second derivative with respect to Z that tends to zero except for $Z \simeq Z_{St}$ [39]. As this term is neglected for simplicity in the previous simulations [9], it is neglected in the current simulations to keep the same conditions for comparison. Regarding the third term, $\overline{\dot{\omega}_{cd}}$, the cross dissipation term is neglected in the present investigation according to the DNS simulations of Ruan et al. [143], that have shown that its order of magnitude is smaller than the other two terms, and the conclusion of Domingo et al. [144].
The governing equation of the variance of reaction progress variable is

$$\begin{aligned}\frac{\partial(\overline{\rho}\widetilde{c''^2})}{\partial t} + \frac{\partial}{\partial x_i}(\overline{\rho}\widetilde{u}_i\widetilde{c''^2}) = &- \underbrace{\frac{\partial}{\partial x_i}\left(\overline{\rho u_i'' c''^2}\right)}_{\text{turbulent transport}} + \underbrace{\frac{\partial}{\partial x_i}\left(\overline{\rho D \frac{\partial c''^2}{\partial x_i}}\right)}_{\text{molecular diffusion}} \\ &- \underbrace{2\overline{\rho}\widetilde{u_i'' c''}}_{\text{production}} - \underbrace{\overline{\rho D \frac{\partial c''}{\partial x_i}\frac{\partial c''}{\partial x_i}}}_{\text{dissipation}} + \underbrace{\overline{2c''\dot{\omega}_c}}_{\text{source-term}} ,\end{aligned} \tag{4.8}$$

The gradient diffusion assumption is used for the turbulent fluxes. The last term in Eq. 4.8 represents a correlation between the chemical source term and the fluctuations in the progress variable. This term can be determined using the following formulation

$$\overline{c''\dot{\omega}_c} = \overline{(c-\tilde{c})\dot{\omega}_c} = \int_0^1\int_0^1 (c^* - \tilde{c})\overline{\dot{\omega}_c|c^*,\eta}\tilde{P}(c^*,\eta)dc^*d\eta, \tag{4.9}$$

where $\overline{\dot{\omega}_c|c^*,\eta}$ is obtained from DCSE and the TGLDM tables using

$$\overline{\dot{\omega}_c|c^*,\eta} = \frac{\overline{\dot{\omega}_{CO_2}|c^*,\eta}}{\overline{Y_{CO_2}^{eq}|\eta}} \tag{4.10}$$

The other unclosed term, $\overline{\rho D \frac{\partial c''}{\partial x_i}\frac{\partial c''}{\partial x_i}}$, is the averaged SDR term which will be covered in the next Section.

4.2 The progress variable SDR closure

The SDR, $\widetilde{\chi}$, is considered a measure for the decay of either the mixture fraction or the reaction progress variable fluctuations estimated by their variance. An analogy is used between the SDR and the dissipation rate of the TKE [6], as they are found to play similar role (dissipation). That led to a relation between the SDR and the characteristic turbulent mixing time. This simple algebraic closure is introduced by Mantel and Borghi [145]. It is selected in the current work to model the mixture fraction SDR as follows

$$\widetilde{\chi}_Z = C_\chi \frac{\varepsilon}{k} \widetilde{Z''^2}, \tag{4.11}$$

where C_χ is a constant of the model and has the order of magnitude of unity. This model, which is based on EBU hypothesis, is used in previous literature [125, 8] where it showed good predictions.

Dovizio and Devaud [9] compared different SDR models included in an study of a turbulent premixed V-shaped flame using CSE approach. They indicated that the highest discrepancies are obtained for the simple algebraic model, and found the main cause to be the absence of the effect of the turbulent flame speed in the model [9].
A reliable SDR model should take in account turbulent mixing, chemical reaction, molecular diffusion, and their interactions. Aiming to achieve these requirements, an advanced algebraic model is developed by Kolla et al. [10]. This model is derived for high Damköhler number turbulent premixed flames. This model is based on the leading order balance of an exact transport equation for $\widetilde{\chi_c}$, which includes the effect of dilatation, interaction of turbulence and scalar gradients, chemical reaction, and dissipation processes.
The model is formulated as follows

$$\widetilde{\chi_c} = 2\bar{\rho}\frac{1}{\beta'}([2K_{c^*} - \tau C_4]\frac{S_L}{\delta_L} + C_3\frac{\widetilde{\varepsilon}}{\widetilde{\widetilde{k}}})\widetilde{c''^2}, \tag{4.12}$$

where β' is model constant which is taken as 6.7, τ heat release parameter, K_{c^*} a model constant which can be calculated by

$$K_{c^*} = (\frac{\delta_L^0}{s_L^0})\frac{\int \{\rho N(\nabla \cdot u)\}_0^L f(c)dc}{\int \{\rho N\}_0^L f(c)dc}, \tag{4.13}$$

where δ_L^0 is the unstrained laminar thermal thickness (its selected value from experiments is 0.62 mm [146]), $f(c)$ the burning mode PDF, s_L^0 laminar flame velocity, N_L^0 the SDR in unstrained planar laminar flame. Selected values for τ and K_{c^*}/τ correspond to the selected value of mixture fraction. The other model constants C_3 and C_4 are estimated according to Chakraborty and Swaminthan [147],

$$C_3 = \frac{1.5}{1 + Ka^{-0.5}}, \tag{4.14}$$

$$C_4 = 1.1(1 + Ka)^{-0.5}, \tag{4.15}$$

where Ka is Karlovitz number which represents the ratio between the chemical time scale and the flow time scale and is taken to be 1.22 [146].

This model proved its physical realizability $\widetilde{\chi}_c \geq 0$ to be unconditional. The predictions obtained by this model were satisfactory compared with DNS data of turbulent premixed combustion [148, 149], which was ensured by the investigations of Dovizio and Devaud [9]. To account for the dependence of the reaction progress variable on the mixture fraction value through the partially premixed flame approach, Dovizio and Devaud [9] extended the formula of Kolla et al. [10] to have the model parameter as a function of the mixture fraction. The extended formula is presented as

$$\widetilde{\chi}_c(Z) = 2\bar{\rho}\frac{1}{\beta'}\left(\underbrace{2K_{c^*}(Z)\frac{S_L(Z)}{\delta_L(Z)}}_{\text{I}} - \underbrace{\tau(Z)C_4(Z)\frac{S_L(Z)}{\delta_L(Z)})}_{\text{II}} + \underbrace{C_3(Z)\frac{\widetilde{\varepsilon}}{\widetilde{k}}}_{\text{III}}\right)\widetilde{c''^2}, \tag{4.16}$$

where the first term, I, represents a correlation between dissipation and dilatation rates. The second term, II, represents the strain due to heat release. The third term, III, represents the correlation to the turbulent mixing time. The good predictions obtained for the stratified flame [9] formed a motivation to investigate its effect on modelling the turbulent lifted jet flame.

4.3 Experimental conditions

The experimental setup involved in the current investigation is a fuel jet of 5.4 mm diameter surrounded by approximately quiescent ambient air. The velocities provided for the fuel jet have an average value of 21, 37 and 60 m/s corresponding to the jet Reynolds numbers of 7,000, 12,000, and 19,500, respectively [12, 150, 13]. The flame extinction velocity for such a jet flame is found to be 90 m/s which is far enough from the values simulated. The experimental data includes the mean lift-off height at the three flames, reacting and non-reacting radial methane concentration profiles measured at four axial locations for the flame at Re=7,000, and axial methane concentration profile along the centerline at Re=7,000.

4.4 Computational details

The governing transport equations are solved using a finite volume low-Mach number pressure based approach. The employed solver is the open source CFD package of OpenFOAM using Pressure-Implicit with Splitting of Operators (PISO) algorithm for pressure corrections. The finite volume schemes used to solve the equations include: a first-order implicit time integration method for all transport equations, Total Variation Diminishing (TVD) and Normalised Variable Diagram (NVD) for fluxes.

4.4.1 Computational domain

The computational domain is similar to what was used by Dovizio et al. [8] as presented in Fig. 4.1. It is constructed in the form of cylindrical wedge of 1 cell thick running along the plane of symmetry. This wedge has an angle of 5^o, radius of 324 mm and length of 1080 mm. This 2-D grid consists of 22,400 cells. The grid is non-uniform to provide a higher grid density at the shear layer region. Based on the non-reacting velocity fluctuations provided for the lowest Re, the inlet turbulence intensity is set to 10%. The one-seventh power law, which is usually used to represent the average velocity profile for turbulent flows, is applied to provide an approximate velocity profile at the fuel inlet.

A relatively small velocity value is specified for air at the co-flow inlet. The ratio between the air velocity to jet velocity is set equal to 0.0005 which is much lower than the value specified experimentally to avoid any impact on the lift-off height that increases if the value of this ratio is higher than 0.002 [13]. The DCSE calculation requires dividing the computational grid into a specific number of ensembles of points. The ensembles are generated by dividing the computational domain using planes normal to the axial direction, taking advantage of the weak dependence between the conditional averages and the radial direction [30]. To avoid sharp changes in the conditional means, a small overlap of 3 mm is included between each two adjacent ensembles.

Each ensemble should satisfy the condition that the number of reactive cells per ensemble should be larger than the number of bins in the combined mixture fraction/progress variable sample space to avoid rank-deficient condition in the inversion problem. The number of ensembles used by Dovizio et al. [8] is employed in the current investigation, which is 3.

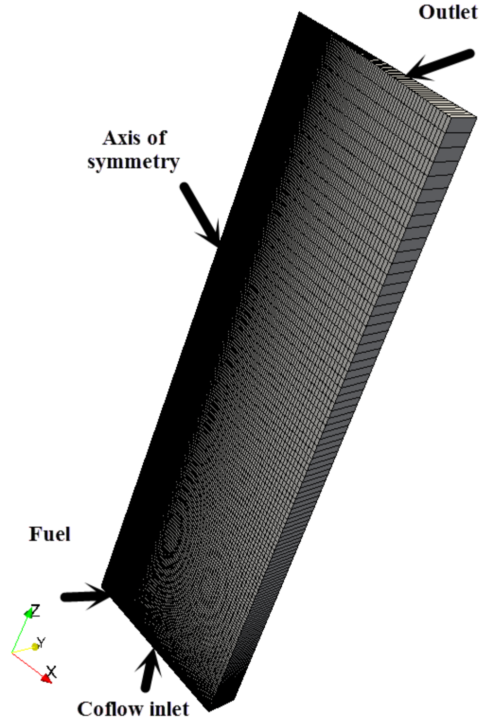

Figure 4.1: The computational domain developed for RANS simulations

4.4.2 DCSE initialization

Similar to Dovizio et al. [8], a rectangular box is defined which is 1 mm downstream from the jet exit with one side located along the centreline with length 100 mm and width in the radial direction of 20 mm. Values for carbon dioxide and water mass fractions are set to be close to the chemical equilibrium values.

4.5 Results

Through the following order, RANS simulations resulted in

1. The predictions obtained by the more detailed SDR [9] using the same computational domain and settings used by Dovizio et al. [8].

2. An assessment for using LSQR in DCSE instead of LU-decomposition which includes time consumption and accuracy.

The methane concentration provided by Schefer et al. [12] is evaluated as the measured methane number density normalized by the number density of pure methane at standard conditions of temperature and pressure (STP). This normalizing value is provided as (2.5×10^{19}) molecules/cm^3 [12]. Because the numerical model provides time-averaged methane mass fraction, $\overline{Y}_{CH_4}$, it can be converted to the normalized methane concentration used in the experiments [12] using the following expression

$$\overline{C}_{CH_4} = \frac{\overline{\rho}_{mix}\overline{Y}_{CH_4}N_A}{M_{CH_4}C_{CH_4STP}}, \tag{4.17}$$

where N_A is Avogadro's number, $\overline{\rho}_{mix}$ the time-averaged density of the mixture, C_{CH_4STP} is the number density of pure methane at STP conditions.

The predictions of radial methane concentration profiles are compared with the experimental data and previous results [8] in Fig. 4.2. As shown in Fig. 4.2, the predictions obtained for mean methane concentration C_{CH_4} remain in good agreement with the experimental data for the case of low Reynolds number (Re=7,000). Further, the axial methane concentration obtained by the current model shows better agreement with the experimental data at the region close to the jet outlet. In particular, the non-physical hump obtained by the simple SDR model [8] is not present, as shown in Fig. 4.3.

There are several approaches to estimate the lift-off height from the numerical results. Following the previous DCSE study [8], different lift-off height estimation criteria are considered: i) the height at which the mass fraction of OH becomes 0.0004 [60], ii) the height at which the mass fraction of OH becomes 0.0006 [58], iii) The location at which the mean temperature reaches 1000 K [151], and iv) the height at which methane reaction rate goes over 1% of the maximum value evaluated at the specified time-step [152].

The experimental evaluations of the lift-off heights including fluctuations are 33 ± 7, 84 ± 11, and 135 ± 11 mm for Re = 7,000, 12,000, and 19,500, respectively. At Re = 7,000, as can be seen in Table 4.1, the differences in lift-off heights obtained by Dovizio et al. [8] and the current study are small (4.5 - 10 %), while differences start to be larger (9.6 - 16.5 %) for most of the criteria used at Re =12000, and become significant (27 - 30%) at the highest Re to be approximately 40 mm according to most of the criteria.
Comparing with the experimental results, the different lift-off height estimated values corresponding to each approach are plotted in Fig. 4.4. The predictions at the low Re for

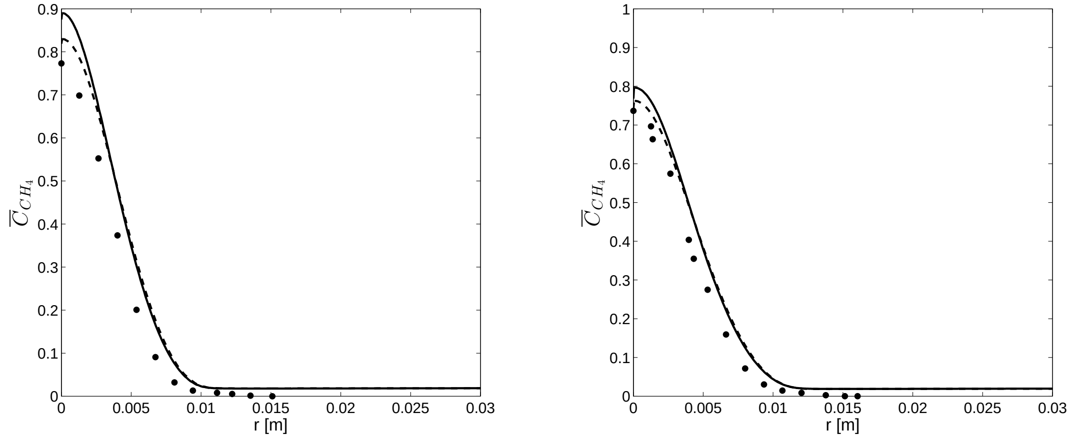

(a) x = 25 mm

(b) x = 30 mm

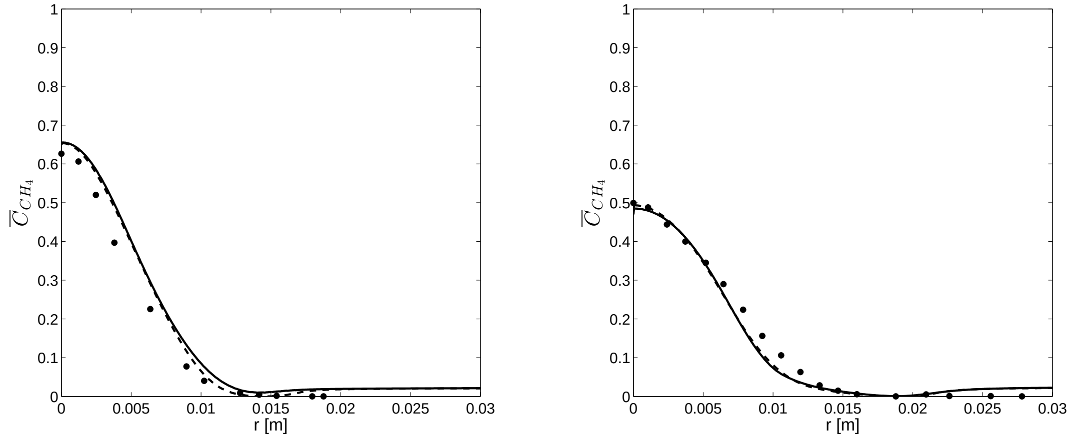

(c) x = 40 mm

(d) x = 60 mm

Figure 4.2: Radial methane concentration profiles obtained by RANS simulations at four axial locations, Re = 7000, where filled circles is Experimental [12], solid line current study, and dashed line Dovizio et al. [8].

all criteria are almost within the experimental lift-off height fluctuation limits, while for higher Re, discrepancies start to appear and increase with increasing Re values for most

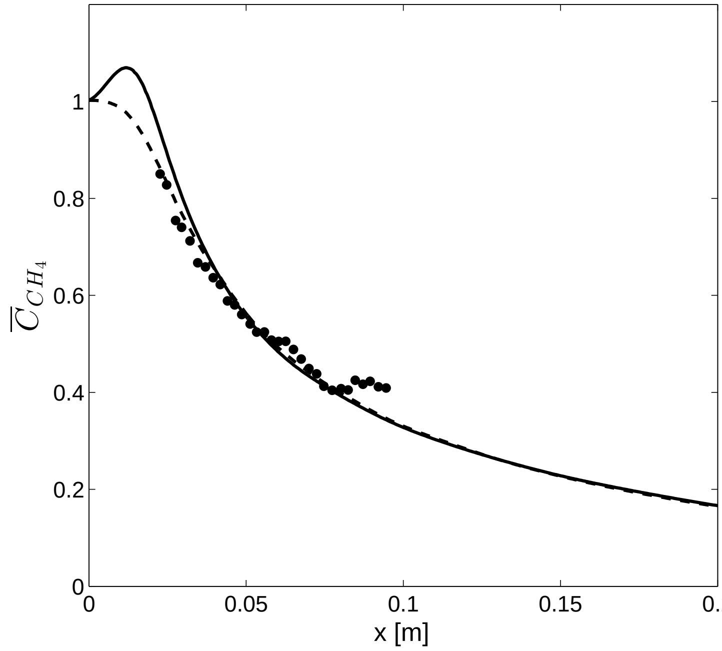

Figure 4.3: Axial methane concentration profile obtained by RANS simulations along the jet centerline, Re = 7000, where filled circles is Experimental [12], solid line current study, and dashed line Dovizio et al. [8]

Table 4.1: Lift-off heights in mm for different criteria obtained in the current study using Eq. (4.16) and the previous work of Dovizio et al.[8] using Eq. (4.11).

Criterion	**Re=7000**		**Re=12000**		**Re=19500**	
	Dovizio et al. [8]	**Current study**	**Dovizio et al. [8]**	**Current study**	**Dovizio et al. [8]**	**Current study**
$\widetilde{Y}_{OH} = 0.0004$	28.5	30.5	73	62	129	92
$\widetilde{Y}_{OH} = 0.0006$	29.5	31	74.5	64	129.5	92
$\widetilde{T} = 1000K$	34.5	38	83	75	137.5	100
1% of $\dot{\omega}_{CH_4}$	33.5	35	81.5	68	134	93

predictions.

Before implementing LSQR in the DCSE code, a stand-alone code of LSQR algorithm is used to compare the CPU time to solve the minimization problem presented in Eq. 3.15 for a given time and ensemble, with the time consumed for the same purpose using LU-decomposition. The same inputs are used for both techniques and the results are presented

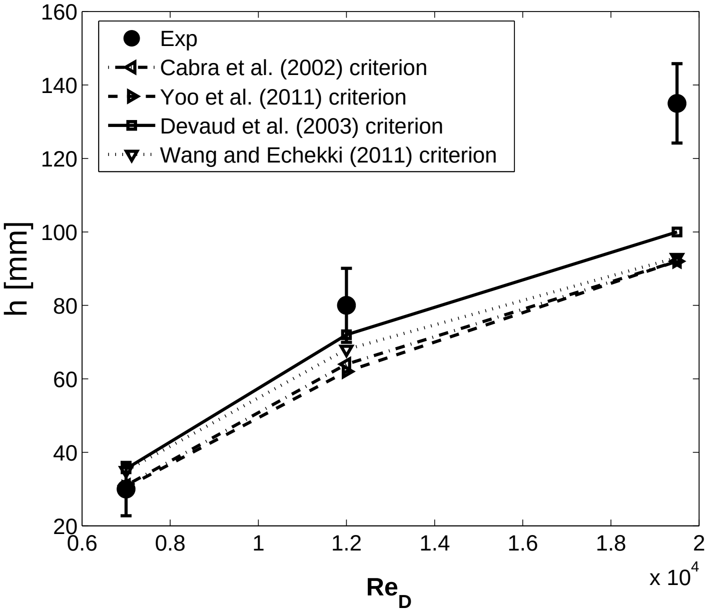

Figure 4.4: Predicted lift-off heights with different criteria compared with experimental data at three different Re. The bars indicate the rms of fluctuations of the mean lift-off height [13]

in Table 4.2. The results show a significant reduction in the time consumed in the inversion process using LSQR algorithm compared with the originally used LU-decomposition. The LSQR routine adjustable parameters like maximum number of iterations and relative error of results between each two successive iterations are set to 100 and 10^{-10}, respectively. It should be noted that the maximum number of iterations has never been reached for all tested time steps of the three ensembles. The value of $\|A\overrightarrow{\alpha} - \overrightarrow{b}\|_2$ is used as a measure of the deviation from exact solution. As the value of the given L2-norm decreases, the solution is closer to the exact solution. LSQR results show smaller L2-norm values compared to the values obtained using the LU-decomposition which means accuracy is improved. The results show that only very few bins have negative values, less than what LU-decomposition has. The non-physical values are replaced with zeros without affecting the results as they are found to appear on fuel rich mixture fractions where the reaction rates are negligible.

Next, the LSQR algorithm is coupled with DCSE. Two identical cases are run from the

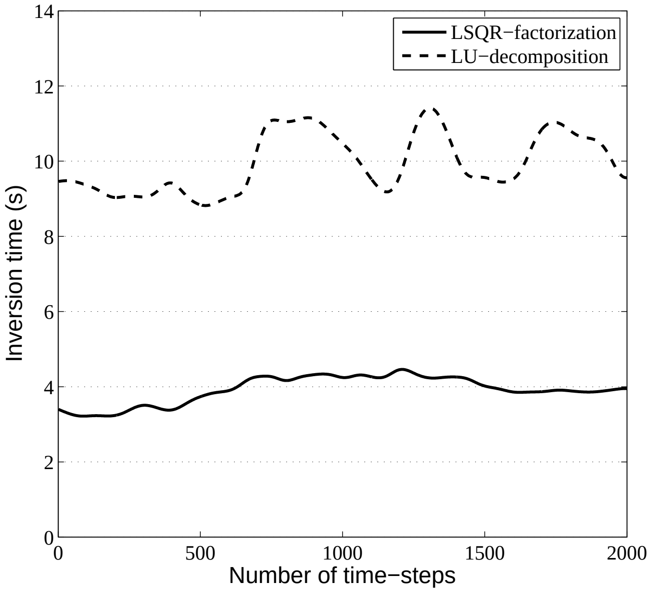

Figure 4.5: Time consumed in implementing the inversion process estimated at each time-step separately for cases using LSQR and LU-decomposition

Table 4.2: Comparison between results obtained in solving Eq. 3.14 using LSQR and LU-decomposition

Ensemble	**LU-decomposition**		**LSQR factorization**	
	L-2 norm	**CPU time (s)**	**L-2 norm**	**CPU time (s)**
1	0.1887	2.66	0.1703	1.17
2	0.3033	1.99	0.2231	1.27
3	0.1287	1.28	0.0487	0.66

same starting time and the same initial time step. As shown in Fig. 4.5, it is clear that the average time consumed per time-step, for LU-decomposition, is approximately 10 s, while it is approximately 4 s using LSQR leading to the computational time being reduced by 60%.

4.6 Summary

An initial RANS investigation is carried out to assess the effect of using LSQR and a more detailed progress variable SDR closure compared to what is used in the previous RANS simulations [8]. All the other model settings including the solver, governing equations, computational details and boundary conditions, used in the former investigation are employed in the current one to keep the comparison conditions. The results obtained for the first flame (Re=7000) show better predictions for the methane concentration field that reache 9.2% discrepancy with expreimental results. The predictions of the lift-off height show a significant impact of the progress variable SDR, even though they do not show good agreement with the experimental data. As the mathematical structure of the progress variable SDR model is more elaborate compared to the simple one used in [8], it is expected to show better performance within more detailed mixing field such as LES mixing field. Regarding LSQR, it has shown better performance with respect to the accuracy of the predicted conditional water mass fraction. In addition, it saves about 60% of the time consumed by LU-decomposition in DCSE calculation, considering that DCSE encounters much larger matrix/vector sizes compared to conventional CSE. These conclusions motivate the use of LSQR and the detailed SDR closure in LES investigations.

Chapter 5

LES-DCSE applied to turbulent lifted flames

A series of lifted turbulent flames were investigated in RANS using DCSE with a linear relaxation SDR model for the progress variable variance transport equation [8]. Some terms were also neglected in the progress variable transport equation (See section 4.1). The RANS predictions of the lift-off height were in good agreement within the experimental uncertainty [150] with a larger noticeable discrepancy for the second flame (Re=12000). Nevertheless, some flame statistics available in the experimental studies could not be used due to the averaging nature of RANS, such as the PDF of fuel concentration. It is also believed that LES will bring a much more realistic description of the turbulent flow and mixing fields of these complex flames.

The objective of the present study is to revisit the simulations of the lifted turbulent flames, previously undertaken in RANS-DCSE [8], but using LES-DCSE combined with a more elaborate SDR model and more accurate closure of the transport equation of the progress variable. There are additional challenges related to the implementation of DCSE in LES that will be discussed in Section 5.1. The experimental studies include three lifted turbulent jet flames with three different Reynolds numbers [12, 150, 13]. The predicted lift-off height and the flammability region width will be provided for the three flames under investigation and compared with available experimental data. Predictions for time-averaged methane concentration and its RMS, PDF, flame width, lift-off height and detailed qualitative observations are presented and compared with experimental observations, whenever possible. The present chapter is organized as follows: first, the Favre-filtered transport equations are presented. Next, the computational details are given including important aspects related to ensemble selection and chemistry tabulation. Finally, quantitative and qualitative analyses for the predictions are included, followed by a summary of the chapter.

5.1 Computational Details

5.1.1 Experimental Configuration

The same setup provided in Section 4.3 is used. In addition, information about turbulence scales and other experimental data is provided here. The integral length scale is estimated experimentally at the flame base to be 2.1, 5.6 and 9.45 mm for the Re = 7000, 12000 and 19500 flames, respectively [13]. The Kolmogorov scale is also given at the flame base for two flames: 0.2 mm for Re = 7000 and 0.7 mm for 19,500 [13]. In non-reacting conditions, the available data include axial and radial profiles of mean methane concentration and its rms, and jet width along the streamwise direction in the non-reacting case. Likewise, in the reacting cases, axial and radial profiles of mean methane concentration mean and its rms, methane concentration PDF at different locations, flammability regions and lift-off heights are given. The instantaneous planar images of methane concentration are obtained by collecting Raman-scattered light perpendicular to thin sheet of laser light passing through the axis of the flame.

5.1.2 LES domain

The computational domain is cylindrical using Cartesian coordinates in which x-direction is the streamwise direction while y- and z-directions are the cross-stream directions. The grid incorporates 400, 106 and 80 cells in the axial, radial and azimuthal directions, respectively. The spatial resolution is increased close to the nozzle and in the shear layer to capture the expected sharp scalar gradients. The resulting total number of cells is equal to 3,302,400 hexahedral cells for a length of 540 mm and radius of 189 mm. The spatial filter width, Δ, is defined as $(\Delta x \Delta y \Delta z)^{1/3}$ with Δx, Δy and Δz being the grid spacing in x, y and z, respectively, and is equal to 0.14 mm in the refined regions increasing to 9.5 mm at the domain sides towards the exit of the domain. In comparison to the turbulent length scales provided in the experimental studies, the filter width is located within the inertial sub-range in the refined mesh regions where combustion takes place.

The mesh size is selected after performing a rigorous sensitivity analysis including three meshes of 798,000, 3,302,400 and 7,965,000 cells. In particular, comparison was made for time-averaged methane concentration profiles in radial and axial direction and second order

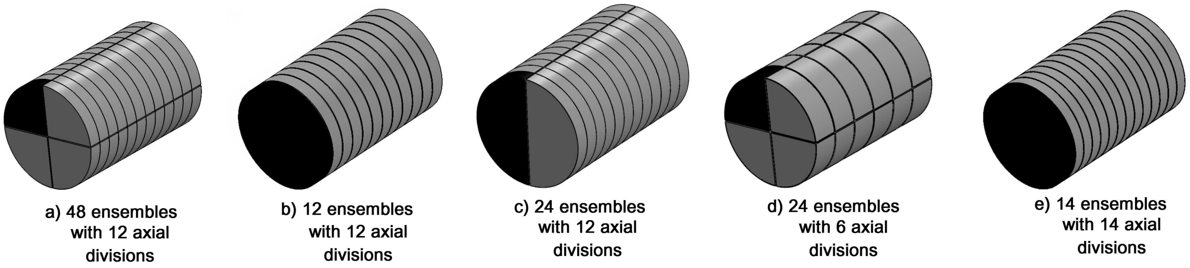
a) 48 ensembles with 12 axial divisions
b) 12 ensembles with 12 axial divisions
c) 24 ensembles with 12 axial divisions
d) 24 ensembles with 6 axial divisions
e) 14 ensembles with 14 axial divisions

Figure 5.1: Different ensemble patterns tested. For each configuration, one ensemble is illustrated by a darker area.

moments. As a result, the medium sized grid is selected. Further, the amount of resolved TKE is also examined. It is found that with the selected grid, between 85 and 95 % of the TKE is resolved in the jet area, and the region of shear layers.

5.1.3 Ensemble selection

The selection of ensembles is dictated by a trade-off between reducing computational load and keeping sufficient number of points in each ensemble. This aspect turns out to be more delicate in LES compared to RANS due to much larger computational cost and more crucial need of balanced load in parallel processing. It should be noted in the current LES-DCSE implementation, the domain decomposition for parallel processing follows the ensemble definition, i.e. one ensemble for each core. Further, in the present CFD code, the domain decomposition can only yield evenly distributed ensembles in space due to the current domain decomposition technique in OpenFOAM. Without this constraint, ensembles of uneven dimensions or ensembles made of non-adjacent regions could have been tested. In the future, it seems to be crucial to investigate ensemble definition and parallel processing together to yield variable and adaptive ensembles without any a-*priori* knowledge of the flame following some initial studies [126, 153].

A minimum requirement for the number of points in each ensemble is imposed by the matrix structure that is used in each inversion (matrix A in Eq. 3.15) and the current regularization technique, only applicable for over-determined system of equations. Thus, the minimum number of points in each ensemble is equal to $M + 1$, M being the product of the number of bins in mixture fraction and number of bins in progress variable space corresponding to 1,000 points. In the present case of turbulent flame simulations, this restriction becomes a minimum of 1,001 reacting cells. For example, if the entire computational domain is taken as one large ensemble, sufficient information is available to provide meaningful statistical information on the turbulent reacting field. However, the integral inversion would have to be performed using several million points using one processor/core leading to the loss of the benefits of parallel processing and extremely slow calculations, not feasible in the present LES. In contrast, if too many ensembles are defined, Eq. 3.14 may become rank-deficient (number of points below 1,000). Calculations will run much faster, but there is insufficient information on the reacting field to generate accurate inversions.

Using the observation that conditional averages have steeper spatial gradients in the streamwise direction [30], planes normal to the jet centerline form the basis of the ensemble configurations.

Different arrangements of ensemble are considered in the current simulations and shown in Fig. 5.1. Initially, a total of 48 ensembles are defined corresponding to cylindrical quarters, as presented in Fig. 5.1a). This distribution of ensembles yields the fastest runs, but also resulted in a significant issue related to the transient motion of the flame base. The simulated flames move up and down in the axial direction. If at one instant, the reacting zone leaves one ensemble, the number of reacting cells in this ensemble drops below 1,000 and no reaction is included. When the flame moves back down to this specific ensemble, in the present DCSE formulation, there is no reignition mechanism for an ensemble that was 'extinguished'. This problem points out a weakness of the CSE/DCSE model: convection in conditional space is not included. Thus, it is important to have ensembles sufficiently large around the flame base that can include the up and down motion of the flame in the axial direction. Further, at the beginning of the reacting flow calculations, it is important to set a large number of reacting cells in all ensembles. Combustion initialization takes place by setting the filtered mass fractions of CO_2 (or c) and H_2O to values close to their equilibrium values at the centre of the LES domain.

The current issue with 48 ensembles is specific to the current mesh and flames considered. For example, if a finer computational mesh was used, each of the 48 ensembles would include a larger number of points and contain more reacting cells, therefore in this case, 48 ensembles may be suitable for the simulation of the same flames. This means that the sensitivity analysis related to the ensemble selection needs to be repeated for each new computational mesh. The configuration with 12 ensembles is considered next, as shown in Fig. 5.1b). The resulting ensembles have the same axial length as those with 48 ensembles; however, there is no domain cutting in the radial and circumferential directions. In terms of correct physical description of the flame, this set of ensembles works well. However, the LES run time is significantly increased compared to the first calculations using 48 ensembles. Thus, as a compromise between 48 and 12 ensembles, the configuration with 24 ensembles is selected. The computational domain is divided into 12 ensembles in the axial direction, split into two in the centre. The present ensemble configuration, as shown in Fig. 5.1c) satisfies the numerical constraints on the minimum number of reacting cells in each ensemble and yields faster calculations related to the runs with 12 ensembles. It should be noted that the predicted lift-off heights were the same for 12 (Fig. 5.1b)) and 24 ensembles (Fig. 5.1c)).

The next two configurations, as can be seen in Fig. 5.1 d) and e), are tested to examine the impact of the axial distribution of the ensembles and therefore, the spatial variation of the conditional averages. Throughout the calculations, both configurations satisfactorily met the constraints on the minimum of reacting cells for the inversion to take place. For brevity, the results obtained for the first flame with Re = 7000 are discussed in the present section. However, the effect of the ensemble selection was also examined for the two remaining flames with similar conclusions. The impact on the predicted lift-off height was small, 30 mm for 12 ensembles (Fig. 5.1 b)), 33 mm for 6 ensembles in the axial direction (Fig. 5.1 d)) and 31 mm for 14 ensembles (Fig. 5.1 e)). Negligible changes in methane concentrations are also seen, 2% at most with the last three configurations tested. For the current flames, the largest number of axial divisions that could be applied is equal to 14. Associated with the selected number of ensembles is the computational cost. With 48 ensembles (Fig. 5.1a)), one time step requires 32 CPU seconds. In comparison, the completion of one time step with 12 ensembles (Fig. 5.1b)) needs 67 CPU seconds, 42 CPU seconds with 24 ensembles (Fig. 5.1c)), 44 CPU seconds with 24 ensembles using 6 axial divisions (Fig. 5.1d)) and 50 CPU seconds for 14 ensembles (Fig. 5.1e)) . This is a clear decrease in total computational time with increasing number of ensembles due to parallel processing and the fact of running one ensemble on one core/processor. Based on the considerations of the ensemble sensitivity study and computational cost, the domain decomposition of 24 ensembles, as shown in Fig. 5.1c), is selected for the present simulations for the three flames.With 24 cores (Intel Skylake 2.4 GHz processor) and using the selected mesh and ensembles, approximately 106 CPU hours are required to simulate one flow-through-time. One flow-through time is defined as the time needed by a fluid particle to travel over the entire length of the computational domain.

5.1.4 Favre-filtered transport equations

Transport equations of mass, momentum, enthalpy and species are solved. Seven species, CH_4, O_2, CO_2, H_2O, CO, OH and H_2, are determined by a transport equation each. These seven species are selected as being the main contributors of enthalpy changes. Further, transport equations for resolved mixture fraction, $\widetilde{Z}$, and its SGS variance, $\widetilde{Z''^2}$, are solved. The resolved mixture fraction, $\widetilde{Z}$, and its SGS variance, $\widetilde{Z''^2}$, have the following transport equations:

$$\frac{\partial(\overline{\rho}\widetilde{Z})}{\partial t} + \frac{\partial}{\partial x_i}(\overline{\rho}\widetilde{u}_i\widetilde{Z}) = \frac{\partial}{\partial x_i}\left(\overline{\rho}\,(D + D_t)\,\frac{\partial \widetilde{Z}}{\partial x_i}\right), \tag{5.1}$$

$$\frac{\partial(\overline{\rho}\widetilde{Z''^2})}{\partial t} + \frac{\partial}{\partial x_i}(\overline{\rho}\widetilde{u}_i\widetilde{Z''^2}) = \frac{\partial}{\partial x_i}\left(\overline{\rho}\,(D + D_t)\,\frac{\partial \widetilde{Z''^2}}{\partial x_i}\right) - 2\,\overline{\rho}\big(D + D_t\big)\frac{\partial \widetilde{Z}}{\partial x_i}\frac{\partial \widetilde{Z}}{\partial x_i} - \widetilde{\overline{\rho}\chi_z}. \tag{5.2}$$

Differential diffusion is neglected. The SGS scalar fluxes are modelled by a standard gradient assumption. The turbulent diffusion coefficient is calculated as $D_t = \nu_t/Sc_t$, where Sc_t is the turbulent Schmidt number. Three values of 0.4, 0.7 and 1, are tested for Sc_t for the simulation of the first flame (Re = 7000) and negligible effect is found on the numerical predictions of the axial and radial methane profiles and the lift-off height. This indicates that turbulent diffusion has a small impact on the predictions. This is likely due to the refined mesh selected. The calculated filter width is smaller than or equal to 0.4 mm upstream and around the flame base, gradually increased farther out in the radial direction and downstream. The experimental Kolmogorov scale is estimated to be equal to 0.2 mm at the flame base with a corresponding integral length of 2.1 mm [13]. In the present LES, the filter width is well within 2.1 mm for the vast majority of the flame. Due to the lack of significant changes when different values of Sc_t are selected, the value of 0.7 is kept. The SGS SDR for mixture fraction is modelled using a simple relaxation model given by,

$$\widetilde{\chi}_z = C_\chi\,\frac{\widetilde{\varepsilon}_{sgs}}{\widetilde{k}_{sgs}}\,\widetilde{Z''^2}, \tag{5.3}$$

where C_χ is a constant set to a value of 2, $\widetilde{\varepsilon}_{sgs}$ the SGS dissipation and $\widetilde{k}_{sgs}$ the SGS-TKE, both modelled and available in OpenFOAM [125].

In the present study, the progress variable, c is defined similar to the definition used in section 4.1 and for best comparison, it is useful to consider the same progress variable and same joint PDF model.

The Favre-filtered transport equation of c is given by

$$\frac{\partial(\overline{\rho}\;\widetilde{c})}{\partial t} + \frac{\partial}{\partial x_i}(\overline{\rho}\;\widetilde{u}_i\;\widetilde{c}) = \overline{\dot{\omega}_{tot}} + \frac{\partial}{\partial x_i}\left(\overline{\rho D\frac{\partial c}{\partial x_i}} - \overline{\rho}\widetilde{u_i''c''}\right), \tag{5.4}$$

The mean total progress variable source term is decomposed into

$$\overline{\dot{\omega}_{tot}} = \overline{\dot{\omega}_p} + \overline{\dot{\omega}_{np}} + \overline{\dot{\omega}_{cd}} + \overline{\dot{\omega}_c}, \tag{5.5}$$

where $\overline{\dot{\omega}_p}$ and $\overline{\dot{\omega}_{np}}$ are the premixed and non-premixed mode contribution terms, respectively, $\overline{\dot{\omega}_{cd}}$ the counter dissipation term, and $\overline{\dot{\omega}_c}$ the chemical source term of the progress variable. The first three terms in the right hand side of Eq. 5.5 are presented due to the dependence of the reaction progress variable on the mixture fraction. It is note-worthy to mention that Eq. 5.4 is valid when all molecular diffusivities are the same.

The first term, $\overline{\dot{\omega}_p}$, tends to zero because of the linear relation between c and Y_{CO_2}. The non-premixed mode contribution is negligible outside the flammability region, but it may be large close to stoichiometric conditions. Recently, this term was included in the LES calculations performed by Chen et al. [154] and the closure proposed by Ruan and co-workers [155] is applied in the present study given by

$$\overline{\dot{\omega}}_{np} = \overline{\rho \frac{1}{Y^{eq}_{CO_2}} \frac{\partial^2 Y_{CO_2}}{\partial Z^2} \chi_z} = \overline{\rho}\ \widetilde{c}\ \widetilde{\chi}_z \ \int_0^1 \frac{1}{Y^{eq}_{CO_2}(\eta)} \frac{\partial^2 Y_{CO_2}(\eta)}{\partial Z^2}\ \overline{P}(\eta)\ d\eta, \tag{5.6}$$

where $\widetilde{\chi}_z$ is the filtered scalar dissipation rate of mixture fraction being equal to the sum of the resolved and SGS components. The cross dissipation contribution term $\overline{\dot{\omega}}_{cd}$ is neglected in the current study. It is shown to be one order of magnitude less than the other two terms: $\overline{\dot{\omega}}_c$ and $\overline{\dot{\omega}}_{np}$ [143]. The governing equation of the SGS variance of reaction progress variable is written as

$$\begin{aligned} \frac{\partial(\overline{\rho}\widetilde{c''^2})}{\partial t} + \frac{\partial}{\partial x_i}(\overline{\rho}\ \widetilde{u}_i\ \widetilde{c''^2}) = -\frac{\partial}{\partial x_i}\left(\overline{\rho u_i'' c''^2}\right) + \frac{\partial}{\partial x_i}\left(\overline{\rho D \frac{\partial c''^2}{\partial x_i}}\right) - 2\ \overline{\rho}\ \widetilde{u_i''\ c''} \\ -2\ \widetilde{\chi}_c + \overline{2\ c''\dot{\omega}_c}\ . \end{aligned} \tag{5.7}$$

Equation 5.7 follows the derivation initially presented in RANS by Poinsot and Veynante [14], by subtracting the balance equation of $\tilde{c}^2$ from the balance equation of $\widetilde{c^2}$, but the present derivation is adapted to the LES context. Using the considerations outlined above for Eq. 5.4, one additional term appears, $\overline{2c''\dot{\omega}_{np}}$. The modeling of this term would require additional tabulation related to the conditional SDR of mixture fraction as this quantity is not directly available in DCSE. This is not straightforward. As a first approximation, $\overline{2c''\dot{\omega}_{np}}$ is neglected in Eq. 5.7. The gradient diffusion assumption is used for the SGS turbulent fluxes. The last term in Eq. 5.7 represents a correlation between the chemical source term and the fluctuations in the progress variable. This term can be determined using the following formulation

$$\overline{c''\dot{\omega}_c} = \int_0^1 \int_0^1 (c^* - \widetilde{c})\ \overline{\dot{\omega}_c|\eta, c^*}\ \overline{P}(c^*, \eta) dc^* d\eta, \tag{5.8}$$

where $\overline{\dot{\omega}_c|\eta, c^*}$ is obtained from DCSE and the TGLDM tables using

$$\overline{\dot{\omega}_c|\eta, c^*} = (\overline{\dot{\omega}_{CO_2}|\eta, c^*})/Y^{eq}_{CO_2}(\eta), \tag{5.9}$$

with $Y^{eq}_{CO_2}$ being the chemical equilibrium value of CO_2 mass fraction at a given mixture fraction, η. The other unclosed term, $\widetilde{\chi}_c$ is the SGS SDR which is further discussed in Section 5.1.5.

5.1.5 SGS progress variable SDR modeling

The SDR of the progress variable is a challenging term to close accurately and previous RANS-DCSE of stratified flames showed some sensitivity to the selected model [9]. Two expressions are implemented and tested in the current investigation. Recently, an expression based on the model of Kolla et al. [10] has been proposed for LES [156] and successfully implemented in LES-CMC of a turbulent premixed bluff-body close to blow-off [36]. In the present study, it is extended to partially-premixed combustion by having the model parameters functions of mixture fraction (or equivalence ratio).

$$\widetilde{\chi}_c(\widetilde{Z}) = \overline{\rho}\ (1 - exp(-\theta_5 \frac{\Delta}{\delta_L(\widetilde{Z})}))\ \Big[2K_c(\widetilde{Z})(\frac{S_L(\widetilde{Z})}{\delta_L(\widetilde{Z})}) + (C_3(\widetilde{Z}) \\ -\tau C_4(\widetilde{Z}) Da_\Delta)(\frac{2u'_\Delta}{3\Delta})\Big]\frac{\widetilde{c''^2}}{\beta_c}, \tag{5.10}$$

where θ_5 is a constant equal to 0.75, δ_L the unstrained laminar flame thermal thickness, K_c model parameter, S_L the unstrained laminar flame speed, C_3 and C_4 model parameters, τ heat release index, defined by $\tau(\widetilde{Z}) = \frac{T_b(\widetilde{Z})-T_u}{T_u}$ with T_b the adiabatic flame temperature and T_u unburnt gas temperature, Da_Δ the SGS Damköhler number, u'_Δ the SGS velocity and β_c model constant equal to 2.4. The SGS velocity is calculated as $u'_\Delta = (\frac{2}{3}k_{sgs})^{0.5}$. The Damköhler number is obtained by

$$Da_\Delta = \frac{\Delta\ S_L(\widetilde{Z})}{u'_\Delta \delta_L(\widetilde{Z})}. \tag{5.11}$$

To determine τ, K_c, S_L and δ_L, correlations based on experimental data are used and details can be found in the previous RANS-DCSE study of stratified flames [9]. The model coefficients C_3 and C_4 are calculated as functions of the SGS Karlovitz number, Ka_{sgs} with $Ka_{sgs} = ((u'_\Delta/S_L)^3/(\Delta/\delta_L))^{0.5}$ [36, 147],

$$C_3(\widetilde{Z}) = \frac{1.5\sqrt{Ka_{sgs}(\widetilde{Z})}}{1+\sqrt{Ka_{sgs}(\widetilde{Z})}}, \tag{5.12}$$

$$C_4(\widetilde{Z}) = 1.1(1 + Ka_{sgs}(\widetilde{Z}))^{-0.4}. \tag{5.13}$$

5.1.6 Chemistry details

For the current investigation, GRI-MECH 2.11 is the detailed mechanism used in the current study. The mixture fraction space is divided into 50 bins and the progress variable space into 20 bins. The mixture fraction bins are not uniformly distributed, with the bin density being higher around the stoichiometric value.

5.1.7 Boundary conditions

For the methane jet inlet, first non-reacting simulations are run using a synthetic turbulence generator, one-seventh power law velocity profile with fully developed flow conditions and extending the inlet pipe length to 115 mm. Then, these non-reacting values are set to the fuel inlet with a shorter extended inlet pipe of length 27 mm (five times the jet diameter). The pressure of the methane and coflow inlets is set to be calculated from zero gradient, while a non-reflective pressure boundary conditions are imposed at the outlet. The velocity at the outlet is calculated using zero gradient for an outflow, while the velocity is set to zero for reverse flow, if any. According to the experimental data, a small coflow velocity is set to represent the surrounding ambient air without affecting the lift-off height. Accordingly, a value of 0.01 m/s is used in the present calculations. The outer side of the computational domain has the same conditions used for the outlet. A temperature of 290 K is set for the methane jet and the air coflow.

5.1.8 SGS model and numerical schemes

A constant Smagorinsky model [16] is selected with a Smagorinsky constant (C_s) equal to 0.079. As will be discussed in Section 5.2.1, three other values of C_s are also tested for sensitivity analysis. The LES calculations of the present study are carried out by the open source CFD toolbox of OpenFOAM. The governing equations are solved with a finite volume low-Mach number pressure-based approach. The pressure is coupled with velocity by using PISO algorithm. A transient second order implicit Crank-Nicholson method is used to advance the transport equations in time with an adjustable time step for a maximum Courant number of 0.5. A NVD gamma scheme is used for the convective terms.

5.2 Results

In the present section, comparisons are undertaken between the measured experimental quantities and the predicted values both the cold and reacting methane jet.

5.2.1 Cold flow

As a first step, it is interesting to examine the turbulent flow/mixing fields without chemical reactions to identify any possible discrepancies with experimental observations. The non-reacting data is collected and time-averaged over 18 flow-through times. One of the key quantities on which the experimental analysis is based, is methane concentration, $C_{\mathrm{CH_4}}$. Figure 5.2 shows the radial profiles of the time-averaged methane concentration at four different axial locations compared with experimental data. Good agreement between the experimental data and the present LES predictions is obtained. For example, the predicted centreline values are within 8% of the experimental data at x = 25 mm, 6% at x = 30 and 40 mm and 14% at x=60 mm. Figure 5.3 presents the radial profiles of the rms methane concentration and the corresponding experimental data at three different axial locations. The resolved time-averaged rms is calculated by $\sqrt{< (\tilde{C}_{CH_4})^2 > - < \tilde{C}_{CH_4} >^2}$ where the brackets represent time averages and unresolved fluctuations are neglected. As displayed, the current LES overpredicts the rms values compared to the experimental values at all positions, while preserving the shape of the profiles. The predicted peak value is approximately twice as high as the corresponding experimental measurement. Further comparisons were undertaken with the results of three other Smagorinsky constant values, 0.01, 0.1 and 0.224 keeping the current mesh, and two other meshes, 798,000 and 7,965,000 cells with a Smagorinsky constant equal to 0.079. In all cases, the LES results significantly overpredict the experimental values. Negligible differences are found in the predictions when the C_s values of 0.01, 0.079 and 0.1 are used. For $C_s = 0.224$, the time-averaged methane concentrations and rms are further away from the experimental data compared to what is obtained with $C_s = 0.079$. Thus, the default C_s value of 0.079 is kept. A small improvement, at most 13%, could be seen with the finest mesh, but this improvement is hardly visible compared to the experimental values for a significant computational cost increase due to a mesh being more than twice as large as the selected grid. Further, these small differences in the predicted rms between the two finest meshes tested indicate that the discrepancies do not come from the magnitude of unresolved variance. Other sources of discrepancies in the simulations can be identified such as the turbulent inlet boundary conditions (normal stresses are specified) and the

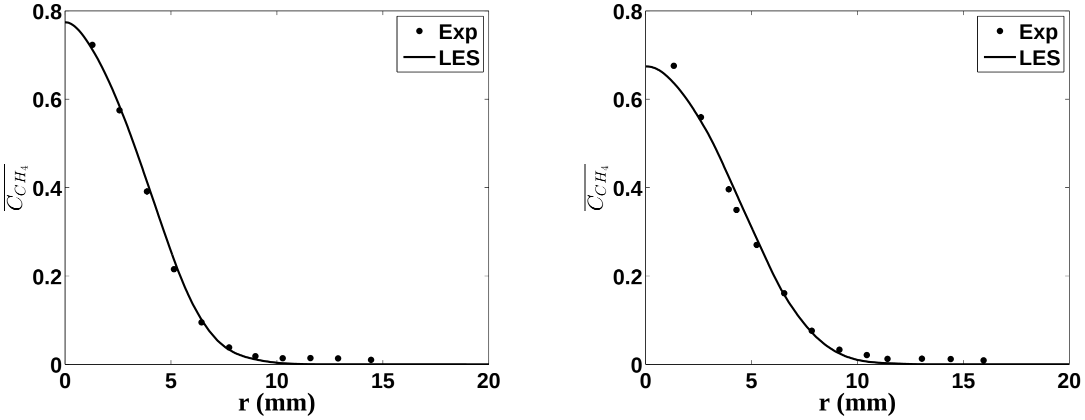

(a) x = 25 mm

(b) x= 30 mm

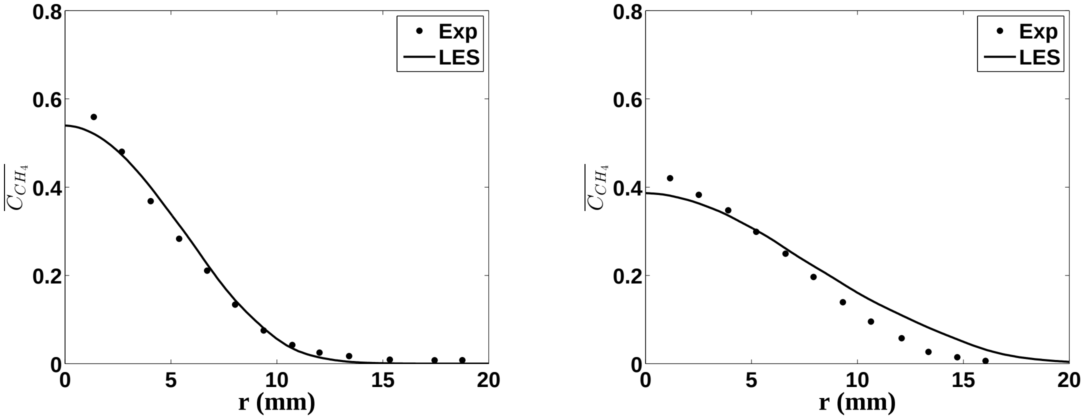

(c) x = 40 mm

(d) x = 60 mm

Figure 5.2: Non-reacting case: time-averaged methane concentration profiles at four axial locations, Re = 7000. Experimental values are taken from [12].

SGS model (constant Smagorinsky model). No additional measurements are available in the experimental studies for inlet Reynolds stress components [12, 150, 13]. A dynamic Smagorinsky model may improve the rms predictions. Without any documented experimental uncertainty [12, 150, 13], it is difficult to further assess the accuracy of the present results. However, different boundary conditions are tested for the current case (Re=7000). They include

1. Different values of coflow inlet velocity (0, 0.01 and 0.05 m/s). The differences in

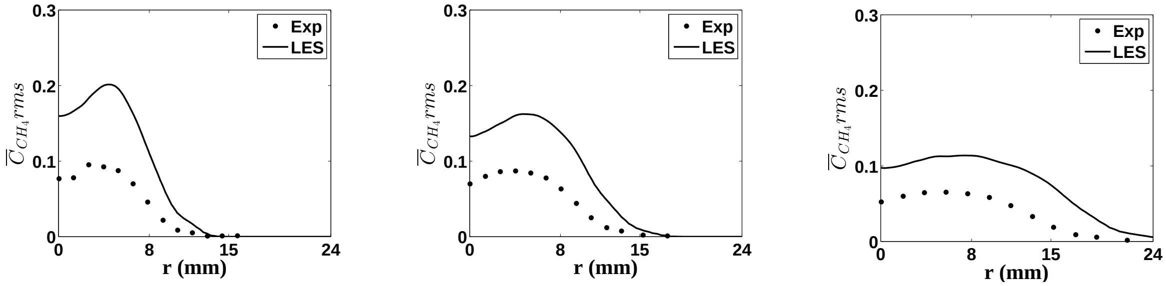

(a) x = 30 mm (b) x = 40 mm (c) x = 60 mm

Figure 5.3: Non-reacting case: methane concentration rms profiles at three axial locations, Re = 7000. Experimental values are extracted from [12].

predictions are found to be negligible.

2. For the main jet turbulence field, it is first assumed that there is no shear stress and only normal stresses are specified using ($v^{'} = w^{'} = 0.615u^{'}$) following [15] for fully-developed turbulent pipe flow. Also, different values of turbulence intensity I_t, which is defined as $\frac{u^{'}}{\widetilde{u}}$, are tested as shown in Fig. 5.4. Best results for filtered and resolved rms are obtained for ($I_t = 10\%$), but the differences in the predictions using the different values of turbulence intensity are small.

3. Then, an inlet pipe is added with length of 5d upstream of the fuel jet exit. There is no change in the predicted rms.

4. The final attempt is to run a simulation using an inlet pipe that covers more than the developing length of the methane jet (200d) [12]. Then, the radial profiles of all components of Reynolds stress tensor are obtained and mapped as an inputs for another case of inlet pipe of length 5d. However, the changes in the methane concentration rms predictions are negligible compared to the discrepancy with the experimental data.

5.2.2 Reacting flow

In the reacting conditions, data is collected and time averaged over 5 flow-through times. For the following numerical results, time averages are calculated directly from the Favre-filtered quantities. The experimental values do not appear to be mass-weighted and this may create some discrepancy between the current LES predictions and the experimental

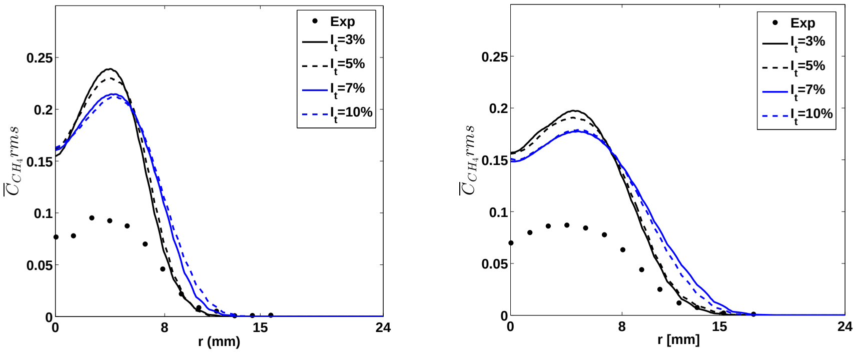

(a) x = 30 mm

(b) x = 40 mm

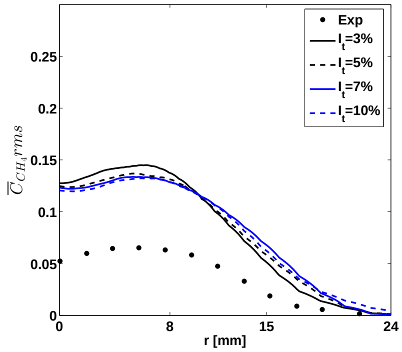

(c) x = 60 mm

Figure 5.4: Non-reacting case: methane concentration rms profiles with different values of turbulence intensity at three axial locations, Re = 7000. Experimental values are extracted from [12].

data. The time-averaged statistics and time-averaged density weighted statistics using Eq. 8 of [157] were also compared. The differences between the two sets of averages are found to be negligible for the radial and axial profiles considered in the present study. As shown in Fig. 5.5, the current LES-DCSE underpredicts the axial methane concentration profile along the centerline of the jet, in particular after 30 mm downstream of the jet exit. However, around the lift-off height (30 mm), the agreement between the numerical and experimental values is good with a relative difference of 17%. Downstream of the lift-off height, the larger predicted combustion rates are likely due to possible turbulent mixing field discrepancies on the centreline. In the previous RANS calculations of the same flames [8], closer agreement of the centreline values is obtained with the same chemistry tables.

It is believed that the differences between the two sets of simulation results are due to different types of turbulent flow and mixing field calculations, 2D RANS and 3D LES.

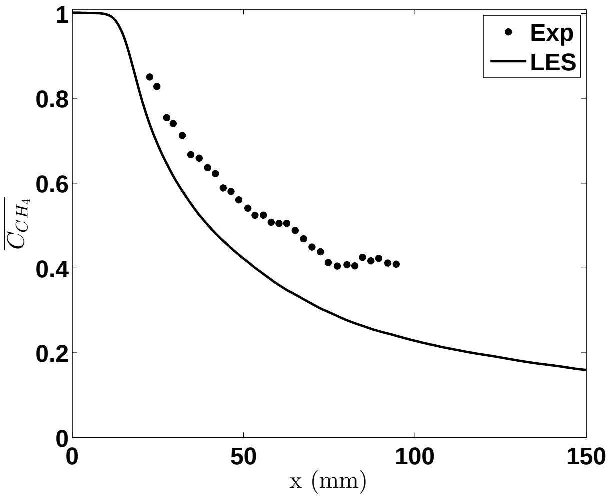

Figure 5.5: Reacting case: centreline profile of time-averaged methane concentration, Re = 7000. Experimental values are taken from [12].

The predictions of methane concentration radial profiles are shown with the corresponding experimental data in Fig. 5.6. Some discrepancies between the predictions and experimental data can be seen at the centreline, starting at 11% for x=25 mm increasing to 27% at x = 60 mm. However, the jet spreading rate is well predicted for axial locations smaller than or equal to 40 mm, which is around the predicted and experimental lift-off height value. Some experimental data are also given for the jet width which is estimated as the distance between the locations where the methane concentration drops to half the maximum value at the axial location. Similar to what is found in Fig. 5.6, the predicted jet width is in good agreement with the experimental value around the flame base, as shown in Fig. 5.7. The largest discrepancy between the numerical and experimental jet widths occurs at x = 60 mm with a value of 14%.

The PDF of the methane concentration is given in the experimental study [12]. The PDF is generated using 22,000 instantaneous values and the methane concentrations are normalized by their maximum value at the given axial locations. The PDF profiles obtained in the current LES and those from the experimental data are presented in Fig. 5.8. The shape and width are well reproduced; however a shift in the peak location can be seen, consistent with the underprediction of the peak value observed in the radial profiles, also visible in Fig. 5.5. The fact that the PDF width is well predicted brings some confidence

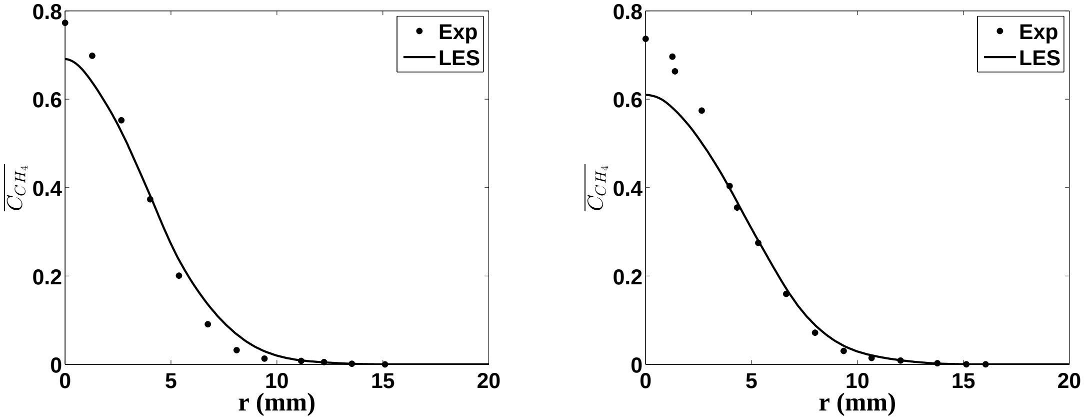

(a) x = 25 mm (b) x = 30 mm

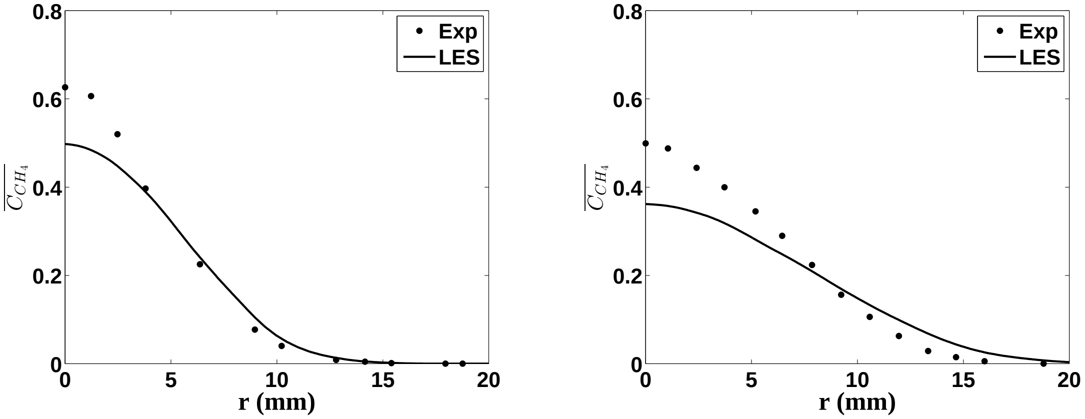

(c) x = 40 mm (d) x = 60 mm

Figure 5.6: Reacting case: time-averaged methane concentration profiles at four axial locations, Re = 7000. Experimental values are taken from [12].

in the current predictions of the fluctuation levels for the reacting case expected to be reasonable. In the current study, the flammability region is defined as the region included between two mixture fraction iso-surfaces of values 0.022 and 0.11, which are the lean and rich flammability limits of the methane-air mixture, respectively. The time-averaged width of the flammability region ($\overline{W}_f$) is evaluated at the flame stabilization location for

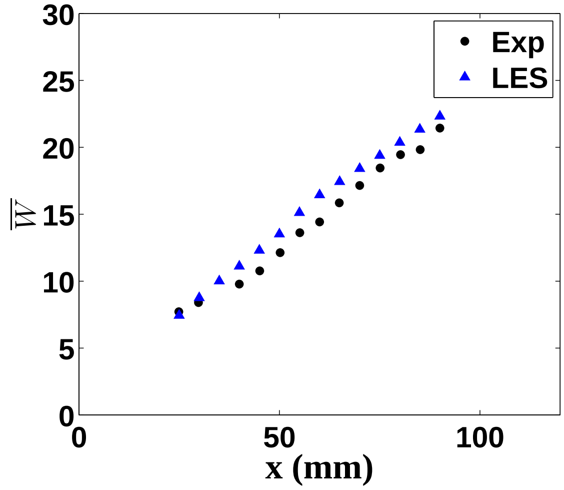

Figure 5.7: Time-averaged reacting jet width predictions with the experimental jet widths [12], Re = 7000.

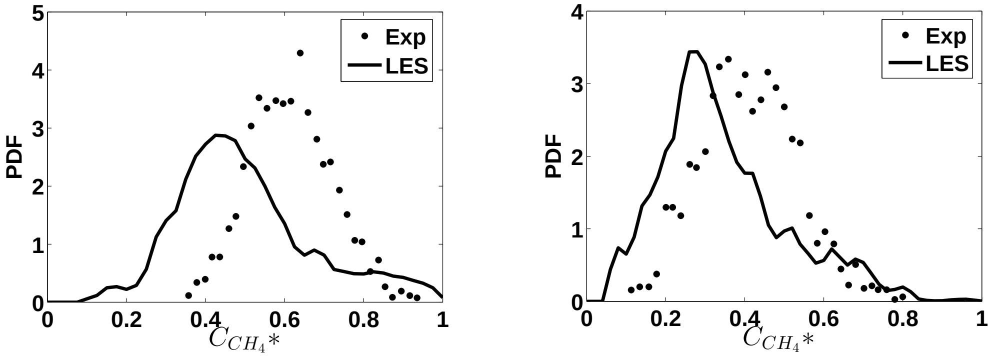

(a) centerline

(b) r=0.0043 m

Figure 5.8: PDF of normalized reacting methane concentration, 40 mm downstream of the fuel jet, Re = 7000. Experimental values are taken from [12]

the three flames by time averaging the instantaneous values that are collected from 95 instantaneous images equally distributed over one flow through time and using 4 planes. The LES predictions are shown to be within the experimental range, as shown in Fig. 5.9.

Although the lift-off height is the most distinctive characteristic of the turbulent lifted flames, there is no universal criterion to determine the lift-off height in experiments and simulations. Thus, many criteria can be found, including the use of temperature iso-

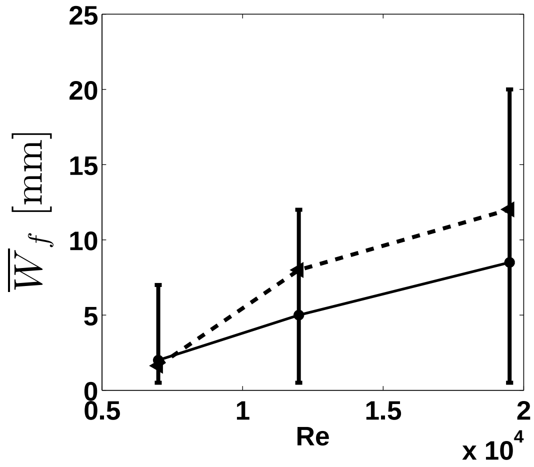

Figure 5.9: LES predictions (solid triangles) of flammability region width compared to the experimental values (solid circles) [13] at the flame base. The bar around the experimental data indicates the minimum and maximum values observed in the experiments.

contours of 900 K and 1000 K [151, 158] and OH mass fraction iso-contours of 0.0004 and 0.0006 [58, 60]. In addition, methane reaction rates and the reaction progress variable are used as markers for the flame leading edge [152, 159]. The previous RANS-DCSE investigations [8] have shown predictions for the lift-off height of the first flame ($Re = 7000$) with different criteria that have a maximum difference of 4.5 mm (15%), while the current LES investigation shows larger differences in the predicted lift-off height with a maximum of 6 mm (20%), probably due to the better description of mixing field in LES compared to RANS and the ability of LES to capture unsteady flame motions.

For consistency with the previous RANS-DCSE calculations for the same flames [8] and experiments, OH mass fraction ($\widetilde{Y}_{OH}$) equal to 0.0006 is used to estimate the flame base location. Table 5.1 shows the LES lift-off height estimations with the corresponding previous RANS predictions [8] and the discrepancies based on the jet diameter (d). Excellent agreement between the LES-DCSE results and experimental data is found for the three flames. As can be seen in Table 5.1, the current LES-DCSE has improved the lift-off height predictions compared to the previous RANS-DCSE results, in particular for the two flames with the largest Reynolds numbers due to better turbulent flow and mixing field description in LES. The flame base is also illustrated in Fig. 5.10 for the three Reynolds numbers.

Table 5.1: The lift-off height of the three investigated flames estimated by LES in the current study and RANS from a previous study [8] with the discrepancy obtained for both in terms of the methane jet diameter (d) relative to the experimental values.

Re	**Exp. (mm)**	**LES (mm)**	**LES discrepancy**	**RANS (mm)**	**RANS discrepancy**
7000	30 ± 7	30	0	29.5	0.09d
12000	80 ± 11	78	0.37d	74.5	1.02d
19500	135 ± 11	137	0.37d	129.5	1.02d

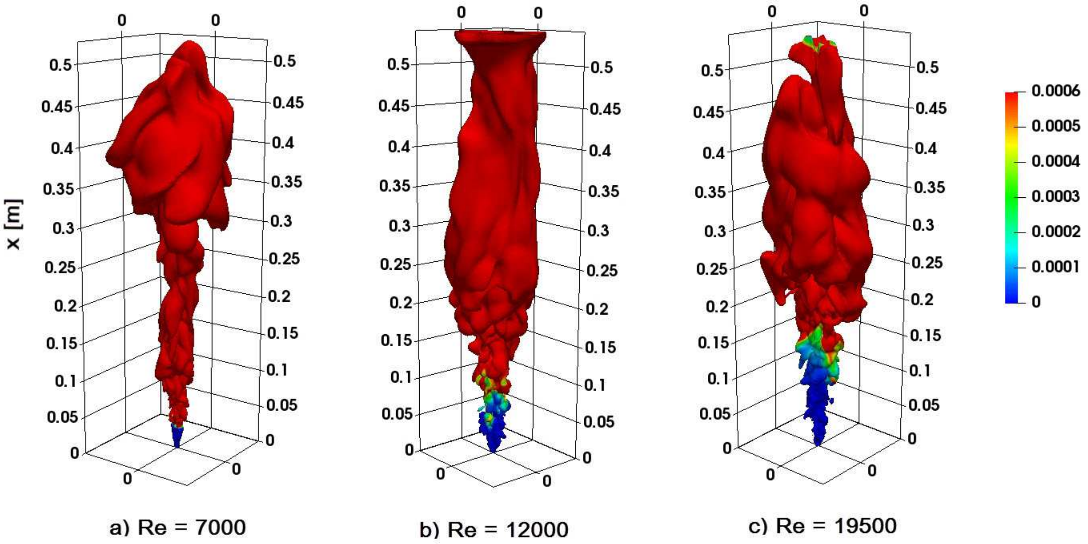

Figure 5.10: Instantaneous stoichiometric mixture fraction iso-surface colored by the instantaneous OH mass fraction field for the flames of a) Re = 7000, b) Re = 12000 and c) Re = 19500.

5.2.3 Qualitative analysis

Some additional comparisons can be made using reported experimental observations.

Methane Concentration

The available experimental observations are focused on the methane concentration distribution as it is a key quantity in the involved series of lifted flames experimental study [12, 150, 13]. Experimentally, the decay rate of methane is found to be higher in the non-reacting jet case compared to the lifted flame. This observation can be explained by the drop in the surrounding gases density as it is heated up by combustion resulting in less mass entrained towards the jet region. In the current investigation, two arbitrary values of methane mass fraction are selected ($\overline{Y}_{CH_4} = 0.1$ and 0.5) to show how far downstream these values can be found. Figure 5.11 shows that the traces of methane mass fraction equal to 0.5, for example, can be seen farther downstream of the jet compared to the non-reacting jet flow. This is noticed in a multiple instantaneous frames, but for brevity, only one time frame is used in Fig. 5.11 . It is also noticed that the shear layer area is wider in the non-reacting case due to higher air mass entrainment, which is consistent with the experimental observations. This is also visible in the time-averaged field of $\tilde{\mathrm{Y}}_{CH4}$, as shown in Fig. 5.12. The axial profile indicates a higher decay rate for methane mass fraction in the case of the non-reacting jet compared to the reacting case of the lifted flame.

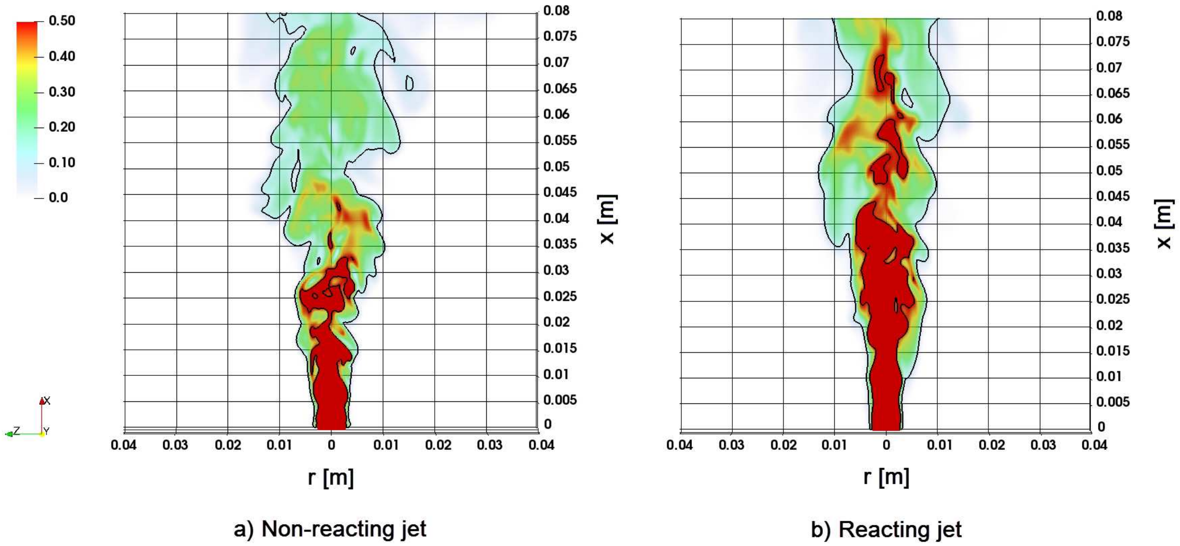

a) Non-reacting jet

b) Reacting jet

Figure 5.11: Instantaneous methane mass fraction contours to display the differences in methane mass fraction axial decay for a) non-reacting jet and b) reacting jet at $Re = 7000$. Methane mass fraction isolines of 0.5 and 0.1 (outer line) are also included in black.

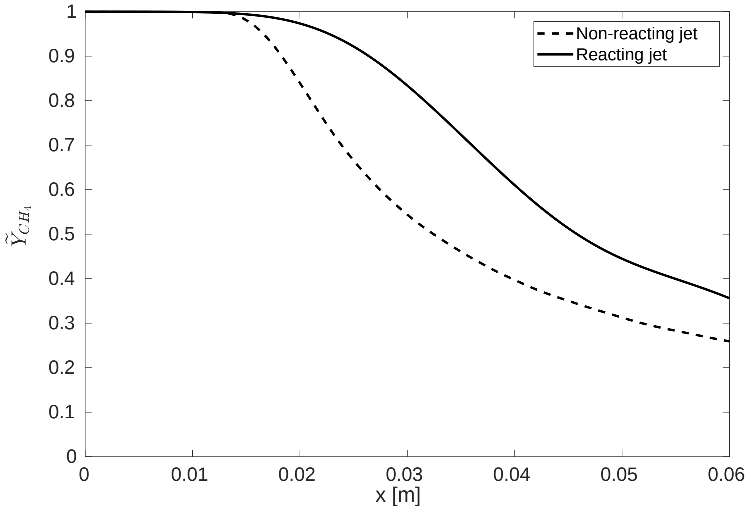

Figure 5.12: Time-averaged $\widetilde{Y}_{CH_4}$ axial profile along the centerline of the jet for non-reacting and reacting methane jet at $Re = 7000$.

Further detailed analysis [12] shows that the flame zone is established along the large scale fuel/air boundaries. It is also found that the flame zone follows the outer side of the normalized methane concentration isoline of 0.1. Different instantaneous frames of Heat Release Rate (HRR) per unit volume are presented in Fig. 5.13. The high HRR values are found on the outer side of the methane concentration contour of 0.1, in good agreement with the experimental observations [12]. The value of 0.1 is selected to match the analysis conducted in the experimental study [12]. It also corresponds to the stoichiometric value of methane concentration in non-reacting conditions.

Edge/Triple flame characteristics

The concept of the edge/triple flame has been proposed in several experimental and numerical studies to describe flames that involve fuel concentration gradients [160, 161, 162, 163, 164, 165]. This type of flame have several distinctive characteristics that involves mixture fraction and velocity fields. The situation of flame propagation through fuel concentration gradient forms three different fuel branches through the flame leading edge; a fuel-lean premixed flame branch, a fuel-rich premixed flame branch and the stoichiometric branch that passes close to the middle of the flame front. In the present investigation, the time-averaged OH reaction rates are found to have their highest values at the vicinity of the flame base. This is consistent with the experimental observations in which the highest

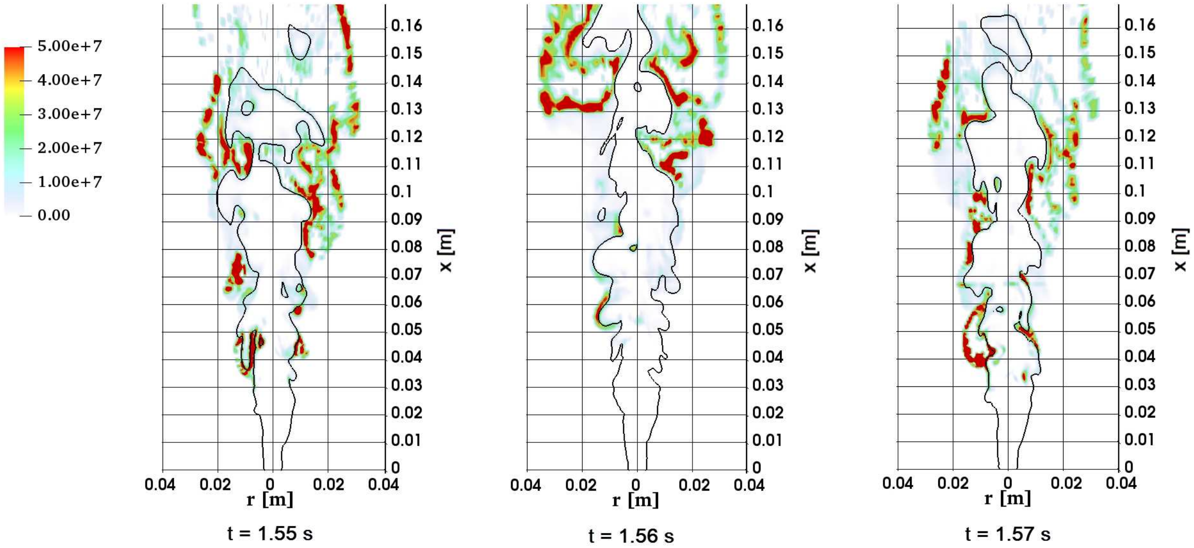

Figure 5.13: Instantaneous Heat Release Rate (HRR) frames (W/m^3) bounded by methane concentration isoline of 0.1 at $Re = 7000$.

OH concentrations are first found at the flame base area [13].

In Fig. 5.14, the stoichiometric branch goes through the middle of the flame base in the three flames, while the two flammability limit branches pass through the reaction zone which shows that reactions take place over lean and rich mixtures. Accordingly, this distinctive characteristic of the triple flame is well-reproduced in the present simulations with agreement with the experimental findings [163]. Figure 5.15 shows the time-averaged CO_2 reaction rate contours at the flame base of the lowest Re flame. The mixture fraction isolines show divergence upon the flame base which corresponds to the deceleration of the flow at the stabilization point. Consequently, this divergence is another indication of the triple point [165].

Effect of the SGS-SDR modeling

The SDR of the progress variable is found to have an impact on the flame predictions in some numerical RANS studies [9]. It is interesting to examine the effect of the SGS SDR further in the current LES-DCSE of turbulent lifted flames. Two reactive simulations of ($Re = 7000$) are implemented with two different SDR models for the progress variable,

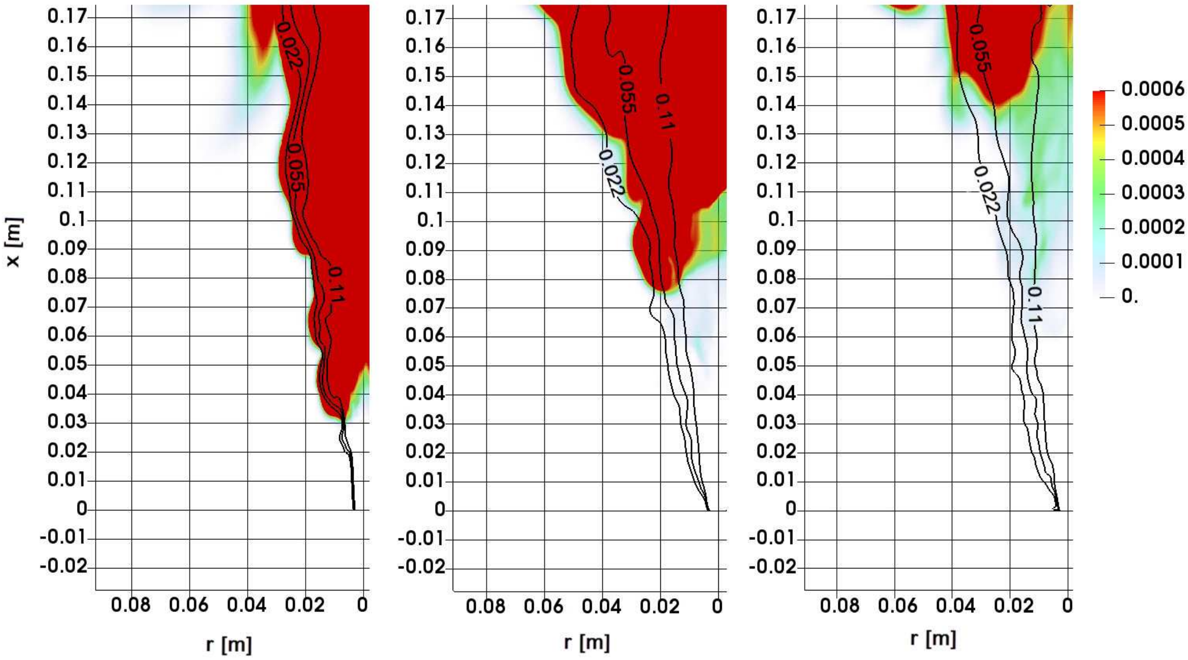

a) Re =7000 b) Re =12000 c) Re =19500

Figure 5.14: Stoichiometric mixture fraction isoline (0.055) with the flammability limit branches (0.022 and 0.11) going through the flame base superimposed on the filled contours of the time-averaged $\widetilde{Y}_{OH}$ at Re a)7000, b)12000 and c)19500. $\widetilde{Y}_{OH} = 0.0006$ is the lift-off criterion used in the current study.

using a simple linear relaxation model given by,

$$\widetilde{\chi}_c = \overline{\rho}\, \frac{\tilde{\varepsilon}_{sgs}}{\tilde{k}_{sgs}}\, \widetilde{c''^2}, \tag{5.14}$$

and the expression given in Eq. 5.10. For this investigation, three locations are considered: upstream the flame base (x = 25 mm), at the flame base (x = 30 mm) and downstream the flame base (x = 40 mm). Figure 5.16 shows the radial profiles of $\widetilde{\chi}_c$ and side by side those of three other quantities are included, rms of the SDR calculated by $\sqrt{< (\widetilde{\chi}_c)^2 > - < \widetilde{\chi}_c >^2}$ and time-averaged $\widetilde{Y}_{OH}$, $\tilde{c}$ and $\widetilde{T}$. The shape and magnitude of the two SDRs are visibly different for the 3 positions considered. The peak of the SDR modelled by Eq. 5.10 is always shifted to larger radial distances compared to what is seen in the profile given by Eq. 5.14. For the first two axial locations, 25 and 30mm, the relaxation model yields smaller peak values by a factor of 2 or more. It is also interesting to see the amount of

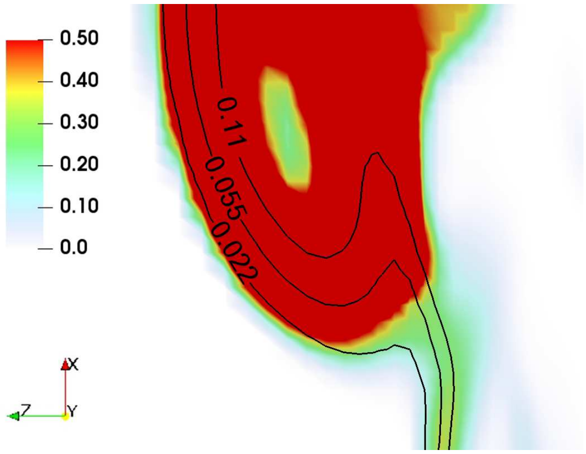

Figure 5.15: Stoichiometric mixture fraction isoline with the flammability limit branches (0.022 and 0.11) going through the flame base superimposed on the time-averaged OH reaction rates (1/s), at Re=7000.

fluctuations in each modeled SDR, the rms values exceed very often the time-averaged values. The lift-off height is determined by using $\widetilde{Y}_{OH} = 6 \times 10^{-4}$. As discussed in Section 5.2.2, the predicted lift-off height using Eq. 5.10 results in a value of 30 mm. This is visible in Fig. 5.16 for $\widetilde{Y}_{OH}$ radial profiles showing the peak of 6×10^{-4} at x = 30 mm. Farther downstream, at x = 40 mm, higher values are present, in particular two peaks of similar magnitude can be seen. In contrast, for the simulations using Eq. 5.14, there has been no significant OH produced yet at three selected axial locations showing no or little chemical reaction taking place. This also visible by the $\tilde{c}$ and $\widetilde{T}$ profiles in Fig. 5.16. Thus, the predicted lift-off height using Eq. 5.14 is much larger than 30 mm, being approximately 43% above the predicted lift-off height using Eq. 5.10. Similar trends are found when lift-off is determined by the temperature, instead of using $\widetilde{Y}_{OH}$ with the relaxation SDR model yielding lift-off heights approximately 32% larger than those including Eq. 5.10. In contrast, the lift-off height predictions are much closer to each other when the reaction rate of methane is considered for the determination of lift-off, within 10%. The current SDR model (Eq. 5.10) gives lift-off predictions closer to the experimental values. This is in agreement with previous studies indicating that the simple relaxation model is not accurate in the case of progress variable like in turbulent premixed combustion [166, 167].

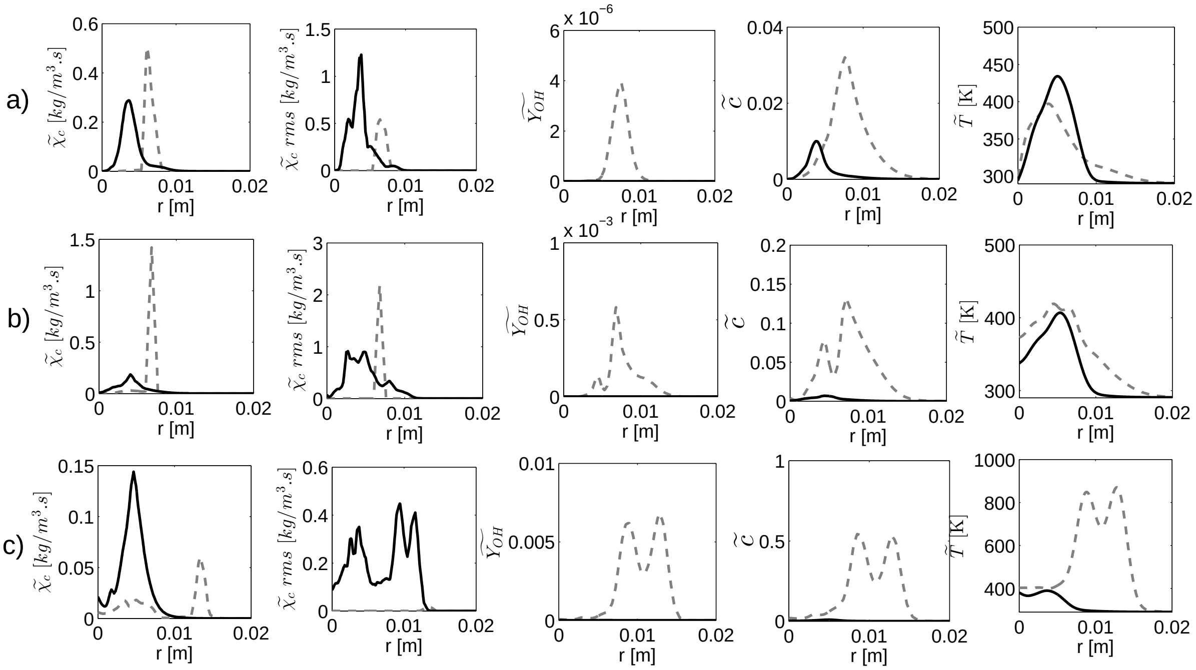

Figure 5.16: Radial profiles of time-averaged $\widetilde{\chi}_c$, rms of $\widetilde{\chi}_c$, OH mass fraction ($\widetilde{Y}_{OH}$), $\tilde{c}$ and temperature ($\widetilde{T}$) obtained using Eq. 5.14 (solid line) and Eq. 5.10 (dashed line) at three axial locations, a) x = 25 mm, b) x = 30 mm and c) x = 40 mm, for Re=7000.

The non-premixed mode contribution (NPMC) term effect

In the previous RANS-DCSE study [8], the NPMC term in Eq. 5.4, $\overline{\dot{\omega}}_{np}$, is neglected. In the current study, this term is included and modelled using Eq. 5.6. Its effect is investigated. First, it is found that this term has a negligible impact on the methane concentration profiles (not shown for brevity). For further analysis, Figure 5.17 displays the radial profiles of time-averaged $\widetilde{Y}_{OH}$, $\tilde{c}$ and $\widetilde{T}$ with and without the NPMC term. The OH mass fractions are clearly much smaller when the NPMC term is not included leading to delayed reaction and larger lift-off height. Without the NPMC term, the predicted lift-off height is equal to 35 mm, leading to an overprediction of 14% compared to the value when the NPMC is accounted for. Similar effect can be seen for the profiles of $\tilde{c}$ and $\widetilde{T}$. The inclusion of the NPMC term results in values of $\tilde{c}$ 2-3 times larger than those without NPMC. Similar effect for the predicted temperatures can be seen with a smaller impact at the first two axial locations, but at x = 40 mm, a significant difference is found: with the NPMC term the predicted temperature reaches 870 K, while without NPMC it barely gets to 424 K. Consequently, differences in the predicted lift-off height can be larger,

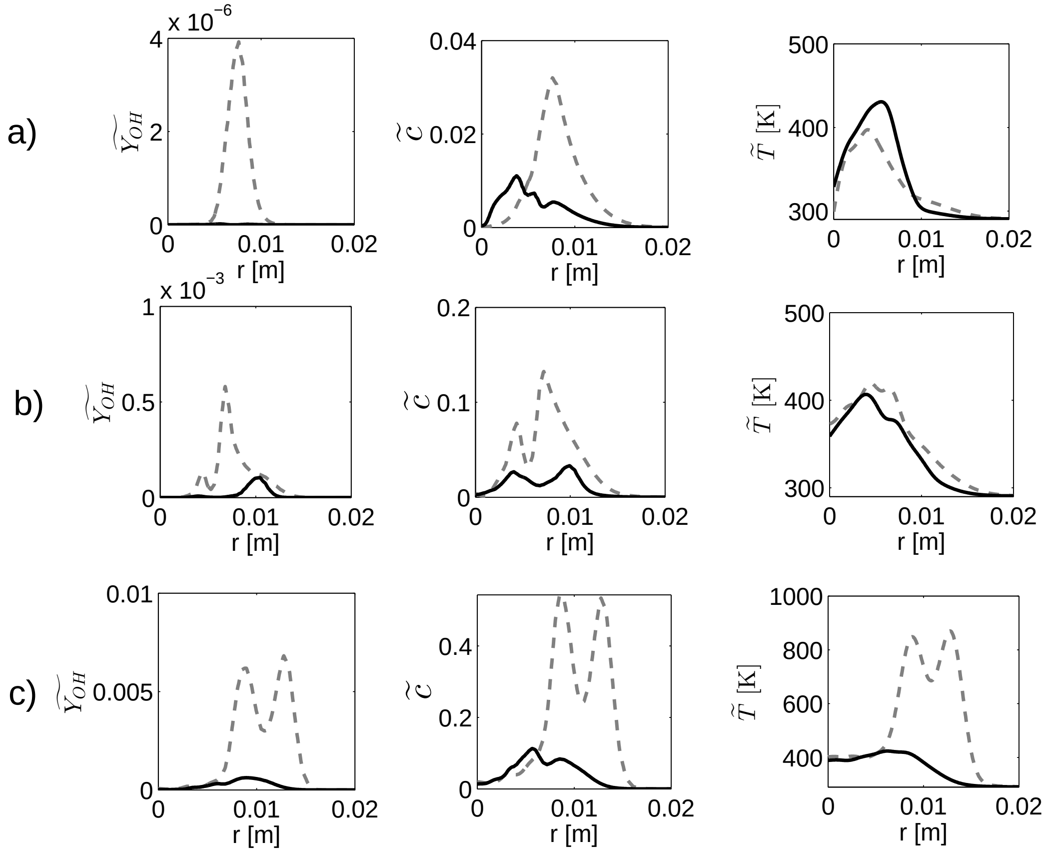

Figure 5.17: Radial profiles of time-averaged OH mass fraction for the same flame including the NPMC term (dashed line) and without the NPMC term (solid line), at three axial locations a)x = 25 mm, b)x = 30 mm and c)x = 40 mm, Re=7000.

in the order of 50% when temperature is used to define the lift-off height with negligible differences when the lift-off height is determined by the methane reaction rates.

5.3 Summary

For the first time, LES of a series of lifted turbulent jet flames in cold air (no autoignition is present) has been performed using DCSE for partially-premixed turbulent combustion. The two conditioning variables are mixture fraction to describe the non-premixed flame mode and a progress variable based on CO_2 to include the premixed flame propagation.

Predictions of mean and rms methane concentration are compared with available experimental data for the non-reacting methane jet at the lowest Reynolds number, Re = 7000. Good agreement is found for the mean, with larger discrepancies for the rms. Possible numerical inaccuracies may come from some uncertainties in the turbulent inlet conditions (no experimental measurements are reported at the nozzle exit) and the constant Smagorinsky model.

For the reacting conditions, time-averaged methane concentration profiles, jet width and methane concentration PDFs are compared with the experimental data available for the lowest Re flame. Reasonable agreement between the predictions and experimental data is found for the axial methane concentration. However, around the lift-off height the relative difference between the LES and experimental values is small, 17%. For the remaining variables, very good agreement between the present LES and experiments is observed. The methane concentration PDF profiles are well reproduced with a shift in the peak location, consistent with the small underprediction of the peak value in the methane concentration radial profiles. These good PDF predictions demonstrate that the predicted level of turbulent fluctuations in the present LES is reasonable in comparison to the experimental conditions.

For the three flames, flammability region width and lift-off height are determined and compared with experimental data. The predicted flammability region is within the experimental range of values for each flame. Excellent agreement with the experimental measurements is found for the lift-off height. The present LES-DCSE calculations also bring some improvement over what was obtained in previous RANS-DCSE [8] due to more accurate description of the turbulent flow/mixing fields and submodels for the closure of the progress variable transport equation.

Further qualitative analysis is conducted on a few other aspects of the flames. The predicted methane decay rate in the flame is found to be in agreement with the experimental observations. Some evidence of a triple/edge flame is noted, confirming the partially-premixed flame propagation. The progress variable SDR model is shown to have an impact on the lift-off height predictions. The simple relaxation model yields lift-off values that are 43% larger than those predicted by the modified expression of Dunstan et al. [156]. In agreement with previous studies [166, 167], the linear relaxation model does not appear to be sufficiently accurate for the present conditions. For the current simulations, the NPMC term included for the closure of the progress variable transport equation is shown to have a small impact on the predicted lift-off heights, but have a much larger effect on the progress variable and temperature field.

Chapter 6

LES-DCSE applied to a series of methane-piloted flames

A series of methane-piloted flames (D,E and F) with varying levels of local extinction are investigated in the present chapter. LES-DCSE is used to carry out the numerical simulations. The objective is to assess the ability of DCSE, as a partially premixed flame-based model, in predicting flames that have significant local extinction. The study investigates the effect of the number of bins in sample space, the PDF and the form of the progress variable with respect to the accuracy and computational cost. In this chapter, the computational details that include the experimental setup, the computational domain, chemistry tabulation and transport equations are introduced, followed by the boundary conditions and the numerical setup. Then, the results are discussed for Flame D, E and F.

6.1 Experimental configuration

The experimental configuration of the partially premixed Sandia flames (D-F) [76] consists of a main fuel jet of 7.2 mm diameter surrounded by a pilot of 18.2 mm outer diameter. The composition of the main jet is methane and air with volumetric percentage 25% and 75%, respectively. The stoichiometric mixture fraction is equal to 0.351. The average fuel jet speed is 49.6 (± 2), 74.4 (± 2) and 99.2 (± 2) m/s for flames D, E and F, respectively. The pilot is composed of ethyne, hydrogen, air, carbon dioxide and nitrogen with the same equilibrium composition and enthalpy as methane-air mixture of equivalence ratio 0.77. The average pilot velocity is 11.4 (± 0.5), 17.1 (± 0.75) and 22.8 (± 1) m/s for flames

D, E and F, respectively. An air coflow is provided by a wind tunnel at a speed of 0.9 m/s. No information is provided about the different flow length scales in the experimental papers, except for the macro length scale of the fluctuations in scalar dissipation which is measured as 1 mm [168]. The experiments provide detailed description for the velocity, Reynolds stress tensor components and TKE profiles of the inlets of main jet and pilot [77]. The experimental data provides radial profiles of Favre-averaged velocity, mixture fraction, temperature, and mass fractions of species CH_4, O_2, CO_2, H_2O, CO, H_2 and OH. In addition, conditionally-averaged temperature and species mass fraction radial profiles are available for comparison with numerical predictions.

6.2 LES domain

The computational domain is cylindrical with diameter of 381.6 mm (53 d) and length of 576 mm (80 d), where d is the main jet diameter. The domain is based on Cartesian coordinates where x-direction is the streamwise direction and y- and z- directions are cross-stream directions. The grid has 600, 114 and 80 cells in the axial, radial and azimuthal directions, respectively. The spatial resolution is higher close to the nozzle and in the shear layer between the main jet-pilot and the pilot-coflow. An inlet pipe of length 10 mm is provided to improve the main jet inlet conditions. The total number of cells for the computational mesh that is used in the current study is 5,300,000 hexahedral cells. A spatial filter width (Δ) which is $(\Delta x \ \Delta y \ \Delta z)^{\frac{1}{3}}$ is used implicitly in the solver, where Δx, Δy and Δz are the grid spacing in x, y and z, respectively. The filter width ranges from 0.14 mm to 7 mm where a range of (0.14 − 1 mm) is achieved from the centerline till radius of $4.4d$ in average. A sensitivity analysis is carried out on four grids of 840,000, 2,700,000, 5,300,000 and 6,700,000 cells. The analysis resulted in the selection of the third grid (5,300,000 cells). The analysis is made based on the first and second moments of the mixture fraction and velocity radial profiles. In addition, the resolved TKE is found to be higher than or equal to 90% of the total TKE on the flame region.

6.3 Favre-filtered transport equations

Transport equations of mass, momentum, enthalpy and species mass fractions are solved within the current solver. The species that are included are CH_4, O_2, CO_2, H_2O, CO, OH and H_2. To calculate the FDF that describes the statistical distribution of the mixture fraction, transport equations for resolved mixture fraction $\widetilde{Z}$ and its sub-grid scale (SGS) variance $\widetilde{Z''^2}$ are solved as presented in Eqs 5.1 and 5.2. The same assumptions used in Section 5.1.4 apply here, except for the turbulent Schmidt number which will be discussed later in Section 6.5. The progress variable is a parameter that quantifies the transition between unburnt and fully-burnt gases. Many definitions for the progress variable are covered in the premixed and partially premixed literature. It is usually a mass fraction of reactive species such as CO_2 [169, 170] or a summation of a number of reactive species such as CO_2, CO [171] and/or H_2O [172]. Further, it can be non-normalized or normalized by equilibrium value [171], maximum value [173], or complete combustion value [108] of the reactive species mass fraction which is a function of the mixture fraction. In the current study, two definitions of the progress variable are used to be assessed which is going to be discussed in detail in the next two subsections.

6.3.1 Normalized progress variable definition

The normalized form of the progress variable which is used in the current study, has been used successfully in LES-DCSE [174]. It follows the expression

$$c = \frac{Y_{\mathrm{CO_2}}}{Y^{eq}_{\mathrm{CO_2}}}, \tag{6.1}$$

where ${Y^{eq}}_{\mathrm{CO_2}}$ is the equilibrium value of $Y_{\mathrm{CO_2}}$ at specific mixture fraction, which is obtained from chemistry tables. According to Eq. 6.1, the value of c ranges from 0 at no reaction and 1 at fully burnt. Due to the dependence of c on mixture fraction, additional terms are expected in the Favre-filtered transport equation of c, as shown in Eq. 5.4. The transport SGS variance of the progress variable equation is also solved similar to Eq. 5.7. The assumptions and submodels used in Section 5.1.4 for some terms in the progress variable and its variance equations are employed here. Because there is no experimental data available for the relation between mixture fraction and laminar flame speed and thickness, unstrained laminar flame simulations corresponding to the composition of Sandia flames are carried out using Cantera 2.4.0. Then, the numerical data are curve-fitted to be used in the current LES investigation. To guarantee the quality of results obtained from the one-dimensional model of Cantera, the model is validated against the experimental data of the conventional methane-air composition [175, 176], that are used in Section (5.1.5) in the lifted flames investigations.

6.3.2 Non-normalized progress variable definition

As the normalized definition has the advantage of involving the non-premixed mode effect and extending the partially premixed characteristics to the presumed FDF by including the mixture fraction impact on the progress variable, it has the shortcoming of requiring closure the additional terms in Eqs 5.4 and 5.7. For these unclosed terms, few submodels are available or they are neglected due to high complexity. Therefore, a non-normalized definition is assessed in the current study using the mass fraction of carbon dioxide. Accordingly, the solution of Eq. 5.4 will not be needed as the transport equation of Favre-filtered mass fraction of CO_2 is already included in DCSE. As the coefficients of the modified laminar flame FDF are calculated based on the assumption that $(c = 1)$ is corresponding to equilibrium conditions, the non-normalized progress variable values are scaled by the equilibrium value to get the right statistical description.

6.4 Computational details

6.4.1 Chemistry technique

A detail chemistry mechanism is used in the current study which is GRI Mech 3.0 for methane-air combustion. Using the full set of species in DCSE will result in tremendously high computational cost, as discussed in Section 3.1, as it includes 77 species and 325 elementary reactions. To reduce the computational expenses and keep the effect of detailed chemistry, a technique should be employed to reduce the dimensions of the mechanism and tabulate the required chemistry data. Thus, TGLDM technique is kept in the current study to generate the chemistry tables for DCSE prior to the CFD simulations [116, 117]. The tables are generated in a similar way to that used for the methane-air lifted flames in Section 3.3. The difference in the reduction and tabulation process is in the mixture composition, which has a stoichiometric value of 0.351 instead of the conventional 0.055, and the distribution of mixture fraction points in the sample space. The bins of the mixture fraction sample space are distributed unevenly with most of which are located within the flammability limits. The equilibrium value of CO_2 does not show gradients with mixture fraction as sharp as those obtained for the typical methane-air composition. Eventually, the mass fractions and reaction rates of the major species CH_4, O_2, CO_2, H_2O, H_2, CO and OH are tabulated as a function of mixture fraction, mass fractions of CO_2 and H_2O.

6.4.2 Boundary conditions

For the main jet inlet and the pilot, the experimental data are used to provide the boundary conditions of velocity and turbulent kinetic energy. A synthetic turbulence generator is used with Reynolds stress tensor information provided experimentally. The pressure at the main jet and pilot is set to be zero gradient. At the outlet, the pressure is set to be non-reflective, the velocity is zero-gradient outward and zero inward. A coflow of 0.9 m/s of air is applied. A temperature of 294 and 291 K are used for the main jet and the air coflow, respectively, while 1880 K is used for the pilot.

6.4.3 SGS model and numerical schemes

A constant Smagorinsky model [16] is used with a constant C_s of 0.079. A sensitivity analysis for the Smagorisnky constant is applied on the values 0.047, 0.079 and 0.107 which led to the best results obtained at 0.079. The CFD simulations are carried out using a custom code based on a finite-volume low-Mach pressure based approach in the CFD package of OpenFOAM. The discretization of the governing equations includes a second order Crank-Nicholson scheme to advance the solution in time, and a normalized variable diagram (NVD) Gamma scheme for convective terms. Regarding the velocity-pressure coupling, the pressure implicit with splitting operators (PISO) is employed. An ajustable time-step setting is employed using a Courant number of value 0.4.

6.5 Results

The results that are presented in this section are time-averaged over 5 flow-through times at least. Further, the radial profiles are obtained by postprocessing the LES to average the radial profiles over space at any specific plane.

6.5.1 Flame D

Flame D is considered the most stable flame among the three flames investigated in this work with little local extinction. However, its investigation as a partially premixed flame motivates a number of analyses. Therefore, some comparisons are carried out using flame D predictions with the experimental data to find the model setting that gets predictions in best agreement with the experiments. The current comparison is carried out on the radial profiles of Favre-averaged quantities at axial locations of $3d$, $7.5d$ and $15d$. The comparison is applied to investigate the difference between predictions obtained for

- 20 and 50 bins progress variable sample space both are modelled using modified laminar flame FDF
- progress variable statistical distribution described by modified laminar flame FDF and another by β-FDF
- normalized and non-normalized progress variable form

Ensemble sensitivity analysis

As the number of ensembles increases, the computational time decreases due to the fact that each ensemble is processed by a single core in the parallel processing of the simulations. However, a numerical restriction should be satisfied which requires a minimum number of reacting cells in each ensemble that is equal to (M) to avoid rank-deficiency in Eq. 3.14. To carry out a sensitivity analysis for the ensemble configuration selection, the smallest ensemble size should obtain more or equal to M reacting cells. Compared to lifted flames [174], the ensemble selection is considered simpler for attached flames as it does not encounter flame base motion. The only precaution that should be taken into account is monitoring the number of reacting cells in each ensemble (the small ones) to make sure that the local flame extinction (property of the current flames) does not lead to a global numerical extinction in the entire ensemble.

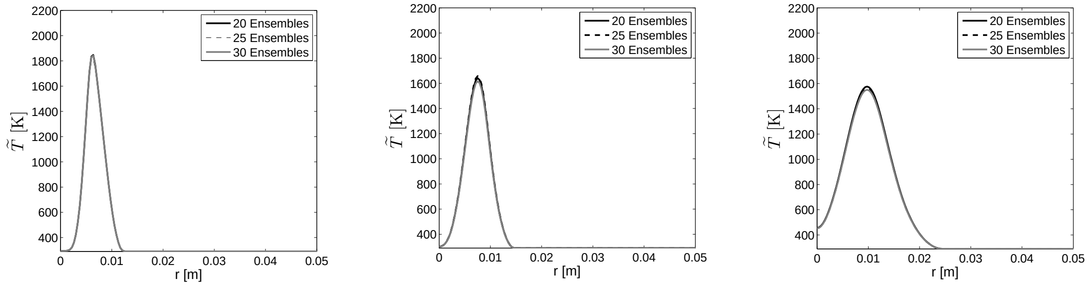

(a) x= 3d (b) x= 7.5d (c) x= 15d

Figure 6.1: Radial profiles of Favre-filtered temperature at three axial locations of Flame D corresponding to three ensemble configurations.

In the current investigation, three different numbers of ensembles are examined to make sure that the number of ensembles that is used for getting final results has no effect on the simulations. The three configurations are introduced as axial divisions of the computational domain separated by planes normal to the streamwise axis. The number of ensembles tested are 20, 25 and 30 ensembles. The temperature radial Favre-filtered profiles, shown in Fig. 6.1, demonstrate a negligible effect for the number of ensembles that ranges between (1.6 - 1.8 %) relative to the results obtained for 30 ensembles. This is in agreement with Bushe's analysis [107] for Sandia flames, which points out that doubly conditional averages do not vary significantly in space. Accordingly, the number of ensembles that are selected for the final simulations is 30.

Turbulent Schmidt number selection

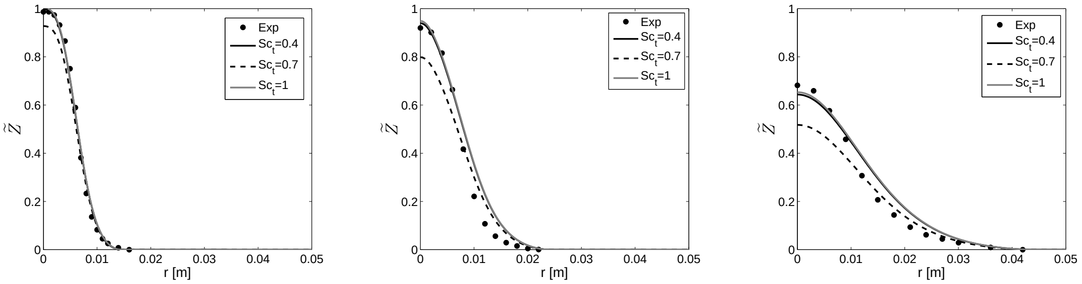

(a) x= 7.5d (b) x= 15d (c) x= 30d

Figure 6.2: Radial profiles of Favre-filtered mixture fraction at three axial locations of Flame D corresponding to simulations carried out using three different turbulent Schmidt number values.

In turbulent reactive flows, turbulent Schmidt number Sc_t plays a crucial role in the turbulent transport of species, mixture fraction, progress variable and, consequently, temperature. This makes the selection of appropriate value of Sc_t is very important to have the best description of the mixing field. Further, the effect of Sc_t varies with the case study, the computational domain and the type of turbulence modelling. Therefore, three different values of Sc_t are examined, which are 0.4, 0.7 and 1. Figure 6.2 shows the impact of Sc_t on the Favre-filtered radial profiles of mixture fraction at three axial locations. The predictions obtained by $Sc_t = 0.4$ and 1 are very close with negligible differences, while the predictions obtained by $Sc_t = 0.7$ shows a discrepancy that ranges from 5.9% at $x = 7.5d$ to 24.1% at $x = 30d$. This indicates overpredicted decaying rate for $Sc_t = 0.7$. Therefore, a turbulent Schmidt number of value 0.4 is selected for the current simulations following the present observation and in agreement with previous study [96].

Progress variable sample space resolution

The resolution of the progress variable and the mixture fraction sample spaces needs to be examined, and its effect varies from case to case and it can be different in RANS and LES for the same case. The quality of the predictions is expected to increase by refining the sample space, although beyond a certain limit, the refinement does not add much. The shortcoming of the refinement is the significant increase in the computational load, as the time consumed in the single time-step is 73.3 s and 168.5 s for 20 and 50 bins, respectively. Therefore, Flame D is simulated using 20 and 50 bins in the progress variable sample space. Figures (6.3 - 6.5) show a comparison between the Favre-filtered radial profiles obtained by DCSE simulations using 20 bins and 50 bins in the progress variable sample space with the experimental data. At $x = 3d$, the (50 bins) predictions of axial velocity show 4% discrepancy at the centerline, while (20 bins) predictions has maximum discrepancy 8% at $r = 0.3d$. Both predictions show good agreement at $x = 7.5d$ except at the centerline where the discrepancy is 2.6% and 5.9% for 50 bins and 20 bins, respectively. At $x = 15d$, a general overprediction is obtained between $(0.7d \leq r \leq 2.1d)$ for both simulations, while a large discrepancy is obtained for (20 bins) at the centerline (24%) and less deviation from experiments is obtained for 50 bins (6.7%). By inspecting the Favre-filtered mixture fraction profiles, the results using 50 bins are in very good agreement with experimental data at $x = 3d$ and $7.5d$ with maximum discrepancy of (0.1) at $r = 1.7d$. In contrast, those with 20 bins do not show good agreement, especially at $x = 15d$. The discrepancies range from 11.5% to 19.3% mostly in the region of $(0 \leq r \leq 0.8d)$.

This can be linked to the discrepancies in the temperature profiles prediction as the density and viscosity are directly affected by temperature. This can be observed from Fig. 6.3, as the temperature discrepancy obtained for 50 bins ranges from 4.3% to 13.7%, where the overprediction in the main species mass fractions (CO_2 and H_2O) is expected at the same region, as found in Fig. 6.4. As expected from mixture fraction predictions, the temperature profiles with 20 bins exhibit high discrepancies that range between (17.6%-25.4%) where the peak temperature location is shifted farther outward and the reaction region width shows significant overprediction at $x = 7.5d$ and $15d$.

The major species mass fractions (CO_2, H_2O and CH_4) radial profiles show consistent prediction with the temperature profiles with good agreement for 50 bins and significant discrepancies for 20 bins. The same can be concluded for the minor species profiles presented in Fig. 6.5. Accordingly, 20 bins are not sufficient to provide reasonable description of flame D, although it saves a considerable amount of computational cost. 50 bins have provided good agreement in general with experimental data at the cost of more computational load (higher by a factor of 2.3).

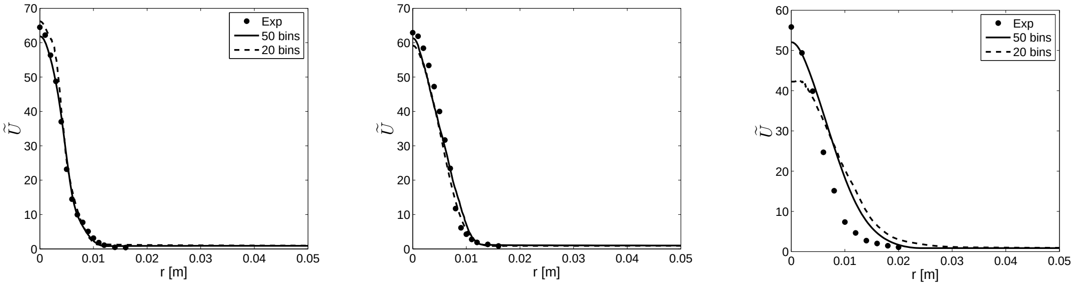

(a) x= 3d (b) x= 7.5d (c) x= 15d

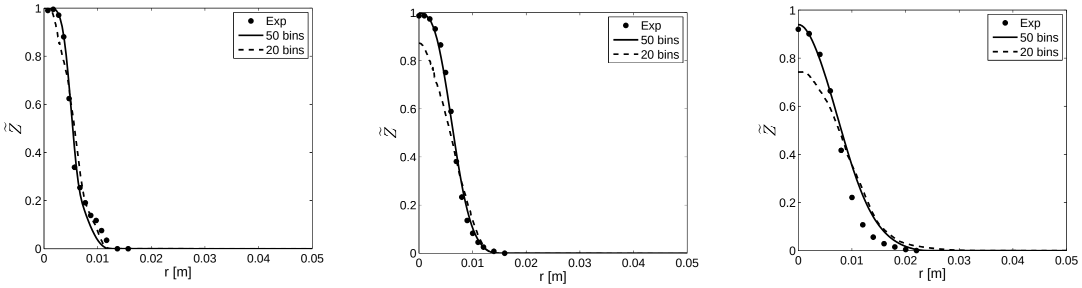

(d) x= 3d (e) x= 7.5d (f) x= 15d

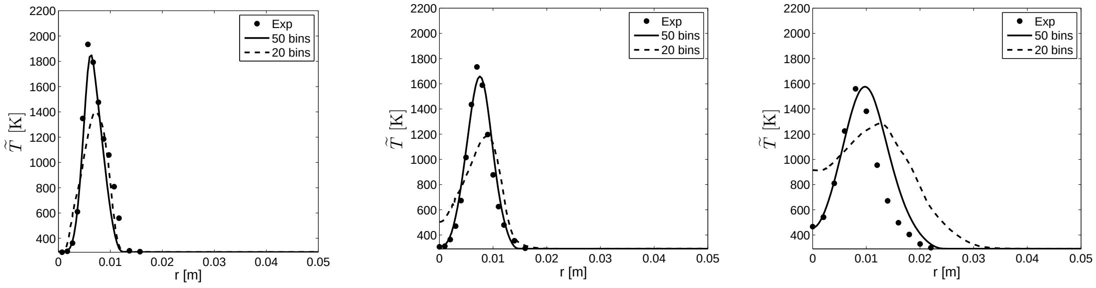

(g) x= 3d (h) x= 7.5d (i) x= 15d

Figure 6.3: Radial profiles of Favre-filtered mass fraction of velocity, mixture fraction and temperature at three axial locations of Flame D corresponding to simulations carried out using 20 bins and 50 bins in the progress variable sample space, compared to the experimental data [77, 76].

Progress variable statistical distribution

Although previous investigations in premixed combustion did not recommend employing β-PDF to describe the statistical distribution of the progress variable [110], it is worth

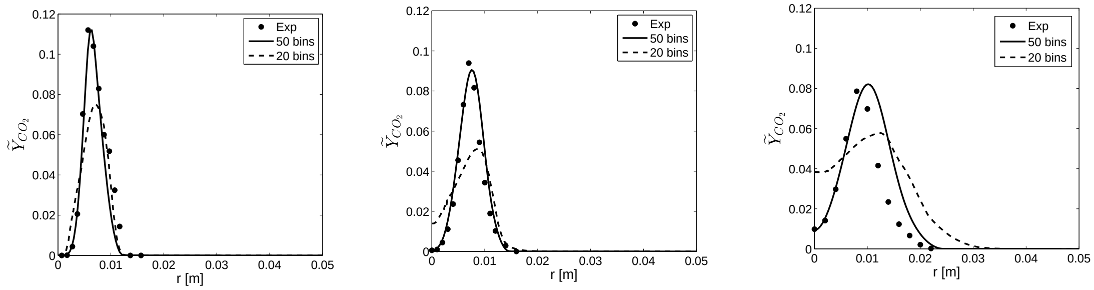

(a) x= 3d (b) x= 7.5d (c) x= 15d

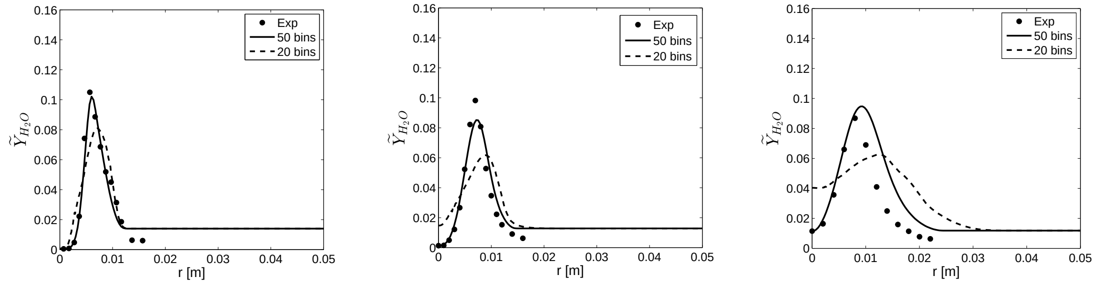

(d) x= 3d (e) x= 7.5d (f) x= 15d

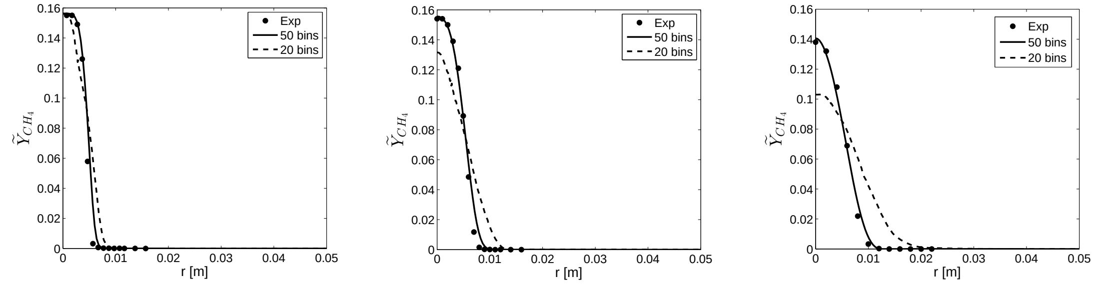

(g) x= 3d (h) x= 7.5d (i) x= 15d

Figure 6.4: Radial profiles of Favre-filtered mass fraction of major species (CO_2, H_2O and CH_4) at three axial locations of Flame D corresponding to simulations carried out using 20 bins and 50 bins in the progress variable sample space, compared to the experimental data [76].

investigating the performance of β-PDF with the progress variable in LES-DCSE in comparison with the modified laminar flame PDF, due to the significant reduction in computational time (43% of the time consumed by MLF-PDF). The velocity profiles show a general overprediction at the three locations with discrepancy between 5.8 and 10% at $x = 3d$ and

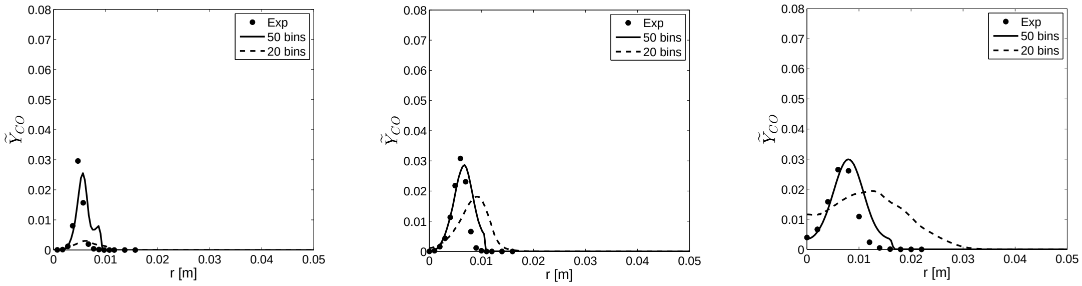

(a) x= 3d (b) x= 7.5d (c) x= 15d

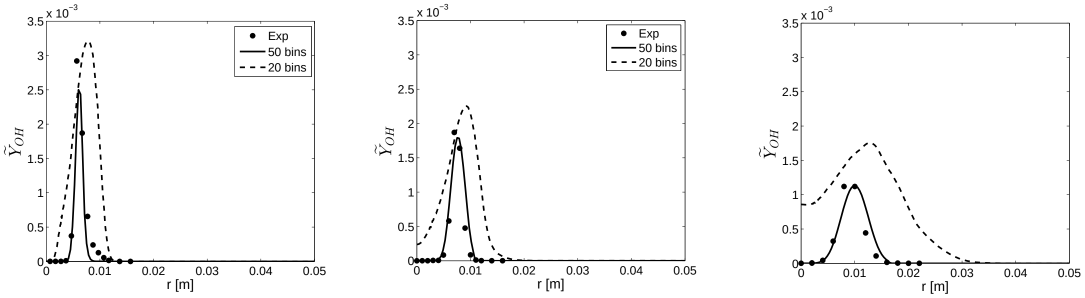

(d) x= 3d (e) x= 7.5d (f) x= 15d

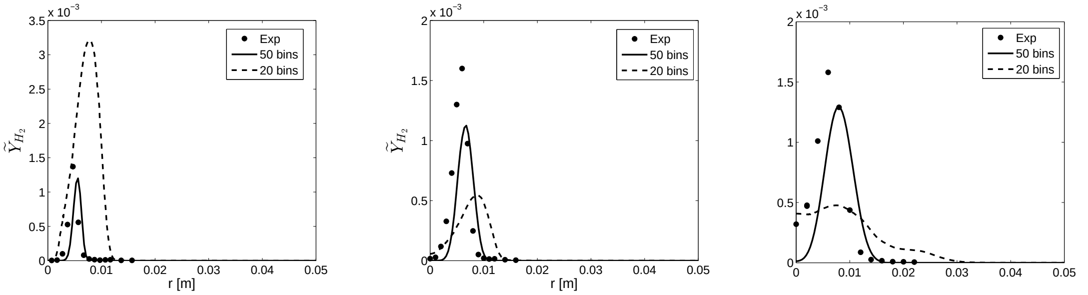

(g) x= 3d (h) x= 7.5d (i) x= 15d

Figure 6.5: Radial profiles of Favre-filtered mass fraction of minor species (CO, OH and H_2) at three axial locations of Flame D corresponding to simulations carried out using 20 bins and 50 bins in the progress variable sample space, compared to the experimental data [76].

$7.5d$, while large discrepancies that tend to (16.27 m/s) at $x = 15d$ within the vicinity of $r = 1.7d$. However, the β-PDF results in a better centerline prediction compared to the modified laminar flame (MLF-PDF). As for the mixture fraction profiles, the β-PDF yields better agreement with experimental data in the region of ($1.07d \leq r \leq 1.9d$) at

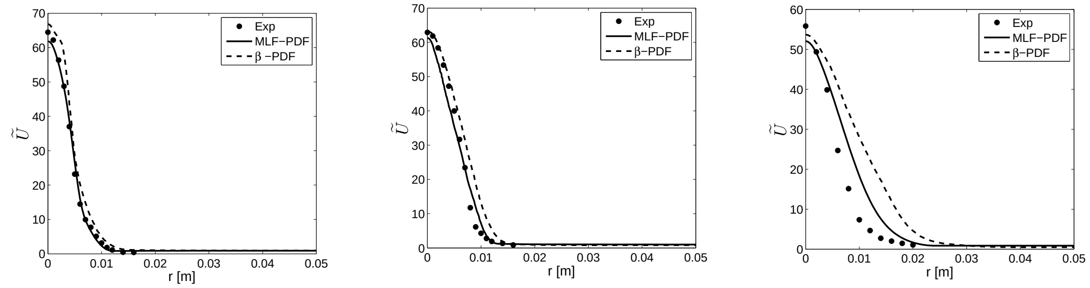

(a) x= 3d (b) x= 7.5d (c) x= 15d

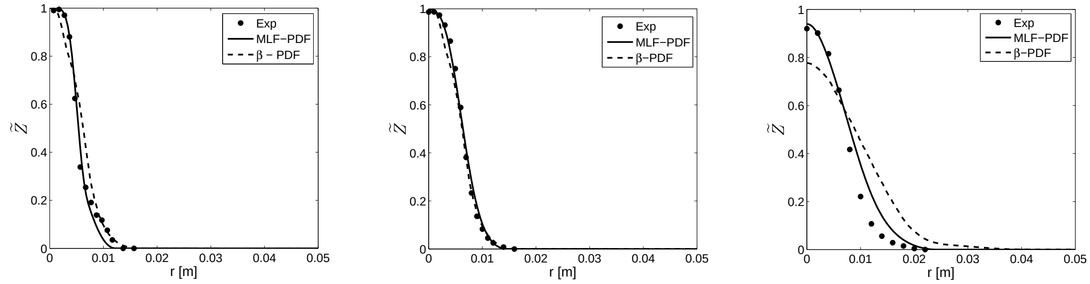

(d) x= 3d (e) x= 7.5d (f) x= 15d

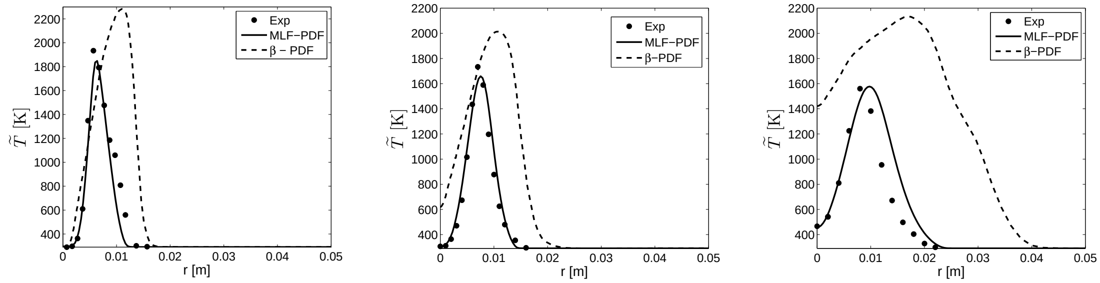

(g) x= 3d (h) x= 7.5d (i) x= 15d

Figure 6.6: Radial profiles of Favre-filtered velocity, mixture fraction and temperature at three axial locations of Flame D corresponding to simulations carried out using β-PDF and Modified laminar flame (MLF-PDF) for the progress variable description, compared to the experimental data [77, 76].

$x = 3d$. Good agreement is obtained at $x = 7.5d$ except within $(0.2d \leq r \leq 0.625d)$ where an underprediction of about 8.1% is shown. A significant discrepancy is found at $x = 15d$ which has a maximum value of 15.6% at the centerline and overprediction of (0.215) in the mixing region which is expected to significantly overpredict the width of the reaction region as observed in Fig. 6.6 and 6.7 for the plots of the temperature and the species mass fractions.

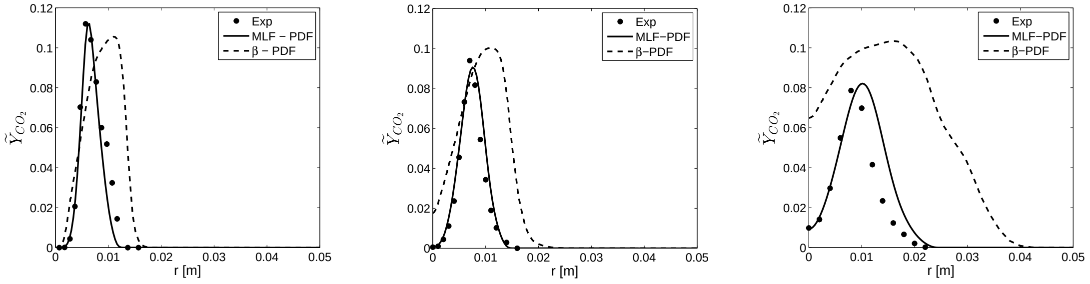

(a) x= 3d (b) x= 7.5d (c) x= 15d

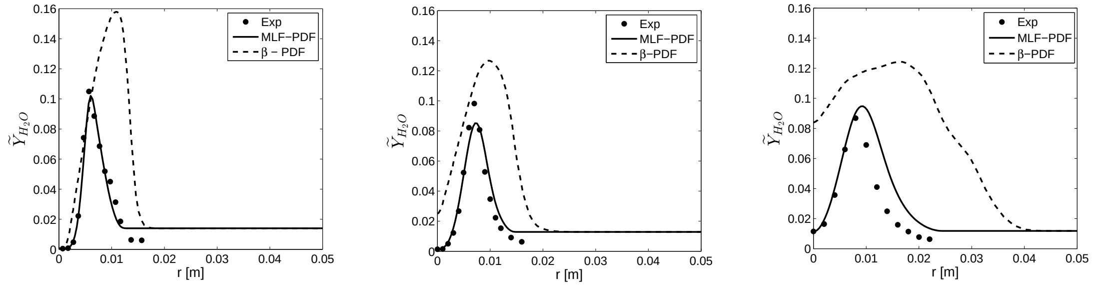

(d) x= 3d (e) x= 7.5d (f) x= 15d

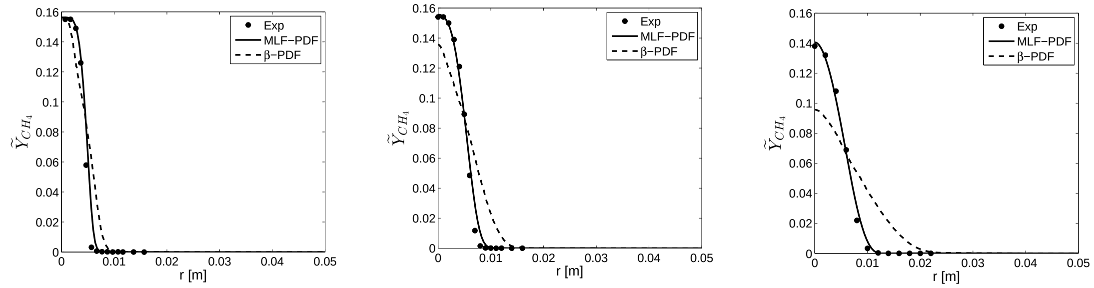

(g) x= 3d (h) x= 7.5d (i) x= 15d

Figure 6.7: Radial profiles of Favre-filtered mass fraction of major species (CO_2, H_2O and CH_4) at three axial locations of Flame D corresponding to simulations carried out using β-PDF and Modified laminar flame (MLF-PDF) for the progress variable description, compared to the experimental data [76].

A significant overprediction in temperature at all locations is obtained with a shift in the peak temperature location away from the jet center. The discrepancy of the peak temperature ranges within (15.8 - 36.8%). In addition, the overprediction in the reaction zone width justifies the overprediction in the centerline temperature at $x = 7.5d$ and $15d$. The radial profiles of the major and minor species reflect higher reaction rates that produce much more mass fractions compared to experiments.

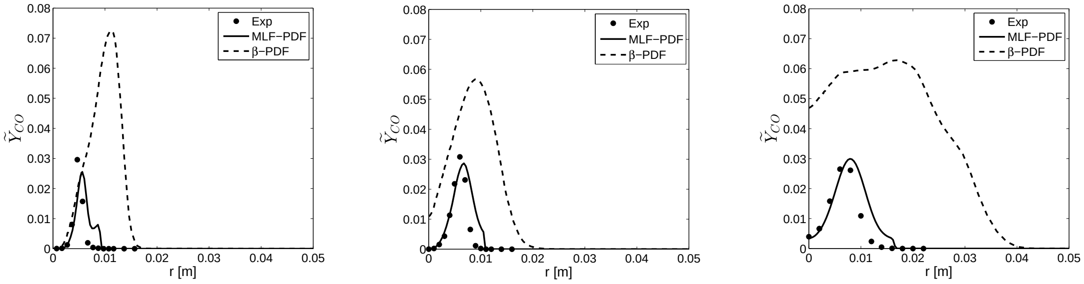

(a) x= 3d (b) x= 7.5d (c) x= 15d

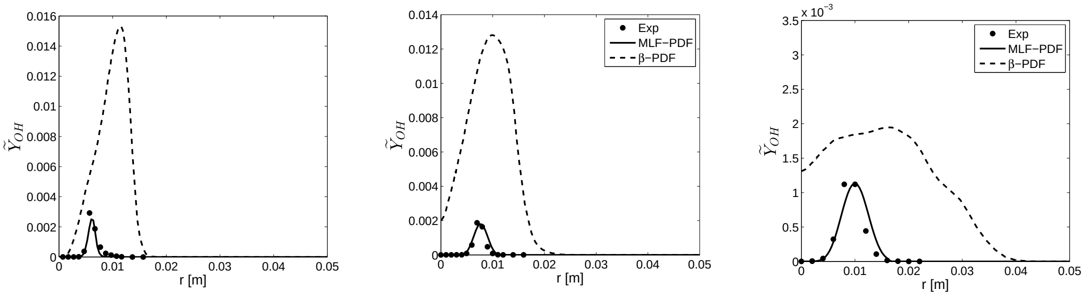

(d) x= 3d (e) x= 7.5d (f) x= 15d

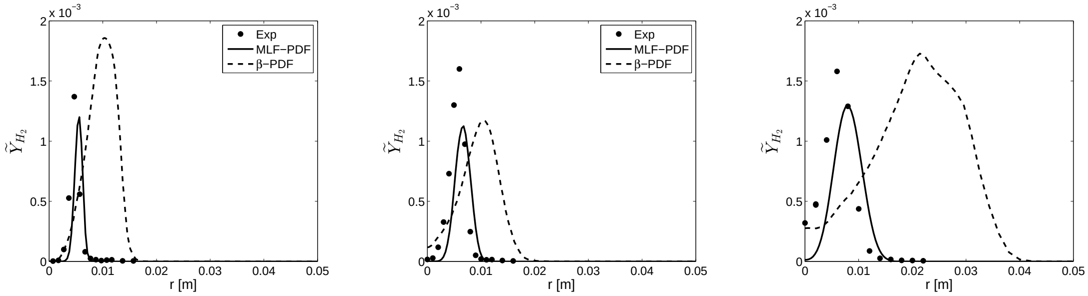

(g) x= 3d (h) x= 7.5d (i) x= 15d

Figure 6.8: Radial profiles of Favre-filtered mass fraction of minor species (CO, OH and H_2) at three axial locations of Flame D corresponding to simulations carried out using β-PDF and Modified laminar flame (MLF-PDF) for the progress variable description, compared to the experimental data [76].

In overall, the predictions obtained by using β-PDF for the progress variable are not in good agreement with the experimental data inspite of its superiority with respect to the computational cost.

Progress variable definition effect

Two different definitions for the progress variable are used in simulating flame D. Both use 50 bins in both progress variable and mixture fraction sample spaces. The comparison is applied on two axial locations ($x = 3d$) and ($x = 7.5d$). The computational time for each is comparable. In Fig. 6.9, the velocity profiles do not show a significant difference, while the mixture fraction shows underprediction within ($d \leq r \leq 1.5d$) at $x = 3d$ and ($0 \leq r \leq 0.5d$) at $x = 7.5d$ of 8.4%. The temperature profiles show an underprediction for the peak temperature of 22% and 1.7% at $x = 3d$ and $x = 7.5d$, respectively. However, the predictions at 7.5d indicates a wider reaction zone compared to experiments. In addition, the peak temperature location is shifted 1.8 mm (0.25d) outward. The major species profiles does not show significant difference from the normalized definition simulations, except for overprediction of the mass fractions of CO_2 and H_2O in the vicinity of the centerline.

As expected from the temperature profiles, the minor species show wider profiles compared to the experimental data and the normalized definition predictions, most of which do not have a significant difference from the normalized definition with respect to the peak value of each profile. It is noticeable that the peak location of minor species radial profiles at $x = 7.5d$ are shifted away from the jet axis.

Conditional filtered scalars

Good predictions are obtained in most of the conditional filtered radial profiles in consistency with the the predicted Favre-filtered fields. The temperature profiles in Fig. 6.12 show very good agreement with the experimental data with maximum discrepancy of 3.1, 4 and 8.4% at $x = 3d$, $7.5d$ and $15d$, respectively.

By examining the profiles of the major species (CO_2 and H_2O), a very good agreement with the experimental data can be observed at $x = 3d$ and $7.5d$. The maximum discrepancy that is found in CO_2 profiles is 3.7 and 4.1% at $x = 3d$ and $7.5d$, respectively. However, the peak value location is shifted towards the lean mixture (at $\eta = 0.29$) at $x = 15d$ which causes errors in the region ($0.2 \leq \eta \leq 0.45$) of 12%, in average. The profile of H_2O shows slight underprediction (6.3%) near stoichiometry at $x = 3d$, while the

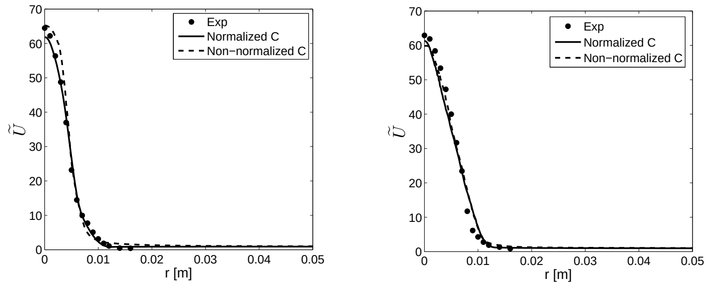

(a) x= 3d (b) x= 7.5d

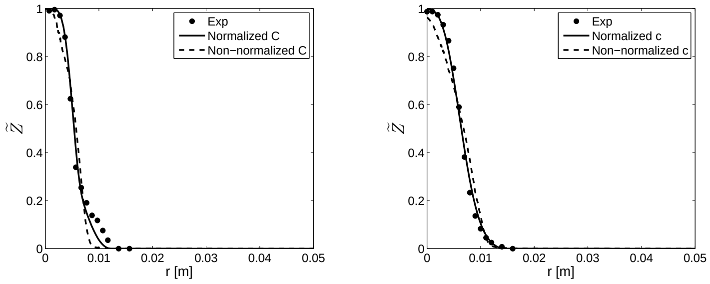

(c) x= 3d (d) x= 7.5d

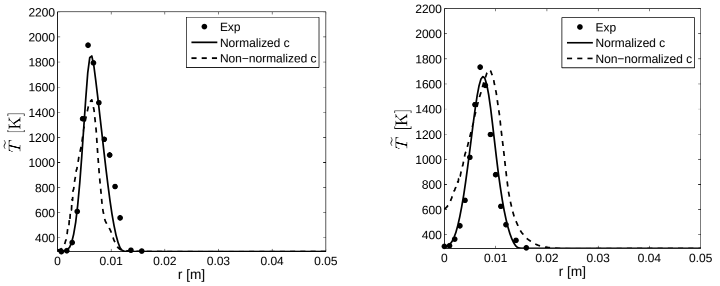

(e) x= 3d (f) x= 7.5d

Figure 6.9: Radial profiles of Favre-filtered velocity, mixture fraction and temperature at two axial locations of Flame D corresponding to simulations carried out using normalized and non-normalized progress variable definition, compared to the experimental data [77, 76].

profile shows good agreement with the experimental points at the lean and rich regions. At $x = 7.5d$, good predictions are obtained except within the rich side of the flammability region ($0.4 \leq \eta \leq 0.52$) where underpredition is encountered with maximum percentage of 10.5% around $\eta = 0.48$. A similar shift of the peak value to that observed in CO_2 is

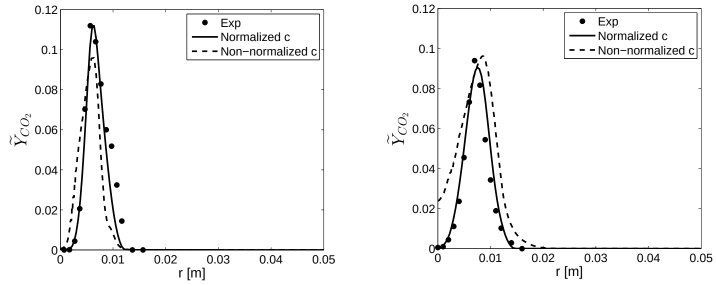

(a) x= 3d (b) x= 7.5d

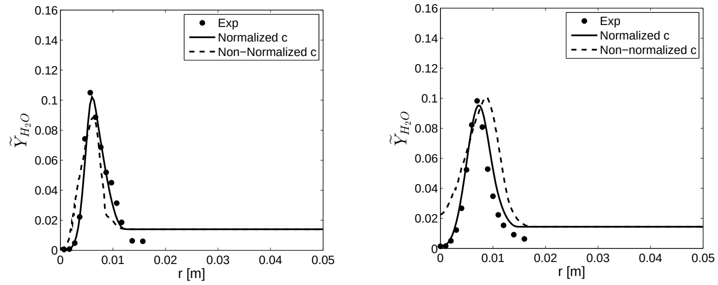

(c) x= 3d (d) x= 7.5d

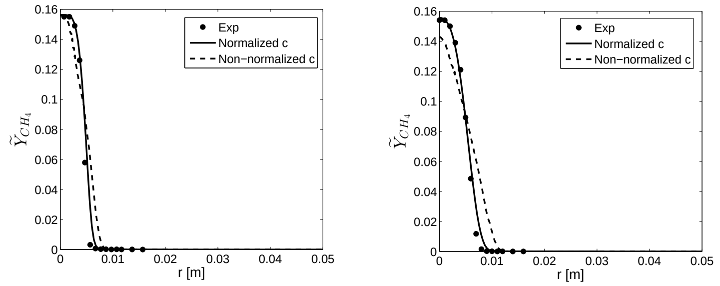

(e) x= 3d (f) x= 7.5d

Figure 6.10: Radial profiles of Favre-filtered mass fraction of major species (CO_2, H_2O and CH_4) at two axial locations of Flame D corresponding to simulations carried out using normalized and non-normalized progress variable definition, compared to the experimental data [76].

found in H_2O at $x = 15d$ which results in a maximum discrepancy of 13% at $\eta = 0.32$. In general, the discrepancies in the conditional profiles can be due to different sources of discrepancy. These sources include the inversion process, the error in presuming the PDF shape, the non-dynamic SGS model and the chemistry tables.

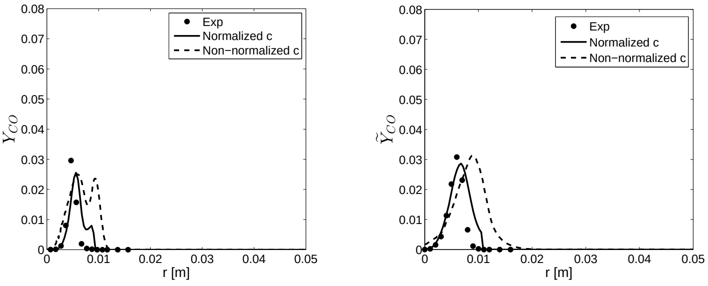

(a) x= 3d (b) x= 7.5d

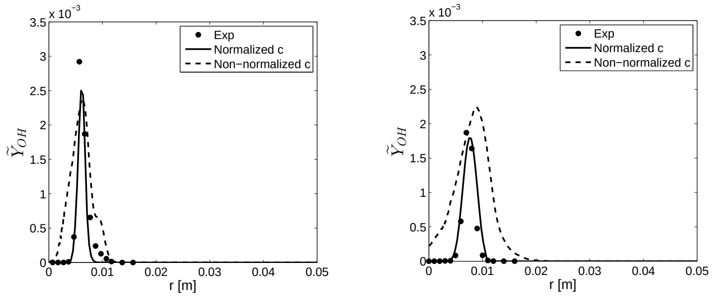

(c) x= 3d (d) x= 7.5d

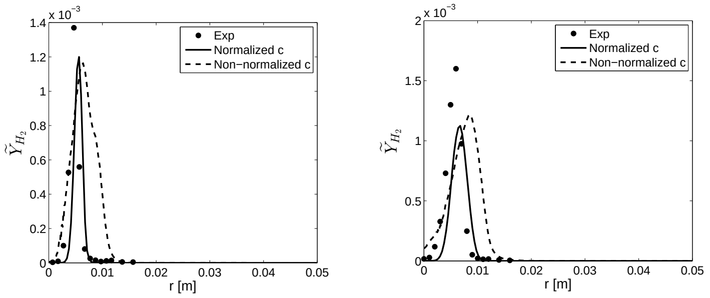

(e) x= 3d (f) x= 7.5d

Figure 6.11: Radial profiles of Favre-filtered mass fraction of minor species (CO, OH and H_2) at two axial locations of Flame D corresponding to simulations carried out using normalized and non-normalized progress variable definition, compared to the experimental data [76].

6.5.2 Flames E and F

In comparison to flame D, flames E and F represent a challenge for modelling using CSE as demonstrated by Labahn et al. [106] by pointing out that no good results have been

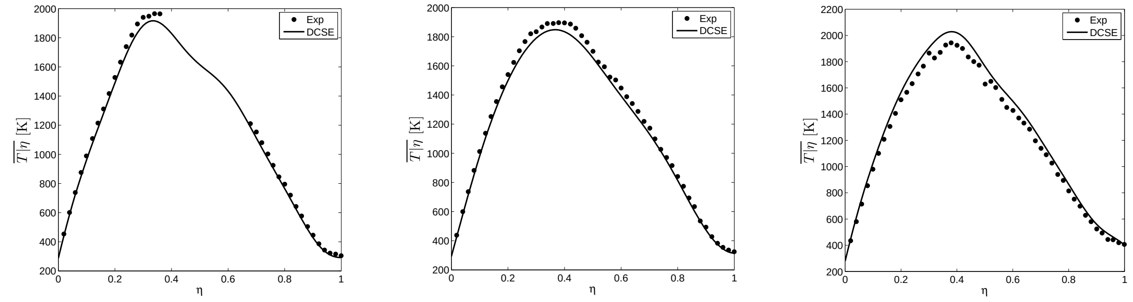

(a) x= 3d (b) x= 7.5d (c) x= 15d

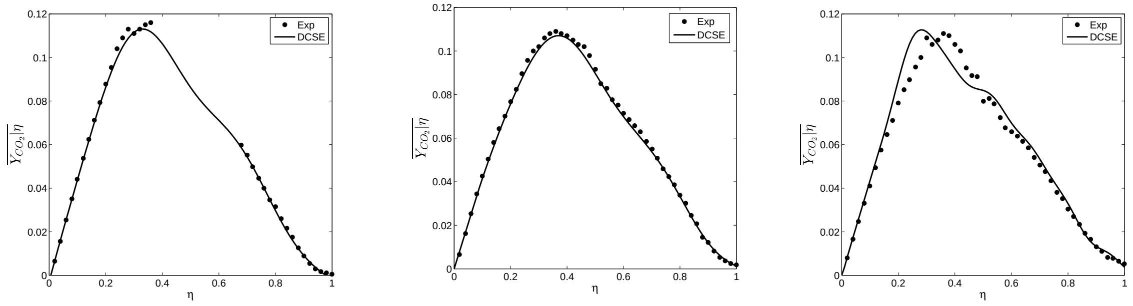

(d) x= 3d (e) x= 7.5d (f) x= 15d

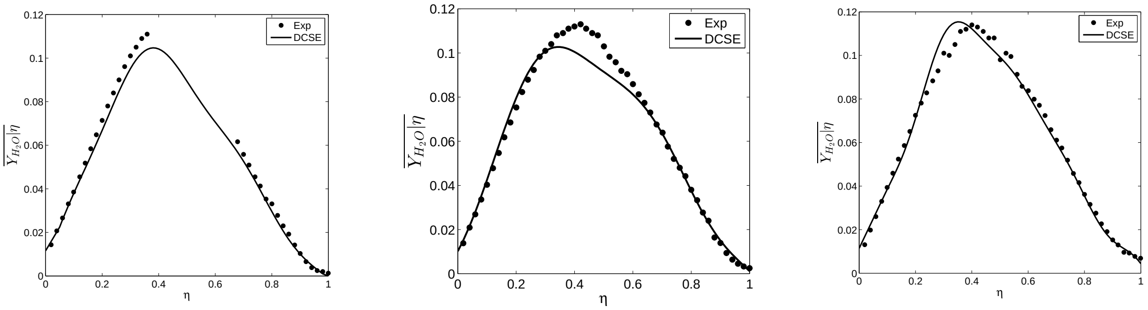

(g) x= 3d (h) x= 7.5d (i) x= 15d

Figure 6.12: Radial profiles of conditional-filtered temperature and mass fractions of CO_2 and H_2O at three axial locations of Flame D using 50 bins in the progress variable sample space and MLF-PDF for the normalized progress variable, compared to the experimental data [76].

obtained for flame F in RANS-CSE. The current investigation is expected to be different as

DCSE has much less fluctuations about the conditional filtered quantities than the single CSE, which means the assumption of neglecting the fluctuation about the conditional quantities is more reasonable. The challenging factor is the higher rate of local extinction that is expected in flames E and F compared flame D. LES-DCSE is used to simulate flames E and F using 50 bins in both mixture fraction and progress variable sample spaces. The MLF-PDF and the normalized form are used for the progress variable. In the current section, the Favre-filtered radial profiles of mixture fraction, temperature, major species (CO_2, H_2O and CH_4), and minor species (CO, OH and H_2) mass fraction are introduced at two axial locations ($x = 3d$) and ($x = 7.5d$), which are illustrated in Figs (6.13 - 6.18). The two locations of 3d and 7.5d are used due to convergence issue and the fact that they are located in the region where location extinction occurs due to the presence of high strain rates.

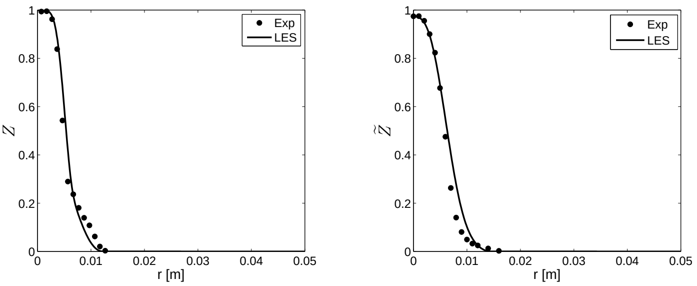

(a) x= 3d (b) x= 7.5d

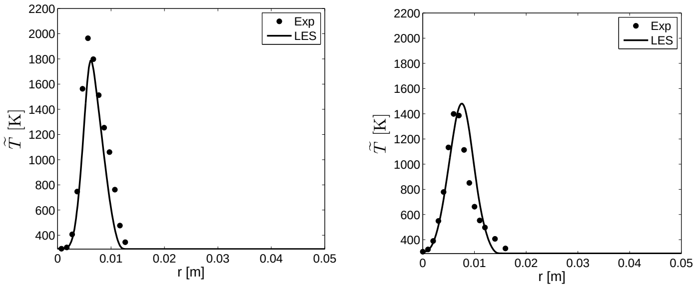

(c) x= 3d (d) x= 7.5d

Figure 6.13: Radial profiles of Favre-filtered velocity, mixture fraction and temperature at two axial locations of Flame E corresponding to simulations carried out using normalized and non-normalized progress variable definition, compared to the experimental data [76].

Starting by flame E profiles, the mixture fraction predictions show good agreement with the experimental data with some discrepancies that have a maximum value of 0.06 at $r =$

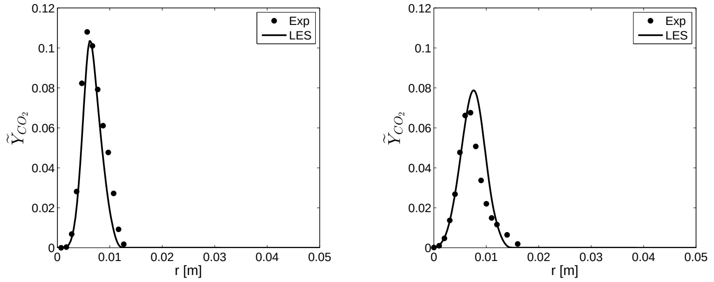

(a) x= 3d (b) x= 7.5d

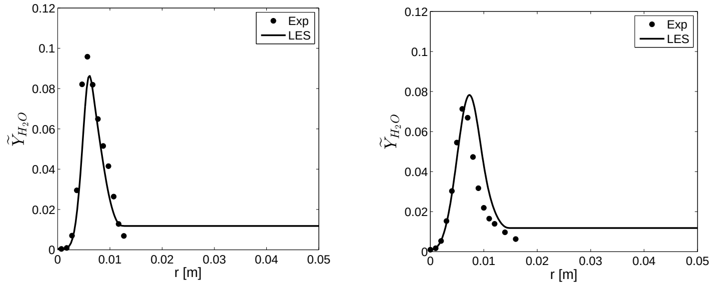

(c) x= 3d (d) x= 7.5d

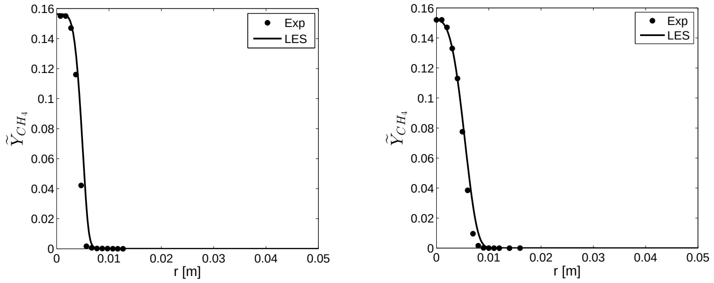

(e) x= 3d (f) x= 7.5d

Figure 6.14: Radial profiles of Favre-filtered mass fraction of major species (CO_2, H_2O and CH_4) at two axial locations of Flame E corresponding to simulations carried out using normalized and non-normalized progress variable definition, compared to the experimental data [76].

$1.35d$ and $x = 3d$ and 0.14 at $r = 1.1d$ and $x = 7.5d$. The temperature profiles follow the same shape that is formed by the experimental points with a maximum discrepancy of 9.2% and 5.8% for the peak temperature at $x = 3d$ and $7.5d$, respectively. The underprediction in the mixture fraction profiles in the region of ($d \leq r \leq 1.67d$) results in the shift observed in the curve to the right at $x = 7.5d$, which might be solved by employing dynamic SGS model in the future. Similar to the temperature profiles, the major species mass fraction profiles exhibit some discrepancies, although good agreement with the experimental data is achieved. At $x = 3d$, the discrepancy in CO_2 peak value is 4.2% and in H_2O peak value is 9.9%, while they are 16 % and 10.6 % at $x = 7.5d$ for CO_2 and H_2O, respectively. No significant problems are encountered in CH_4 mass fraction profiles. The minor species (CO, OH and H_2) show an underprediction for CO and H_2 mass fraction profiles at $x = 3d$ ranges within (11.9 - 39.7%), while OH profile has an overprediction in the peak value equals to 28%. Further, all the minor species show overprediction at $x = 7.5d$ with a considerable good agreement with the experimental data within ($0 \leq r \leq 0.7d$). The discrepancies encountered at these locations can be referred to the effect of the pilot which might interfere with the statistical description of the mixing field and the progress variable at these locations. By examining predictions of flame F, the mixture fraction profiles show similar problems to those observed in flame E profiles within the region of ($0.95d \leq r \leq 1.96d$) where the mixture fraction shows underprediction at $x = 3d$ and overprediction at $x = 7.5d$. The temperature profiles show a good agreement with experimental data with maximum discrepancy of 7.9% and 4.2% at $x = 3d$ and $7.5d$, respectively. In spite of the shift in CO_2 and H_2O curves, they show very good agreement with experiments considering how these locations are challenging. Similar to flame E, CH_4 mass fraction profiles are in good agreement with experiments. Regarding the minor species, some profiles show significant discrepancies which are mainly at $x = 3d$ and the discrepancy level decreases at $x = 7.5d$ to show better agreement with experimental data. This might be due to the high temperature that is convected from the pilot to the first location ($x = 3d$) which has a contradiction with the temperature assumed for the initialization of reactions at the generation of TGLDM trajectories, which is 300K. The generation of reaction trajectories that are initiated at elevated temperature and used only for the ensembles close to the pilot inlet, may be a potential improvement for the predictions at the location close to the pilot.

Another source of discrepancies is the effect of the products that are issued from the pilot on the PDF description, as the discrepancy in water mass fraction field will result in a discrepancy in the progress variable chemical source term. Conceptually, the mass fraction of water, that is provided to the inversion, is supposed to be due to the flame chemical reaction, while the mass fraction that is presented close to the jet is a summation of that created by the reaction and the amount that comes from the pilot. The approximation in the presumed shape of current joint FDF is not believed to be the major source of errors in the minor species mass fractions considering the recent results of Hendra and Bushe

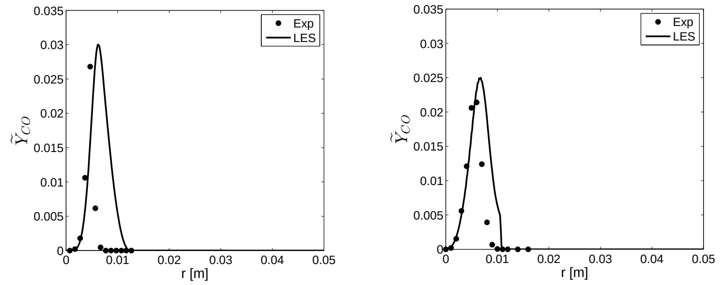

(a) x= 3d (b) x= 7.5d

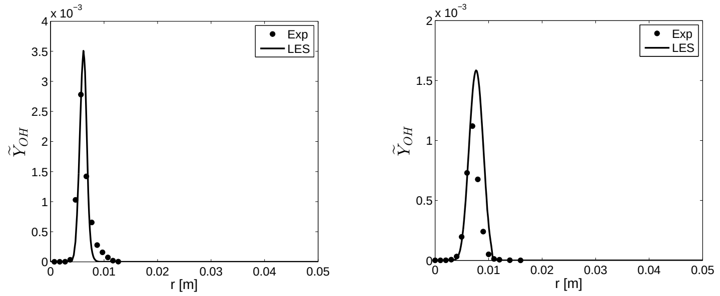

(c) x= 3d (d) x= 7.5d

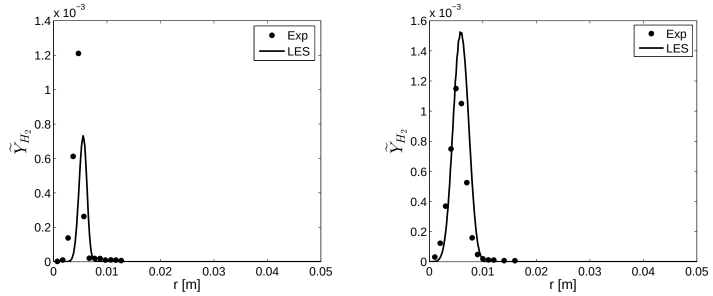

(e) x= 3d (f) x= 7.5d

Figure 6.15: Radial profiles of Favre-filtered mass fraction of minor species $(\mathrm{CO}, \mathrm{OH}$ and $\mathrm{H}_2)$ at two axial locations of Flame E corresponding to simulations carried out using normalized and non-normalized progress variable definition, compared to the experimental data [76].

[108] showing similar discrepancies in the minor species concentrations with the joint PDF is extracted from experimental data. The observations point towards some inaccuracies in chemical kinetics and the tabulation technique.

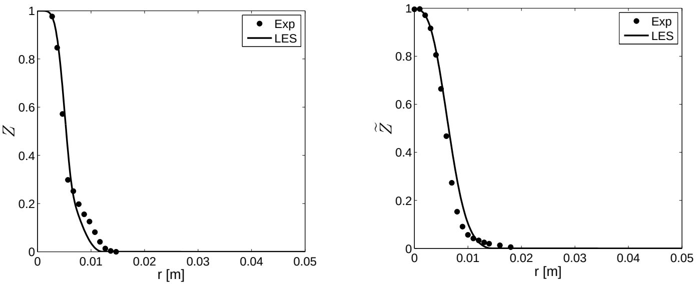

(a) x= 3d (b) x= 7.5d

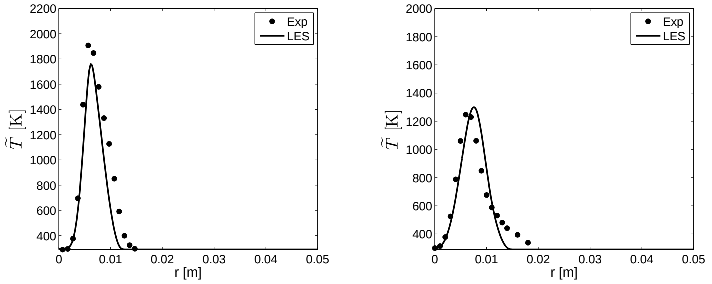

(c) x= 3d (d) x= 7.5d

Figure 6.16: Radial profiles of Favre-filtered velocity, mixture fraction and temperature at two axial locations of Flame F corresponding to simulations carried out using normalized and non-normalized progress variable definition, compared to the experimental data [76].

6.5.3 Qualitative observation

One of the main targets of the current investigation is to assess the ability of DCSE to reproduce the local extinction and reignition phenomena in LES. Although an overall good results are obtained for the three flames at the region where these phenomena occur, a qualitative presentation using the temporal instantaneous frames of the flames will ensure the assessment. There are different ways to check for the presence of local extinction in the flame structure. The filtered-temperature instantaneous frames are used by Ihme and Pitsch [96] and the investigation of Garmory and Mastorakos [105]. Both studies show low temperature patches within the flammability limits within the region that extends from the domain inlet till 14d downstream of the fuel exit. Further, Garmory and Mastorakos have used peak conditional SDR, stoichiometric conditional temperature and OH mass fraction plots with respect to time, to prove the extinction and reignition that take place in the region (5d $\leq$ x $\leq$ 8.6d). In the present investigation, the filtered reaction rates of OH ($\overline{\dot{\omega}_{\mathrm{OH}}}$

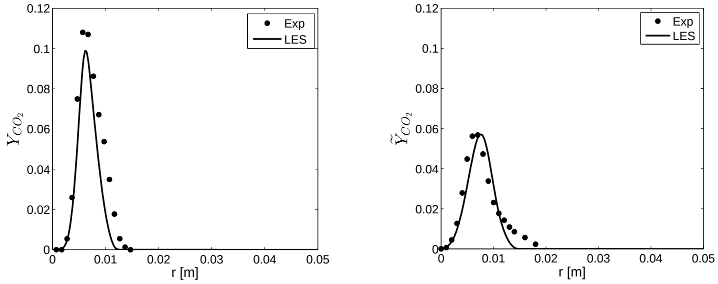

(a) x= 3d (b) x= 7.5d

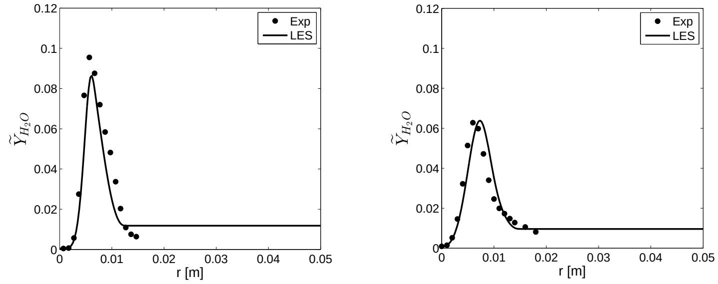

(c) x= 3d (d) x= 7.5d

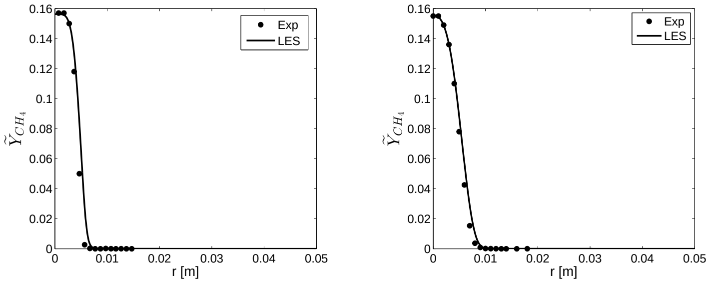

(e) x= 3d (f) x= 7.5d

Figure 6.17: Radial profiles of Favre-filtered mass fraction of major species (CO_2, H_2O and CH_4) at two axial locations of Flame F corresponding to simulations carried out using normalized and non-normalized progress variable definition, compared to the experimental data [76].

are used to mark the chemical reactions of the flames. The selection of OH reaction rates over OH mass fraction is to avoid the effect of turbulent transport of OH mass fraction that might make it hard to observe local extinction and reignition. The local extinction

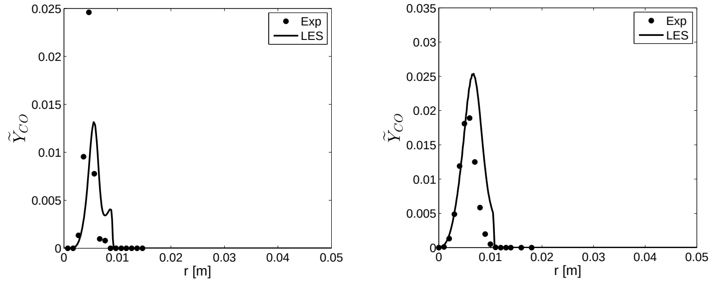

(a) x= 3d (b) x= 7.5d

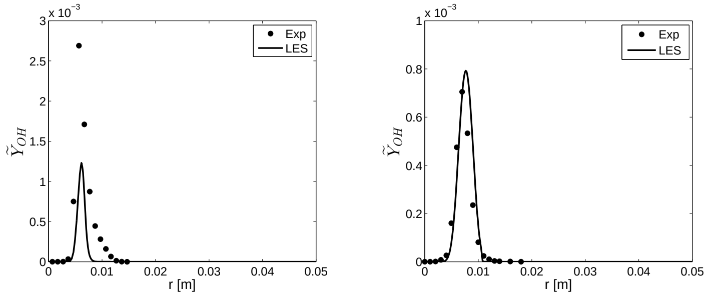

(c) x= 3d (d) x= 7.5d

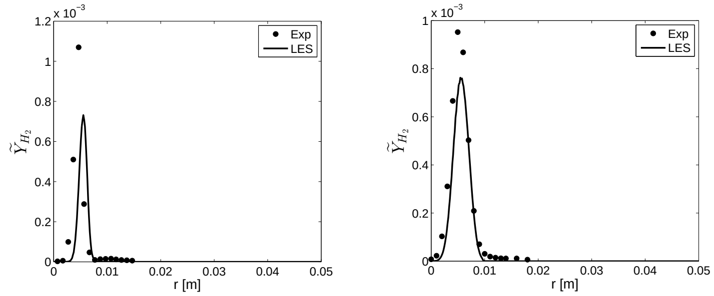

(e) x= 3d (f) x= 7.5d

Figure 6.18: Radial profiles of Favre-filtered mass fraction of minor species (CO, OH and H_2) at two axial locations of Flame F corresponding to simulations carried out using normalized and non-normalized progress variable definition, compared to the experimental data [76].

locations can be observed in Figs. (6.19-6.21) as the locations with zero reaction rates (white spots) within the flammability region. The instantaneous frames barely show local extinction in Fig. 6.19 for flame D. On the other hand, many local extinction locations can be observed in Figs 6.20 and 6.21 within the region $(7d \leq x \leq 14d)$ and $(5.5d \leq x \leq 10d)$

for flame E and F, respectively. The instantaneous stoichiometric iso-surface of Flame (D-F) that is shown in Fig. 6.22 supports the local extinction observation in Flame E and F, as it shows the expected patches of low temperature on the stoichiometric iso-surface that drops below 1200 K in a good agreement with the observations of Garmory and Mastorakos [105].

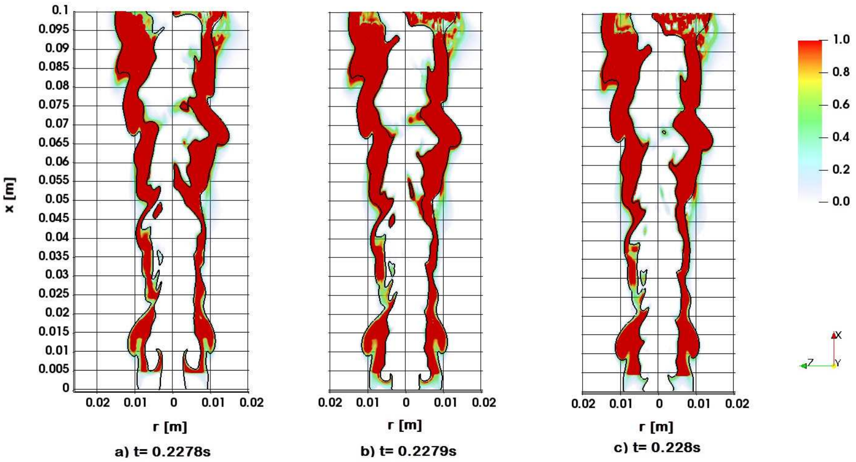

a) t= 0.2278s b) t= 0.2279s c) t= 0.228s

Figure 6.19: Mixture fraction isolines, that represent the flammability limits (Z=0.2 and Z=0.6), superimposed on instantaneous filtered OH reaction rates (1/s) color map of flame D central plane.

6.6 Summary

DCSE is used in LES framework to investigate a series of methane-piloted flames that encounter an increasing level of local extinction and reignition. The investigation employs detailed chemistry which is provided in the form of three dimensional tables by TGLDM. Different analyses are carried out in the present study based on Flame D that include the selection of ensembles and turbulent Schmidt number. The results show better prediction of flame D for the simulation that uses 50 bins in the progress variable sample space, simulation that uses MLF-PDF for the progress variable and the normalized form of the progress variable compared to using 20 bins, β-PDF and the non-normalized progress variable form, respectively. An overall good predictions are obtained for Sandia flames (D-F) at the inspected axial locations based on the Favre-filtered radial profiles of velocity, mixture fraction, temperature, mass fraction of major species (CO_2, H_2O and CH_4) and the minor ones (CO, OH and H_2). The discrepancies presented significantly in the minor

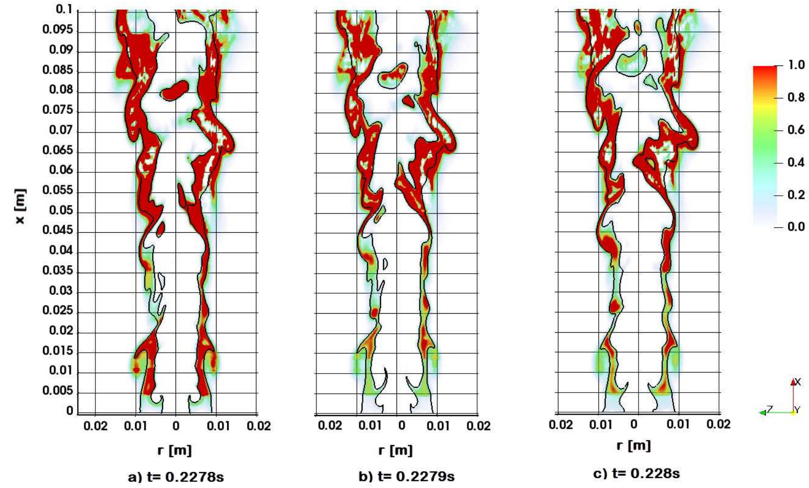

a) t= 0.2278s b) t= 0.2279s c) t= 0.228s

Figure 6.20: Mixture fraction isolines, that represent the flammability limits (Z=0.2 and Z=0.6), superimposed on instantaneous filtered OH reaction rates (1/s) color map of flame E central plane.

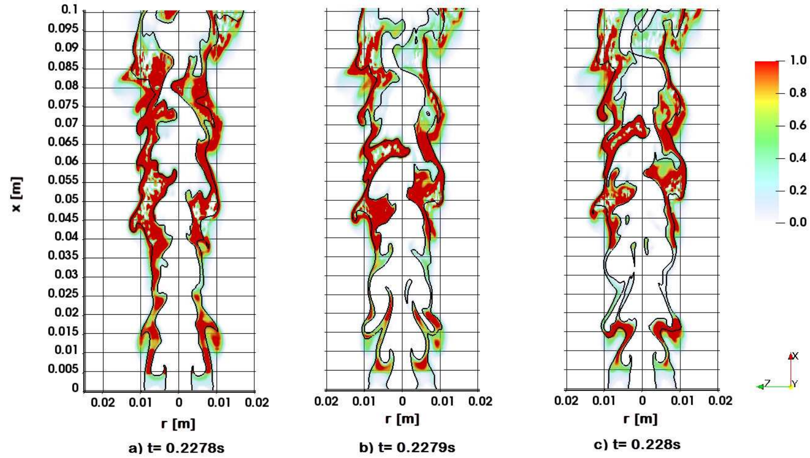

a) t= 0.2278s b) t= 0.2279s c) t= 0.228s

Figure 6.21: Mixture fraction isolines, that represent the flammability limits ($\widetilde{Z}$=0.2 and $\widetilde{Z}$=0.6), superimposed on instantaneous filtered OH reaction rates (1/s) color map of flame F central plane.

species profiles at $x = 3d$ which are expected to be due to the effect of the pilot, in addition to the discrepancy in the mixture fraction field that is referred to the constant SGS model. The good predictions obtained by LES-DCSE are reinforced by the qualitative observations that ensure the reproduction of the local extinction and reignition phenomena

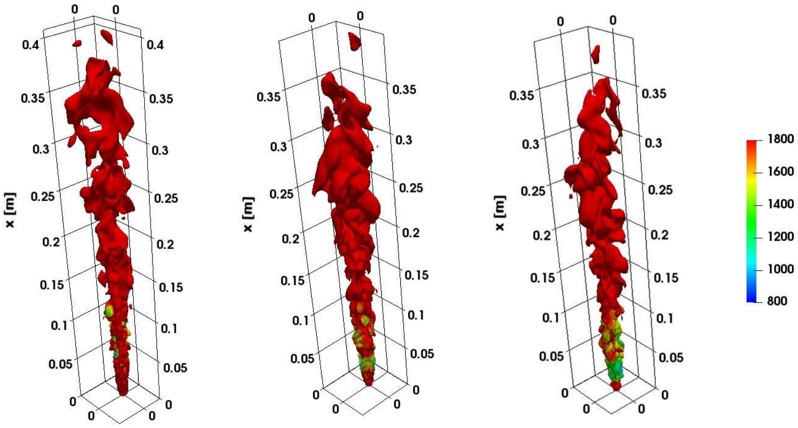

a) Flame D

b) Flame E

c) Flame F

Figure 6.22: Instantaneous stoichiometric iso-surface coloured by Favre-filtered instantaneous temperature contours in [K] for Flame a) D, b) E and c)F.

using instantaneous frames of OH reaction rates and temperature.

Chapter 7

Conclusions

The main objective of the present dissertation is to provide an assessment of DCSE with LES, with emphasis on recreating challenging reactive flow characteristics. The good predictions make LES-DCSE promising for industrial investigations. The major findings and conclusions are presented in the current chapter, followed by some recommendations for future work.

7.1 Summary of main findings

In Chapter 4, RANS simulations of a series of lifted turbulent jet flames initially performed by Dovizio et al.[8] were revisited. In the present work, a more advanced SDR formulation [9] was implemented and a different numerical technique was investigated to solve the inverted integral equation. In particular, LSQR algorithm instead of LU-decomposition, was examined. The predictions obtained for the radial profiles of methane concentration at different radial locations have shown good agreement with the experimental results. Different approaches were used to estimate the lift-off height from the numerical results. For the different criteria, the trends in the lift-off height predictions remained the same and the relative difference between the lowest and largest predicted lift-off height ranged from 15% for Re = 7000 to 21% for Re = 12,000, consistent with previous work [8]. The SDR model was shown to have an impact on the lift-off height predictions, in particular for the two largest Reynolds numbers. Keeping the first criterion based on the OH mass fraction [60], the differences between the current lift-off height predictions and those reported by Dovizio et al. [8] with the simple algebraic model were 7%, 15% and 29% for Re = 7000, Re = 12000 and Re = 19500, respectively. The LSQR algorithm was shown to reduce the inversion computational time by 60%, while keeping the the same, if not higher accuracy than the LU decomposition.

In Chapter 5, LES of a series of lifted turbulent jet flames in cold air (no autoignition is present) has been performed using DCSE for partially-premixed turbulent combustion for the first time. The two conditioning variables are mixture fraction, to describe the non-premixed flame mode, and a progress variable based on CO_2, to include the premixed flame propagation. Predictions of methane concentration and rms are compared with available experimental data for the non-reacting methane jet at the lowest Reynolds number, Re = 7000. Good agreement is found with larger discrepancies for the rms. Possible numerical inaccuracies may come from some uncertainties in the turbulent inlet conditions (no experimental measurements are reported at the nozzle exit) and the constant Smagorinsky model. For the reacting conditions, time-averaged methane concentration profiles, jet width and methane concentration PDFs are compared with the experimental data available for the lowest Re flame. Reasonable agreement between the predictions and experimental data is found for the axial methane concentration. However, around the lift-off height the relative difference between the LES and experimental values is small, 17%. For the remaining variables, very good agreement between the present LES and experiments is observed. The methane concentration PDF profiles are well reproduced with a shift in the peak location, consistent with the small underprediction of the peak value in the methane concentration radial profiles. These good PDF predictions demonstrate that the predicted level of turbulent fluctuations in the present LES is reasonable in comparison to the experimental conditions. For the three flames, flammability region width and lift-off height are determined and compared with experimental data. The predicted flammability region is within the experimental range of values for each flame. Excellent agreement with the experimental measurements is found for the lift-off height. The present LES-DCSE calculations also bring some improvement over what was obtained in previous RANS-DCSE [8] due to more accurate description of the turbulent flow/mixing fields and submodels for the closure of the progress variable transport equation. Further qualitative analysis is conducted on a few other aspects of the flames. The predicted methane decay rate in the flame is found to be in agreement with the experimental observations. Some evidence of a triple/edge flame is noted, confirming the partially-premixed flame propagation. The progress variable SDR model is shown to have an impact on the lift-off height predictions. The simple relaxation model yields lift-off values that are 43% larger than those predicted by the modified expression of Dunstan et al. [156]. In agreement with previous studies [166, 167], the linear relaxation model does not appear to be sufficiently accurate for the present conditions. For the current simulations, the NPMC term included for the closure of the progress variable transport equation is shown to have a small impact on the predicted lift-off heights, but have a much larger effect on the progress variable and temperature field.

In Chapter 6, a series of methane-piloted flames with varying levels of local extinction are investigated in LES using DCSE in combination with the TGLDM approach for chemistry reduction and tabulation. Good agreement with experimental data is obtained for predictions obtained for the three flames (D, E and F) at the locations of comparison based on Favre-filtered radial profiles of velocity, mixture fraction, temperature and species mass fractions. Based on flame D simulations, additional analyses are introduced to assess the quality of predictions when using 20 bins in progress variable sample space, the β-PDF to model the progress variable statistical distribution, and the non-normalized form of the progress variable. The results show significantly better performance for using 50 bins in the progress variable sample space compared to 20 bins. Using β-PDF for the progress variable saves 67% of the computational cost consumed by MLF-PDF. However, it severely overpredicts reactive scalars which makes it unsuitable. The non-normalized form of the progress variable shows comparable performance to that obtained by the normalized form with some discrepancies presented for the favor of the normalized. That can be referred to the better description of the progress variable dependence on the mixture fraction that the normalized form provides in its transport equations. The predictions of flame E and F shows good agreement with experimental data for the major species and large discrepancies in the minor species radial profiles. These discrepancies may be due to the effect of the pilot at the locations very close to the inlet. In addition, the discrepancies present in the velocity and mixture fraction fields may stem from the non-dynamic Smagorinsky SGS model. The instantaneous frames of OH reaction rates for flames (D-F) managed to capture the local extinction phenomenon as blank spots (with close or equal to zero reaction) that appear in the flammable region. They also show higher levels of extinction in E and F compared to D.

7.2 Summary of accomplishments

A list of the main outcomes is provided here:

- Numerical simulations of series of turbulent lifted flames using RANS-DCSE to assess the quality of a least squares method technique (LSQR) and the effect of an elaborate progress variable SDR model. LSQR has shown better simulation quality in DCSE results and the more detailed SDR model has an impact on the lift-off height of the three flames.

- The partially premixed DCSE formulation was extended to LES framework to provide better description for the mixing field and allow for further assessment of the model by comparing the PDF and fluctuations of methane concentration with experimental data, in addition to better qualitative investigation. LES-DCSE successfully reproduced the lift-off phenomena for a series of turbulent jet lifted flames with good agreement with the experimental data

- The partially premixed DCSE formulation is used to simulate a series of methane flames with high level of local extinction. LES-DCSE succeeded in capturing the local extinction, especially in flame E and F. A good agreement is obtained for the reactive scalars profiles.

7.3 Future work

It is clear from the previous and current CSE/DCSE investigations that most of the implementations of CSE/DCSE are carried out using a simple geometry that is modelled in cylindrical domain. As DCSE has achieved success in LES with challenging transient phenomena, the next step should be investigating practical burners with complex geometries. It will be interesting to investigate ensemble configuration selection in complex geometries. In such cases, coupling LES-DCSE with the dynamic ensemble selection technique [126] might be needed if the conventional ensemble selection fails to provide good performance. As many combustion applications are operating on liquid fuel spray systems such as IC engines and rocket propulsion, DCSE should be extended to multiphase combustion. Recently, Doubly CMC has achieved success in simulating spray combustion [31]. Therefore, extending DCSE to spray combustion will be of interest as some spray combustion processes are described as partially premixed [177]. A comparative study can be carried out between DCMC and DCSE in spray flames.

Most of CSE/DCSE-TGLDM investigations are based on simple fuel such as methane and methanol. The next target can be examining the performance of CSE/DCSE with more complicated fuels such as oxy-fuel and syngas (combination of CO, CO_2 and H_2) which are commonly used in industry. This will require modifications to the chemistry reduction and tabulation technique that involves selection of additional progress variable for the reaction trajectories generation and additional dimension(s) to be introduced in the chemistry tables.

References

[1] The International Energy Agency (IEA), World energy outlook 2017, Executive summary (2017).

[2] Natural Resources Canada, Renewable energy facts (Oct. 2019).

[3] The International Energy Agency (IEA), Global energy and CO_2 status report (2017).

[4] Environment and Climate Change Canada's website, National Inventory Report 1990–2017: Greenhouse Gas Sources and Sinks in Canada: Executive Summary, Tech. rep., The Pollutant Inventories and Reporting Division (2019).

[5] K. Bray, P. Domingo, L. Vervisch, Role of the progress variable in models for partially premixed turbulent combustion, Combust. Flame 141 (4) (2005) 431 – 437.

[6] N. Peters, Tubulent Combustion, Cambridge University Press, 2000.

[7] K. M. Lyons, Toward an understanding of the stabilization mechanisms of lifted turbulent jet flames: Experiments, Prog. Energy Combust. Sci. 33 (2) (2007) 211 – 231.

[8] D. Dovizio, J. W. Labahn, C. B. Devaud, Doubly conditional source-term estimation (DCSE) applied to a series of lifted turbulent jet flames in cold air, Combust. Flame 162 (5) (2015) 1976 – 1986.

[9] D. Dovizio, C. Devaud, Doubly conditional source-term estimation (DCSE) for the modelling of turbulent stratified V-shaped flame, Combust. Flame 172 (2016) 79 – 93.

[10] H. Kolla, J. W. Rogerson, N. Chakraborty, N. Swaminathan, Scalar dissipation rate modeling and its validation, Combust. Sci. Technol. 181 (3) (2009) 518–535.

[11] M. Mortada, C. Devaud, Numerical investigation of doubly conditional source-term estimation applied to turbulent partially premixed combustion, in: Proc. Combust. Inst. - Can. Sec., University of Waterloo, 2016.

[12] R. Schefer, M. Namazian, J. Kelly, Structural characteristics of lifted turbulent-jet flames, in: Symp. (Int.) Combust., Vol. 22, 1989, pp. 833–842.

[13] R. Schefer, P. Goix, Mechanism of flame stabilization in turbulent, lifted-jet flames, Combust. Flame 112 (4) (1998) 559–574.

[14] T. Poinsot, D. Veynante, Theoretical and numerical combustion, Edwards, 2005.

[15] S. Pope, Turbulent Flows, Cambridge Press, 2000.

[16] J. Smagorinsky, General circulation experiments with the primitive equations, Mon. Weather Rev. 91 (3) (1963) 99–164.

[17] M. Germano, U. Piomelli, P. Moin, W. H. Cabot, A dynamic subgrid-scale eddy viscosity model, Phys. Fluids 3 (7) (1991) 1760–1765.

[18] X. Chai, K. Mahesh, Dynamic equation model for large-eddy simulation of compressible flows, J. Fluid Mech. 699 (2012) 385–413.

[19] T. Echekki, E. Mastorakos, Turbulent Combustion Modeling: Advances, New Trends and Perspectives., Springer, 2011.

[20] R. Bilger, S. Pope, K. Bray, J. Driscoll, Paradigms in turbulent combustion research, Proc. Combust. Inst. 30 (1) (2005) 21 – 42.

[21] B. Magnussen, B. Hjertager, On mathematical modeling of turbulent combustion with special emphasis on soot formation and combustion, Symp. (Int.) Combust. 16 (1) (1977) 719 – 729.

[22] D. Spalding, Mixing and chemical reaction in steady confined turbulent flames, Symp. (Int.) Combust. 13 (1) (1971) 649 – 657.

[23] R. Cant, E. Mastorakos, An Introduction to Turbulent Reacting Flows, Imperial College Press, 2008.

[24] N. Peters, Local quenching due to flame stretch and non-premixed turbulent combustion, Combust. Sci. Technol. 30 (1-6) (1983) 1–17.

[25] V. Kuznetsov, Effect of turbulence on the formation of large superequilbrium concentration of atoms and free radicals in diffusion flames, Mehan. Zhidkosti Gasa 6 (1982) 3–9.

[26] F. A. Williams, Recent Advances in Theoretical Descriptions of Turbulent Diffusion Flames, Springer New York, 1975, pp. 189–208.

[27] K. Bray, J. Moss, A unified statistical model of the premixed turbulent flame, Acta Astronautica 4 (3) (1977) 291 – 319.

[28] R. W. Bilger, Conditional moment closure for turbulent reacting flow, Phys. Fluids 5 (2) (1993) 436–444.

[29] A. Y. Klimenko, Multicomponent diffusion of various admixtures in turbulent flow, Fluid Dyn. 25 (3) (1990) 327–334.

[30] A. Klimenko, R. Bilger, Conditional moment closure for turbulent combustion, Prog. Energy Combust. Sci. 25 (1999) 595 – 687.

[31] M. P. Sitte, E. Mastorakos, Large eddy simulation of a spray jet flame using doubly conditional moment closure, Combust. Flame 199 (2019) 309 – 323.

[32] A. Kronenburg, R. Bilger, J. Kent, Modeling soot formation in turbulent methane–air jet diffusion flames, Combust. Flame 121 (1) (2000) 24 – 40.

[33] R. M. Woolley, M. Fairweather, Yunardi, Conditional moment closure modelling of soot formation in turbulent, non-premixed methane and propane flames, Fuel 88 (3) (2009) 393 – 407.

[34] N. Swaminathan, K. Bray, Turbulent Premixed Flames, Cambridge University Press, 2011.

[35] S. Amzin, N. Swaminathan, J. W. Rogerson, J. H. Kent, Conditional moment closure for turbulent premixed flames, Combust. Sci. Technol. 184 (10-11) (2012) 1743–1767.

[36] D. Farrace, K. Chung, S. S. Pandurangi, Y. M. Wright, K. Boulouchos, N. Swaminathan, Unstructured LES-CMC modelling of turbulent premixed bluff body flames close to blow-off, Proc. Combust. Inst. 36 (2) (2017) 1977 – 1985.

[37] S. B. Pope, Lagrangian PDF methods for turbulent flows, Ann. Rev. Fluid Mech. 26 (1994) 23–26.

[38] S. B. Pope, A Monte Carlo method for the PDF equations of turbulent reactive flow, Combust. Sci. Technol. 25 (5-6) (1981) 159–174.

[39] S. Pope, PDF methods for turbulent reactive flows, Prog. Energy Combust. Sci. 11 (2) (1985) 119 – 192.

[40] L. Valiño, A field Monte Carlo formulation for calculating the probability density function of a single scalar in a turbulent flow, Flow Turbul. Combust. 60 (2) (1998) 157–172.

[41] V. Sabel'nikov, O. Soulard, Rapidly decorrelating velocity-field model as a tool for solving one-point fokker-planck equations for probability density functions of turbulent reactive scalars, Phys. Rev. E 72 (2005) 163001–163022.

[42] A. Y. Klimenko, S. B. Pope, The modeling of turbulent reactive flows based on multiple mapping conditioning, Phys. Fluids 15 (7) (2003) 1907–1925.

[43] M. Cleary, A. Klimenko, J. Janicka, M. Pfitzner, A sparse-lagrangian multiple mapping conditioning model for turbulent diffusion flames, Proc. Combust. Inst. 32 (1) (2009) 1499 – 1507.

[44] K. Vogiatzaki, A. Kronenburg, M. Cleary, J. Kent, Multiple mapping conditioning of turbulent jet diffusion flames, Proc. Combust. Inst. 32 (2) (2009) 1679 – 1685.

[45] C. Straub, A. Kronenburg, O. T. Stein, G. Kuenne, J. Janicka, R. S. Barlow, D. Geyer, Multiple mapping conditioning coupled with an artificially thickened flame model for turbulent premixed combustion, Combust. Flame 196 (2018) 325 – 336.

[46] S. K. Ghai, S. De, Numerical investigation of flow and scalar fields of piloted, partially-premixed dimethyl ether/air jet flames using stochastic multiple mapping conditioning approach, Combust. Flame 208 (2019) 480 – 491.

[47] H. Steiner, W. K. Bushe, Large eddy simulation of a turbulent reacting jet with conditional source-term estimation, Phys. Fluids 13 (3) (2001) 754–769.

[48] D. Dovizio, M. Salehi, C. Devaud, RANS simulation of a turbulent premixed bluff body flame using conditional source-term estimation, Combust. Theor. Model. 17 (2013) 935–959.

[49] J. Labahn, C. Devaud, Investigation of conditional source-term estimation applied to a non-premixed turbulent flame, Combust. Theory Model. 17 (5) (2013) 960–982.

[50] R. W. Grout, W. K. Bushe, C. Blair, Predicting the ignition delay of turbulent methane jets using conditional source-term estimation, Combust. Theory Model. 11 (2007) 1009–1028.

[51] M. Wang, J. Huang, W. Bushe, Simulation of a turbulent non-premixed flame using conditional source-term estimation with trajectory generated low-dimensional manifold, Proc. Combust. Inst. 31 (2) (2007) 1701 – 1709.

[52] C. Burgess, C. Lawn, The premixture model of turbulent burning to describe lifted jet flames, Combust. Flame 119 (1) (1999) 95 – 108.

[53] A. R. Hutchins, J. D. Kribs, K. M. Lyons, Effects of diluents on lifted turbulent methane and ethylene jet flames, J. Energy Resources Technol. 137 (3) (2015) 032204.

[54] K. Wohl, N. Kapp, G. Gazley, The stability of open flames, Third Symp. (Int.) Combust. Flame Explosion (1949) 3–21.

[55] N. Peters, F. A. Williams, Liftoff characteristics of turbulent jet diffusion flames, AIAA 21 (3) (1983) 423–429.

[56] J. E. Broadwell, W. J. Dahm, M. G. Mungal, Blowout of turbulent diffusion flames, Symp. (Int.) Combust. 20 (1) (1985) 303 – 310.

[57] C. Lawn, Lifted flames on fuel jets in co-flowing air, Prog. Energy Combust. Sci. 35 (1) (2009) 1 – 30.

[58] R. Cabra, T. Myhrvold, J. Chen, R. Dibble, A. Karpetis, R. Barlow, Simultaneous laser Raman-Rayleigh-LIF measurements and numerical modeling results of a lifted turbulent H_2/N_2 jet flame in a vitiated coflow, Proc. Combust. Inst. 29 (2) (2002) 1881–1888.

[59] R. Cabra, J.-Y. Chen, R. Dibble, A. Karpetis, R. Barlow, Lifted methane–air jet flames in a vitiated coflow, Combust. Flame 143 (4) (2005) 491 – 506.

[60] C. S. Yoo, E. S. Richardson, R. Sankaran, J. H. Chen, A DNS study on the stabilization mechanism of a turbulent lifted ethylene jet flame in highly-heated coflow, Proc. Combust. Inst. 33 (1) (2011) 1619–1627.

[61] L. Vanquickenborne, A. van Tiggelen, The stabilization mechanism of lifted diffusion flames, Combust. Flame 10 (1) (1966) 59 – 69.

[62] H. Eickhoff, B. Lenze, W. Leuckel, Experimental investigation on the stabilization mechanism of jet diffusion flames, Symp. (Int.) Combust. 20 (1) (1985) 311 – 318.

[63] W. M. Pitts, Assessment of theories for the behavior and blowout of lifted turbulent jet diffusion flames, Symp. (Int.) Combust. 22 (1) (1989) 809 – 816.

[64] K. Watson, K. Lyons, J. Donbar, C. Carter, On scalar dissipation and partially premixed flame propagation, Combust. Sci. Technol. 175 (4) (2003) 649–664.

[65] S. Stårner, R. Bilger, J. Frank, D. Marran, M. Long, Mixture fraction imaging in a lifted methane jet flame, Combust. Flame 107 (3) (1996) 307 – 313.

[66] L. Su, O. Sun, M. Mungal, Experimental investigation of stabilization mechanisms in turbulent, lifted jet diffusion flames, Combust. Flame 144 (3) (2006) 494 – 512.

[67] D. Bradley, P. Gaskell, A. Lau, A mixedness-reactedness flamelet model for turbulent diffusion flames, Symp. (Int.) Combust. 23 (1) (1991) 685 – 692.

[68] D. Bradley, P. Gaskell, X. Gu, The mathematical modeling of liftoff and blowoff of turbulent non-premixed methane jet flames at high strain rates, Symp. (Int.) Combust. 27 (1) (1998) 1199 – 1206.

[69] C. Müller, H. Breitbach, N. Peters, Partially premixed turbulent flame propagation in jet flames, Symp. (Int.) Combust. 25 (1) (1994) 1099 – 1106.

[70] M. Chen, M. Herrmann, N. Peters, Flamelet modeling of lifted turbulent methane/air and propane/air jet diffusion flames, Proc. Combust. Inst. 28 (1) (2000) 167 – 174.

[71] A. Kronenburg, Double conditioning of reactive scalar transport equations in turbulent nonpremixed flames, Phys. Fluids 16 (7) (2004) 2640–2648.

[72] C. M. Cha, G. Kosály, H. Pitsch, Modeling extinction and reignition in turbulent nonpremixed combustion using a doubly-conditional moment closure approach, Phys. Fluids 13 (12) (2001) 3824–3834.

[73] A. Kronenburg, M. Kostka, Modeling extinction and reignition in turbulent flames, Combust. Flame 143 (4) (2005) 342 – 356.

[74] A. Kronenburg, A. Papoutsakis, Conditional moment closure modeling of extinction and re-ignition in turbulent non-premixed flames, Proc. Combust. Inst. 30 (1) (2005) 759 – 766.

[75] F. Salehi, M. Talei, E. R. Hawkes, A. Bhagatwala, J. H. Chen, C. S. Yoo, S. Kook, Doubly conditional moment closure modelling for HCCI with temperature inhomogeneities, Proc. Combust. Inst. 36 (3) (2017) 3677 – 3685.

[76] R. Barlow, J. Frank, Effects of turbulence on species mass fractions in methane/air jet flames, Symp. (Int.) Combust. 27 (1998) 1087 – 1095.

[77] C. Schneider, A. Dreizler, J. Janicka, E. Hassel, Flow field measurements of stable and locally extinguishing hydrocarbon-fuelled jet flames, Combust. Flame 135 (1) (2003) 185 – 190.

[78] H. Pitsch, H. Steiner, Large-eddy simulation of a turbulent piloted methane/air diffusion flame (Sandia flame D), Phys. Fluids 12 (10) (2000) 2541–2554.

[79] P. Coelho, N. Peters, Unsteady modelling of a piloted methane/air jet flame based on the eulerian particle flamelet model, Combust. Flame 124 (3) (2001) 444 – 465.

[80] J. Xu, S. B. Pope, PDF calculations of turbulent nonpremixed flames with local extinction, Combust. Flame 123 (3) (2000) 281 – 307.

[81] M. Hegetschweiler, B. T. Zoller, P. Jenny, Reactive parametrized scalar profiles (R-PSP) mixing model for partially premixed combustion, Combust. Flame 159 (2) (2012) 734 – 747.

[82] H. Turkeri, S. B. Pope, M. Muradoglu, A LES/PDF simulator on block-structured meshes, Combust. Theory Model. 23 (1) (2019) 1–41.

[83] M. Sheikhi, T. Drozda, P. Givi, F. Jaberi, S. Pope, Large eddy simulation of a turbulent nonpremixed piloted methane jet flame (Sandia Flame D), Proc. Combust. Inst. 30 (1) (2005) 549 – 556.

[84] M. B. Nik, S. L. Yilmaz, M. R. H. Sheikhi, P. Givi, Grid resolution effects on VSFMDF/LES, Flow Turbul. Combust. 85 (3) (2010) 677–688.

[85] Y. Ge, M. Cleary, A. Klimenko, Sparse-lagrangian FDF simulations of Sandia Flame E with density coupling, Proc. Combust. Inst. 33 (1) (2011) 1401 – 1409.

[86] K. Vogiatzaki, S. Navarro-Martinez, S. De, A. Kronenburg, Mixing modelling framework based on multiple mapping conditioning for the prediction of turbulent flame extinction, Flow Turbul. Combust. 95 (2) (2015) 501–517.

[87] A. P. Wandel, R. P. Lindstedt, Hybrid multiple mapping conditioning modeling of local extinction, Proc. Combust. Inst. 34 (1) (2013) 1365 – 1372.

[88] K. Vogiatzaki, A. Kronenburg, S. Navarro-Martinez, W. Jones, Stochastic multiple mapping conditioning for a piloted, turbulent jet diffusion flame, Proc. Combust. Inst. 33 (1) (2011) 1523 – 1531.

[89] C. Straub, S. De, A. Kronenburg, K. Vogiatzaki, The effect of timescale variation in multiple mapping conditioning mixing of PDF calculations for Sandia flame series D–F, Combust. Theory Model. 20 (5) (2016) 894–912.

[90] A. Varna, M. J. Cleary, E. R. Hawkes, A multiple mapping conditioning mixing model with a mixture-fraction like reference variable. part 2: RANS implementation and validation against a turbulent jet flame, Combust. Flame 181 (2017) 354 – 364.

[91] V. Hiremath, S. R. Lantz, H. Wang, S. B. Pope, Computationally-efficient and scalable parallel implementation of chemistry in simulations of turbulent combustion, Combust. Flame 159 (10) (2012) 3096 – 3109.

[92] V. Hiremath, S. R. Lantz, H. Wang, S. B. Pope, Large-scale parallel simulations of turbulent combustion using combined dimension reduction and tabulation of chemistry, Proc. Combust. Inst. 34 (1) (2013) 205 – 215.

[93] W. Jones, V. Prasad, Large eddy simulation of the sandia flame series (D–F) using the eulerian stochastic field method, Combust. Flame 157 (9) (2010) 1621 – 1636.

[94] K. A. Kemenov, S. B. Pope, Molecular diffusion effects in LES of a piloted methane–air flame, Combust. Flame 158 (2) (2011) 240 – 254.

[95] K. Han, K. Y. Huh, First and second order lagrangian conditional moment closure method in turbulent nonpremixed flames, Proc. Combust. Inst. 35 (2) (2015) 1175 – 1182.

[96] M. Ihme, H. Pitsch, Prediction of extinction and reignition in nonpremixed turbulent flames using a flamelet/progress variable model: 2. application in LES of sandia flames D and E, Combust. Flame 155 (1) (2008) 90 – 107.

[97] W. Zhao, Large-Eddy Simulation of piloted diffusion flames using multi-environment probability density function models, Proc. Combust. Inst. 36 (2) (2017) 1705 – 1712.

[98] A. Bertels, B. Kober, A. Rittler, A. Kempf, Large-eddy simulation of Sandia Flame D with efficient explicit filtering, Flow Turbul. Combust. 102 (4) (2019) 887–907.

[99] A. C. Nunno, M. E. Mueller, Manifold assumptions in modeling radiation heat losses in turbulent nonpremixed combustion, Proc. Combust. Inst. 37 (2) (2019) 2223 – 2230.

[100] T. Pant, C. Han, H. Wang, Examination of errors of table integration in flamelet/progress variable modeling of a turbulent non-premixed jet flame, App. Math. Model. 72 (2019) 369 – 384.

[101] S. Zahirović, R. Scharler, P. Kilpinen, I. Obernberger, Validation of flow simulation and gas combustion sub-models for the CFD-based prediction of NOx formation in biomass grate furnaces, Combust. Theory Model. 15 (1) (2010) 61–87.

[102] M. Roomina, R. Bilger, Conditional moment closure (CMC) predictions of a turbulent methane-air jet flame, Combust. Flame 125 (3) (2001) 1176 – 1195.

[103] S. H. Kim, K. Y. Huh, Second-order conditional moment closure modeling of turbulent piloted jet diffusion flames, Combust. Flame 138 (4) (2004) 336 – 352.

[104] S. Navarro-Martinez, A. Kronenburg, F. D. Mare, Conditional moment closure for large eddy simulations, Flow Turbul. Combust. 75 (2005) 245–274.

[105] A. Garmory, E. Mastorakos, Capturing localised extinction in Sandia flame F with LES–CMC, Proc. Combust. Inst. 33 (1) (2011) 1673 – 1680.

[106] J. W. Labahn, I. Stanković, C. B. Devaud, B. Merci, Comparative study between conditional moment closure (CMC) and conditional source-term estimation (CSE) applied to piloted jet flames, Combust. Flame 181 (2017) 172 – 187.

[107] W. Bushe, Spatial gradients of conditional averages in turbulent flames, Combust. Flame 192 (2018) 314 – 339.

[108] G. R. Hendra, W. Bushe, The uniform conditional state model for turbulent reacting flows, Combust. Flame 205 (2019) 484 – 505.

[109] S. S. Girimaji, Assumed β-PDF model for turbulent mixing: Validation and extension to multiple scalar mixing, Combust. Sci. Technol. 78 (4-6) (1991) 177–196.

[110] B. Fiorina, R. Vicquelin, P. Auzillon, N. Darabiha, O. Gicquel, D. Veynante, A filtered tabulated chemistry model for LES of premixed combustion, Combust. Flame 157 (3) (2010) 465 – 475.

[111] B. Jin, R. Grout, W. K. Bushe, Conditional source-term estimation as a method for chemical closure in premixed turbulent reacting flow, Flow Turbul. Combust. 81 (4) (2008) 563–582.

[112] K. Bray, M. Champion, P. Libby, N. Swaminathan, Finite rate chemistry and presumed PDF models for premixed turbulent combustion, Combust. Flame 146 (4) (2006) 665–673.

[113] B. Vanderstraeten, D. Tuerlinckx, J. Berghmans, S. Vliegen, E. V. Oost, B. Smit, Experimental study of the pressure and temperature dependence on the upper flammability limit of methane/air mixtures, J. Hazard. Materials 56 (3) (1997) 237 – 246.

[114] N. Kim, Y. Kim, Multi-environment probability density function approach for turbulent partially-premixed methane/air flame with inhomogeneous inlets, Combust. Flame 182 (2017) 190 – 205.

[115] S. B. Pope, Small scales, many species and the manifold challenges of turbulent combustion, Proc. Combust. Inst. 34 (1) (2013) 1 – 31.

[116] U. Maas, S. Pope, Simplifying chemical kinetics: Intrinsic low-dimensional manifolds in composition space, Combust. Flame 88 (3) (1992) 239 – 264.

[117] J. Huang, W. K. Bushe, Simulation of transient turbulent methane jet ignition and combustion under engine-relevant conditions using conditional source-term estimation with detailed chemistry, Combust. Theory Model. 11 (6) (2007) 977–1008.

[118] J. Hadamard, Sur les problemes aux derives partielles et leur signification physique, Princeton Univ. Bulletin 13 (1902) 49–52.

[119] P. C. Hansen, The truncated SVD as a method for regularization, BIT Num. Math. 27 (4) (1987) 534–553.

[120] A. Tikhonov, V. Arsenin, Solution of ill-posed problems, Halsted Press, 1977.

[121] J. W. Labahn, C. B. Devaud, T. A. Sipkens, K. J. Daun, Inverse analysis and regularisation in conditional source-term estimation modelling, Combust. Theory Model. 18 (3) (2014) 474–499.

[122] M. Salehi, W. Bushe, K. Daun, Application of the conditional source-term estimation model for turbulence-chemistry interactions in a premixed flame, Combust. Theory Model. 16 (2012) 301–320.

[123] P. C. Hansen, Numerical tools for analysis and solution of Fredholm integral equations of the first kind, Inverse Problems 8 (6) (1992) 849–872.

[124] W. K. Bushe, H. Steiner, Laminar flamelet decomposition for conditional source-term estimation, Phys. Fluids 15 (6) (2003) 1564–1575.

[125] J. Labahn, C. Devaud, Large eddy simulations (LES) including conditional source-term estimation (CSE) applied to two Delft-Jet-in-Hot-Coflow (DJHC) flames, Combust. Flame 164 (2016) 68 – 84.

[126] H. P. Tsui, W. K. Bushe, Conditional source-term estimation using dynamic ensemble selection and parallel iterative solution, Combust. Theory Model. 20 (5) (2016) 812–833.

[127] C. C. Paige, M. A. Saunders, Lsqr: an algorithm for sparse linear equations and sparse least squares, ACM Trans. Math. Softw. 8 (1982) 43–71.

[128] H. M. Iyer, K. Hirahara, Seismic Tomography: Theory and Practice, Chapman and Hall, 1993.

[129] Y. Saad, H. A. van der Vorst, Iterative solution of linear systems in the 20th century, J. Comp. App. Math. 123 (1) (2000) 1 – 33.

[130] G. Golub, W. Kahan, Calculating the singular values and pseudo-inverse of a matrix, J. Society Indust. App. Math. 2 (2) (1965) 205–224.

[131] E.-J. Lee, H. Huang, J. M. Dennis, P. Chen, L. Wang, An optimized parallel LSQR algorithm for seismic tomography, Comp. Geosci. 61 (2013) 184 – 197.

[132] C. Bowman, R. Hanson, D. Davidson, W. Gardiner, J. V. Lissianski, G. Smith, D. Golden, M. Frenklach, M. Goldenberg, GRI-Mech 2.11 (1995).

[133] P. Smith, D. Golden, M. Frenklach, N. Moriarty, B. Eiteneer, M. Goldenberg, C. Bowman, R. Hanson, S. Song, W. Gardiner, J. V. Lissianski, Z. Qin, GRI-Mech 3.0 (1995).

[134] J. Warnatz, U. Maas, R. Dibble, Combustion: Physical and Chemical Fundamentals, Modeling and Simulation, Experiments, Pollutant Formation, Springer, 2006.

[135] S. Pope, U. Maas, Simplifying chemical kinetics: trajectory-generated low-dimensional manifolds, Tech. rep., Cornell University Report FDA (1993).

[136] J. Ignizio, T. Cavalier, Linear programming, Prentice Hall Int. Series Indust. Sys. Eng.

[137] R. Renka, Tripack: a constrained two-dimensional delaunay triangulation, ACM Trans. Math. softw. 22 (1996) 1 – 8.

[138] R. R. Tirunagari, S. B. Pope, LES/PDF for premixed combustion in the DNS limit, Combust. Theory Model. 20 (5) (2016) 834–865.

[139] J. Floyd, A. M. Kempf, A. Kronenburg, R. H. Ram, A simple model for the filtered density function for passive scalar combustion LES, Combust. Theory Model. 13 (4) (2009) 559–588.

[140] M. M. Salehi, W. K. Bushe, N. Shahbazian, C. P. Groth, Modified laminar flamelet presumed probability density function for LES of premixed turbulent combustion, Proc. Combust. Inst. 34 (1) (2013) 1203 – 1211.

[141] T. Tahtouh, F. Halter, C. Mounaïm-Rousselle, Measurement of laminar burning speeds and markstein lengths using a novel methodology, Combust. Flame 156 (9) (2009) 1735 – 1743.

[142] A. De, E. Oldenhof, P. Sathiah, D. Roekaerts, Numerical simulation of delft-jet-in-hot-coflow (DJHC) flames using the eddy dissipation concept model for turbulence–chemistry interaction, Flow Turbul. Combust. 87 (4) (2011) 537–567.

[143] S. Ruan, N. Swaminathan, K. Bray, Y. Mizobuchi, T. Takeno, Scalar and its dissipation in the near field of turbulent lifted jet flame, Combust. Flame 159 (2) (2012) 591–608.

[144] P. Domingo, L. Vervisch, K. Bray, Partially premixed flamelets in LES of non-premixed turbulent combustion, Combust. Theory Model. 6 (4) (2002) 529–551.

[145] T. Mantel, R. Borghi, A new model of premixed wrinkled flame propagation based on a scalar dissipation equation, Combust. Flame 96 (4) (1994) 443 – 457.

[146] V. Robin, A. Mura, M. Champion, O. Degardin, B. Renou, M. Boukhalfa, Experimental and numerical analysis of stratified turbulent V-shaped flames, Combust. Flame 153 (1) (2008) 288 – 315.

[147] N. Chakraborty, N. Swaminathan, Influence of the Damköhler number on turbulence-scalar interaction in premixed flames. i. physical insight, Phys. Fluids 19 (4) (2007) 045103.

[148] Y. Nada, M. Tanahashi, T. Miyauchi, Effect of turbulence characteristics on local flame structure of H_2-air premixed flames, in: TSFP Digital Library Online, Begel House Inc., 2003.

[149] C. Rutland, R. Cant, Turbulent transport in premixed flames, Proc. the 1994 Summer Program Stanford Univ.

[150] R. Schefer, M. Namazian, J. Kelly, Stabilization of lifted turbulent-jet flames, Combust. Flame 99 (1) (1994) 75–86.

[151] C. Devaud, K. Bray, Assessment of the applicability of conditional moment closure to a lifted turbulent flame: first order model, Combust. Flame 132 (1) (2003) 102 – 114.

[152] W. Wang, T. Echekki, Investigation of lifted jet flames stabilization mechanism using RANS simulations, Fire Saf. J. 46 (5) (2011) 254–261.

[153] G. V. Nivarti, M. M. Salehi, W. K. Bushe, A mesh partitioning algorithm for preserving spatial locality in arbitrary geometries, J. Comp. Phys. 281 (2015) 352 – 364.

[154] Z. Chen, S. Ruan, N. Swaminathan, Large eddy simulation of flame edge evolution in a spark-ignited methane–air jet, Proc. Combust. Inst. 36 (2) (2017) 1645 – 1652.

[155] S. Ruan, N. Swaminathan, O. Darbyshire, Modelling of turbulent lifted jet flames using flamelets: a priori assessment and a posteriori validation, Combust. Theor. Model. 18 (2014) 295–329.

[156] T. Dunstan, Y. Minamoto, N. Chakraborty, N. Swaminathan, Scalar dissipation rate modelling for large eddy simulation of turbulent premixed flames, Proc. Combust. Inst. 34 (1) (2013) 1193 – 1201.

[157] D. Veynante, R. Knikker, Comparison between LES results and experimental data in reacting flows, J. Turbul. 7 (2006) N35.

[158] I. Kim, E. Mastorakos, Simulations of turbulent lifted jet flames with two-dimensional conditional moment closure, Proc. Combust. Inst. 30 (1) (2005) 911 – 918.

[159] S. Ferraris, J. Wen, Large eddy simulation of a lifted turbulent jet flame, Combust. Flame 150 (4) (2007) 320 – 339.

[160] A. Linan, A. Crespo, An asymptotic analysis of unsteady diffusion flames for large activation energies, Combust. Sci. Technol. 14 (1-3) (1976) 95–117.

[161] J. Dold, Flame propagation in a nonuniform mixture: Analysis of a slowly varying triple flame, Combust. Flame 76 (1) (1989) 71 – 88.

[162] S. Karami, E. R. Hawkes, M. Talei, J. H. Chen, Edge flame structure in a turbulent lifted flame: A direct numerical simulation study, Combust. Flame 169 (2016) 110 – 128.

[163] M. S. Mansour, The flow field structure at the base of lifted turbulent partially premixed jet flames, Exp. Therm. Fluid Sci. 28 (7) (2004) 771 – 779.

[164] K. Watson, K. Lyons, C. Carter, J. Donbar, Simultaneous two-shot CH planar laser-induced fluorescence and particle image velocimetry measurements in lifted CH_4/air diffusion flames, Proc. Combust. Inst. 29 (2) (2002) 1905 – 1912.

[165] A. Joedicke, N. Peters, M. Mansour, The stabilization mechanism and structure of turbulent hydrocarbon lifted flames, Proc. Combust. Inst. 30 (1) (2005) 901 – 909.

[166] A. Mura, K. Tsuboi, T. Hasegawa, Modelling of the correlation between velocity and reactive scalar gradients in turbulent premixed flames based on DNS data, Combust. Theory Model. 12 (4) (2008) 671–698.

[167] I. Langella, N. Swaminathan, Unstrained and strained flamelets for LES of premixed combustion, Combust. Theory Model. 20 (3) (2016) 410–440.

[168] A. Karpetis, R. Barlow, Measurements of scalar dissipation in a turbulent piloted methane/air jet flame, Proc. Combust. Inst. 29 (2002) 1929 – 1936.

[169] D. Cecere, E. Giacomazzi, F. R. Picchia, N. Arcidiacono, F. Donato, R. Verzicco, A non-adiabatic flamelet progress–variable approach for LES of turbulent premixed flames, Flow Turbul. Combust. 86 (3) (2011) 667–688.

[170] A. Ketelheun, G. Kuenne, J. Janicka, Heat transfer modeling in the context of large eddy simulation of premixed combustion with tabulated chemistry, Flow Turbul. Combust. 91 (4) (2013) 867–893.

[171] Z. X. Chen, I. Langella, N. Swaminathan, M. Stöhr, W. Meier, H. Kolla, Large eddy simulation of a dual swirl gas turbine combustor: Flame/flow structures and stabilisation under thermoacoustically stable and unstable conditions, Combust. Flame 203 (2019) 279 – 300.

[172] F. Proch, P. Domingo, L. Vervisch, A. M. Kempf, Flame resolved simulation of a turbulent premixed bluff-body burner experiment. part i: Analysis of the reaction zone dynamics with tabulated chemistry, Combust. Flame 180 (2017) 321 – 339.

[173] S. Popp, F. Hunger, S. Hartl, D. Messig, B. Coriton, J. H. Frank, F. Fuest, C. Hasse, Les flamelet-progress variable modeling and measurements of a turbulent partially-premixed dimethyl ether jet flame, Combust. Flame 162 (8) (2015) 3016 – 3029.

[174] M. Mortada, C. Devaud, Large eddy simulation of lifted turbulent flame in cold air using doubly conditional source-term estimation, Combust. Flame 208 (2019) 420 – 435.

[175] E. Fernández-Tarrazo, A. L. Sánchez, A. Liñán, F. A. Williams, A simple one-step chemistry model for partially premixed hydrocarbon combustion, Combust. Flame 147 (1) (2006) 32 – 38.

[176] I. Yamaoka, H. Tsuji, Determination of burning velocity using counterflow flames, Symp. (In.) Combust. 20 (1) (1985) 1883 – 1892.

[177] F. Shum-Kivan, J. M. Santiago, A. Verdier, E. Riber, B. Renou, G. Cabot, B. Cuenot, Experimental and numerical analysis of a turbulent spray flame structure, Proc. Combust. Inst. 36 (2) (2017) 2567 – 2575.